CREEP CORRELATION OF MICRO-ALLOYED HP40Nb REFORMER STEEL

A Thesis Submitted in
Partial Fulfillment of the Requirements
for the Degree of

DOCTOR OF PHILOSOPHY

by

AMITAVA GHATAK

(Roll No.: 09610307)

DEPARTMENT OF MECHANICAL ENGINEERING
INDIAN INSTITUTE OF TECHNOLOGY GUWAHATI
GUWAHATI-781039, INDIA

FEBRUARY 2015

DEPARTMENT OF MECHANICAL ENGINEERING
INDIAN INSTITUTE OF TECHNOLOGY GUWAHATI,
GUWAHATI – 781 039, ASSAM,
INDIA

CERTIFICATE

This is to certify that the thesis entitled "**CREEP CORRELATION OF MICRO-ALLOYED HP40Nb REFORMER STEEL"** submitted by **Mr. Amitava Ghatak**, to the Indian Institute of Technology Guwahati, Guwahati for the award of the degree of **Doctor of Philosophy**, is a bona fide record of the research work done by him under my supervision in the Department of Mechanical Engineering, Indian Institute of Technology Guwahati, Guwahati. The contents of this thesis, in full or in parts, have not been submitted to any other institute or university for the award of any degree or diploma.

Dr. P.S. Robi
Professor
Department of Mechanical Engineering
Indian Institute of Technology Guwahati
Guwahati-781039, Assam, India

10th February, 2015

Phone: (0361) 2582668 (Off.), Fax: (0361) 2582699

TH-1394_09610307

Dedicated to

I would like to dedicate this thesis to my loving

Father, Sri. Bhaskardeb Ghatak and

Mother, Smt. Gitasree Ghatak

Whose unending and unconditional love, affection, encouragement, wisdom, sacrifices and prays of day and night makes me able to get such success and honor.

To my lovely friend and wife, Smt. Manjula Ghatak,

Whose consecutive support, patience and sacrificial care for me and our children made it possible for me to complete this work and

To our son Adrish and newly born baby who are indeed treasure from God.

Along with all hard working and respected Teachers.

TH-1394_09610307

ACKNOWLEDGEMENT

I am immensely indebted to my supervisor Prof. P.S. Robi, for his valuable guidance, support, comments and inspiration during the tenure of my PhD work at Indian Institute of Technology Guwahati, Guwahati. It was a great pleasure working with Prof. Robi and I hope, I can continue working with him in future. I am also sincerely grateful to members of my doctoral committee, Prof. U.S. Dixit, Prof. A. Srinivasan, and Dr. R. Ganesh Narayanan for their advice, valuable suggestions and encouragement during the period of my research work.

My sincere gratefulness to past and present departmental heads is due to Prof. D. Chakraborty, Prof. P. Mahanta and Prof. A.K. Dass for their kind permission for enrollment, registration and several important supports at IIT Guwahati. I would like to acknowledge my sense of gratitude to all the staffs of the Mechanical Workshop for their help in fabrication of experimental set-up for this work. I also wish to express my gratitude to the Central Instruments Facility, IIT Guwahati, India for providing technical support with SEM and TEM facility. I would like to thank Numaligarh Refinery Limited, Assam, India for providing reformer tube and much useful information regarding the tube.

My warm appreciation is to my wife Smt. Manjula Ghatak for her understanding, patience throughout my PhD candidature and finally taking care of our son. To our beautiful son Master Adrish Ghatak and newly born baby who are indeed treasure from God during my PhD tenure. I am always grateful to my sister, Late Debjani Chakraborty, for her inspiration. I consider myself most unfortunate as I could not present this work to my sister who left for heaven abode.

Finally and most importantly, at a personal level, I also wish to record my indebtedness to my parents, Sri. Bhaskardeb Ghatak and Smt. Gitasree Ghatak, for their continuous encouragement, invaluable love, warm wishes and day by day guidance.

Above all, I am thankful to the Almighty.

9th February, 2015 *Amitava Ghatak*

TH-1394_09610307

ABSTRACT

Reformer tube material generally used in petrochemical industries for prolonged service conditions of 800 ˚C - 1000 ˚C and gas pressures 0.5 MPa - 4.2 MPa are centrifugally cast austenitic stainless steel. Many times premature failure of these materials occurs by creep deformation resulting in forced shut down of the plant. Several reports are available in literature regarding the creep failure analysis of metallic materials, each report having its own advantages and limitations. An insight regarding the creep behavior and analysis of the creep life prediction techniques is required for the safe design of the component. Hence, this work was carried out to investigate the microstructure, high temperature tensile behaviour and constant stress creep behavior of micro-alloyed HP40Nb centrifugally cast austenitic stainless steels.

High temperature tensile tests reveal that Young's modulus, yield strength, and ultimate tensile strength of the material decrease with increase in test temperature. The ductility continuously increases with increase in temperature up to 1000 ˚C and decreases drastically with further increase in test temperature. The strain hardening exponent increases up to 600 ˚C, beyond which it starts decreasing. Microstructural investigation of the tube revealed carbides rich in Cr, Nb and Ti at grain boundary regions which are typical features of the cast material. Exposure of the reformer tube material above 1000 ˚C revealed dissolution of Cr_7C_3 in the matrix with concomitant increase in $Cr_{23}C_6$ resulting in loss of ductility.

Creep behaviour of the reformer tube material is investigated by carrying out accelerated creep tests at 650 ˚C - 1050 ˚C and 47 MPa - 120 MPa stress levels. The strains in the three creep regions were analyzed in terms of temperature, stress and minimum creep rate. Analysis of minimum creep rate, strain to rupture and rupture time by Monkman-Grant relation and modified Monkman-Grant relation indicate both methods are valid for the investigated steel. The relationship between time to reach Monkman-Grant ductility and rupture life is established for the steel in terms of damage tolerance factor.

The apparent activation energy for creep and stress exponent show a non-linear second order polynomial relationship with stress and temperature, respectively. The expression for the minimum creep rate obtained by constitutive modeling follows the

TH-1394_09610307

power law relation in the form $\dot{\varepsilon}_s = 9.42 \times 10^{-6}\sigma^{8.3}\exp\left(-\frac{312670}{RT}\right)$. Investigation of the creep rupture sample surfaces reveals nucleation and growth of voids at Cr rich phases as the main mechanism of damage at elevated temperatures.

Researchers were not able to predict the creep curves of materials from the data generated from experiments. This is mainly due to the fact that the creep curve consists of three regions characterized by different deformation behavior. An attempt was carried out to predict the creep curves for various combinations of stresses and temperatures from limited experiential data. Using the data obtained from the creep tests, the creep curves could be successfully generated by Artificial Neural Network (ANN) modeling by a three layer feed-forward back propagation network using Lavenberg-Marquardt optimization algorithm. During the validation stage, 98 % of the creep strain data points could be predicted within a deviation error of ± 10 % where the maximum deviation error was 18% compared to the experimental values. An additional experiment carried out to check the authenticity of the creep curve simulation confirms very good prediction capability by ANN modeling. The correlation coefficient R_{cc} and average absolute relative error (AARE) between experimental and predicted strain values are found to be 0.994 and 23 %, respectively. The minimum creep rate of the material obtained by ANN modeling is very close to the experimental data compared to that obtained by the constitutive equation.

Prediction of the creep life of HP40Nb reformer steel tube under various combinations of temperatures and stresses was carried out by three techniques viz., Manson-Haferd technique, Orr-Sherby-Dorn technique and Larson-Miller technique and the results compared. The results obtained by Mansion-Hafred technique and Orr-Sherby-Dorn technique are found to be over-estimated values. While predicting the creep life by Larson-Miller technique, it was found that the Larson-Miller constant $C_{L\text{-}M}$ used in the $P_{L\text{-}M}$ equation is not a constant. The $C_{L\text{-}M}$ is stress dependent and hence the $P_{L\text{-}M}$ equation needs to be modified. The life prediction by L-M technique was carried out by considering $C_{L\text{-}M}$ as a constant as well as a stress dependent function. Comparison of the results reveals that the large scatter in the master curve is reduced by considering $C_{L\text{-}M}$ as a function of stress. The creep life prediction using $C_{L\text{-}M}$ as a function of stress shows more conservative result compared to the case when $C_{L\text{-}M}$ is considered as a constant.

TH-1394_09610307

CONTENTS

TH-1394_09610307

TH-1394_09610307

TH-1394_09610307

LIST OF FIGURES

TH-1394_09610307

TH-1394_09610307

TH-1394_09610307

TH-1394_09610307

TH-1394_09610307

LIST OF TABLES

TH-1394_09610307

NOMENCLATURE

RMS_{err}^{f}	Root mean square
$\bar{l}$	Mean intercept length
A, A_0, A_1, A_2, A_3, A_4, A_5, A_6, A_7, A_8, A_9, A_{10}, A_{11}, A_{12}, A_{13}	Constant
A_i	Instantaneous area of the gauge section
A_o	Initial gauge area
C, C'	Constant
$C_{L\text{-}M}$	Larson-Miller constant
$C_{L\text{-}M}(\sigma)$	$C_{L\text{-}M}$ as a function of stress
C_{MG}	Monkman-Grant constant
C_{MMG}	Modified Monkman-Grant constant
d	Average grain size
E	Young's modulus
E_i	Experimental value
F_i	Instantaneous load
G	Shear modulus or modulus of rigidity
I	Net input to the neuron
K	Strength coefficient
K_1, K_1', K_T'	Constants
L_{gauge}	Initial gauge length
l_p	Number of intercepts (intersections with grain boundaries) per unit length
m, m'	Constant
n	Strain-hardening exponent
N	Number of data set
n_c	Stress exponent
P_i	Predicted value
$P_{L\text{-}M}$	Larson-Miller parameter
$P_{M\text{-}H}$	Manson-Haferd parameter
$P_{O\text{-}S\text{-}D}$	Orr-Sherby-Dorn parameter
Q_{app}	Apparent activation energy for creep
Q_c	Activation energy for self-diffusion

TH-1394_09610307

R	Universal gas constant (= 8.314 J K^{-1} mol^{-1})
R^2	Coefficient of determination
R_{cc}	Correlation coefficient
t	Time
T	Test temperature
t_0	Initial thickness of gauge section
t_{MGD}	Time to reach MGD
t_{os}	Onset of secondary creep
t_{ot}	Time at the onset of tertiary creep
t_r	Time to rupture or rupture life
W_0	Initial width of gauge section

Greek

$\dot{\varepsilon}_s$	Minimum creep rate
α, β	Constant
γ	Austenite
Δ	Change in gauge length
ε	Elastic strain
ε_2	Secondary creep strain
ε_c	Time-dependent strain (creep strain)
ε_f	Fracture strain
ε_o	Initial strain or instantaneous strain on loading
$\varepsilon_p, \varepsilon_1$	Primary creep strain
$\varepsilon_t, \varepsilon_3$	Tertiary creep strain
ε_{total}	Total strain
κ	Constant
λ	Creep damage tolerance factor
σ	Applied stress
σ_{th}	Creep threshold stress

TH-1394_09610307

ABBREVIATIONS

AARE	Average absolute relative error
ANN	Artificial neural network
ASTM	American society for testing and materials
BPNN	Back-propagation neural network
BSD	Backscattered electron detector
CDM	Continuum creep damage mechanics
DAQ	Data acquisition
EDX	Energy dispersive X-ray
FCC	Face centered cubic
FESEM	Field emission electron microscopy
HD	High definition
HR-TEM	High resolution transmission electron microscopy
MGD	Monkman-Grant ductility
MGR	Monkman-Grant relationship
MLP	Multiple layer precipitation
MMGR	Modified Monkman-Grant relationship
NID	Neural interpretation diagram
OM	Optical microscopy
PID	Proportional-integral-derivative
RMS	Average root mean square
SAD	Selective area diffraction
SE	Secondary electron
SEM	Scanning electron microscopy
TEM	Transmission electron microscopy
UTM	Universal testing machine
UTS	Ultimate tensile strength
WEDM	Wire cut electrical discharge machining
XRD	X-ray diffraction
YS	Yield strength

TH-1394_09610307

CHAPTER 1

INTRODUCTION

1.1 General

Last few decades, it has been witnessed that increase in energy demand with simultaneous ever increasing cost of oil and its bi-products across the world. In industries such as refineries, petrochemical industries, fertilizer plants, gas-based sponge iron plants, etc., in-house production of gases like ammonia, methane, ethane, synthesis gas, hydrogen, etc. are required for the economic production of various products. Hydrogen is an essential gas for the production of ultra-low sulfur diesel and gasoline. The reaction of hydrocarbons and steam at an elevated temperature in reformer furnace tubes produces hydrogen gas. In the reformer tubes, endothermic catalytic reaction takes place at high temperature and converts the hydrocarbon-steam mixture into hydrogen and carbon dioxide. The reforming process necessitates the tube materials to withstand high temperatures and pressures. The centrifugally cast tubes are extensively used in industries for this purpose.

High temperature austenitic stainless steels which can withstand higher temperature and stress for prolonged time have been used as a material of reformer furnace tubes for the last 6-7 decades. The initial reformer tubes were wrought low carbon (~0.1 wt. %) stainless steels. In 1970s, centrifugally cast high carbon HK-40 alloy (0.4 C-25Cr–20Ni–Fe) was developed. In 1980s and early 1990s, a higher creep resistance HP alloy was developed by addition of Nb [1, 2]. The typical chemical composition (wt. %) of the steel is C: 0.35-0.45, Cr: 23-27, Ni: 33-36, Mn: 1-1.5, Si: 1-2 and Nb: 0.8-1.2 [3-9]. Since mid-1990s, a modified version of these alloys, exhibiting still better creep and corrosion resistance by micro alloying with elements like Ti, Ta, Zr, came in to existence. .

The normal service temperatures of the reformer tubes range from 750-1000 °C with a design life of 10^5 operating hours. Though these tubes are designed to withstand the temperature and gas pressure for prolonged time, incidents of premature failure of these materials are very frequent which leads to heavy economic loss for the industry. The reasons for the failures are due to carbonization, oxidation, overheating, stress corrosion cracking, sulfidation or creep failure. In most of the case, the failure was due

TH-1394_09610307

to creep failure. The tube design for creep at the specific service conditions is to be carried out very carefully.

The design life of 10^5 hours at the service conditions has been arrived from creep data of these materials. It is unrealistic to perform creep tests for the entire projected design life, particularly for 10^5 hours of service. The usual practice is to carry out accelerated creep tests by increasing the temperature and/or stress and extrapolating the data obtained to the service conditions. Several techniques of creep life prediction exists viz., constitutive modeling, Monkman-grant relationship, and parametric techniques, each having its own merit and demerit. In the constitutive modeling technique, the minimum creep rate is evaluated based on constitutive parameters and the time to attain a specified creep strain is taken as the creep life of the material. When tested over a wide range of temperatures, the error in the minimum creep rate determined by this technique is in many cases found to be varying by around two orders of magnitude leading to unrealistic values in the creep life prediction. The rupture life prediction by Monkman-Grant relationships is based on the experimental values of creep rupture time and minimum creep rate. The limitations of these techniques are that the creep life cannot be determined by extrapolation of accelerated creep test data. The present practice of life assessment of reformer tubes by industries are by several parametric techniques proposed by investigators. Among the various parametric techniques proposed by the investigators, the Larson-Miller technique [10], Orr-Sherby-Dorn method [11], Manson-Haferd method [12] have found wide acceptance by industries. In spite of the fact that these techniques were developed during 1960s, less attention has been paid to further refine the methodology of analysis.

Larson-Miller parameter $P_{L\text{-}M}$ is most extensively used by industries to predict the creep life of the reformer tubes. In this technique the creep life of the material is determined from σ versus $P_{L\text{-}M}$ master curve. Following the standard practice, investigators observed a large scatter in master curves. The standard practice is by considering the Larson-Miller constant $C_{L\text{-}M}$ in the expression of $P_{L\text{-}M}$ as a constant by trial and error method. A critical analysis reveals that Larson-Miller constant $C_{L\text{-}M}$ is not a constant but depends on the applied stress. By considering the $C_{L\text{-}M}$ value as a stress dependent parameter, the scatter in the master curve can be reduced to a great extent

TH-1394_09610307

thereby one can predict a creep life which may be more realistic compared to the existing standard practice.

During the past 30 years, there has been a substantial amount of work published on the prediction of creep curves using various techniques such as θ-projection technique [13], omega method [14], modified θ-projection technique [15] and finite element technique [16]. These techniques have some limitations and complex to solve. So far researchers were not successful in predicting the creep curves under various combinations of stress and temperature from limited experiential data. It is expected that the problem may solve faster and with a reasonable accuracy using Artificial Neural Network which is difficult by conventional computer programs or human intelligence.

1.2 Major Objectives

The present work aims at investigating the creep behavior of micro-alloyed HP Grade (25Cr-35Ni-0.4C-1Nb) centrifugally cast austenitic stainless steels by carrying out accelerated creep tests at different temperatures and stresses. The material was exposed at 650 °C for 11 years. The experimental data was used for developing creep deformation models by the constitutive equations as well as by parametric techniques and predicting the life of the tube. An attempt was also carried out to predict the creep curve of the material by Artificial Neural Network modeling.

1.3 Layout of the Thesis

This thesis consists of five chapters which are summarized as follows:

- Chapter-1 introduces the importance of creep deformation in reformer tubes and briefly highlights the importance of the thesis work.
- Chapter-2 presents the summary of literature available regarding reformer tubes, the creep deformation and review of various creep deformation models for determination of the creep life of creep resistant materials. Finally, the technical gaps which are to be addressed in this area are highlighted. The chapter ends by highlighting the main objectives of the present work.
- Chapter-3 describes the methodology adopted for achieving the objectives. These includes the design, development, calibration of the creep testing setup, detailed experimental procedures, material characterization techniques and ANN

TH-1394_09610307

technique for predicting the creep curves using the data obtained from the limited experiments.

- The results and discussions are presented in chapter-4. Here the tensile properties obtained for the material at various temperatures have been presented. The properties obtained have been discussed with respect to the microstructure and tensile fractographs. The creep life of the material is presented based on Monkman-Grant relationships, Larson-Miller parameter, Manson-Haferd parameter and Orr-Sherby-Dorn parameter. The creep constitutive relations are presented and the deformation behavior is discussed. ANN technique is used to predict creep curves up to 35 % tensile elongation (i.e. 0.3 creep strain). ANN model was used to generate additional creep data for the accurate prediction of creep life by Larson-Miller parameter. The creep life of the investigated material obtained by various techniques was compared.
- Chapter-5 presents the conclusions and future scope of work and references and appendices are followed by.

TH-1394_09610307

LITERATURE SURVEY

2.1 Introduction

HP40Nb micro-alloyed stainless steel is being used extensively as reformer tube material in petrochemical and fertilizer industries to produce hydrogen gas from a mixture of hydrocarbons and steam at elevated temperature [17]. During service, these tubes are continuously exposed to temperature of about 1000 ˚C and gas pressure of 0.5 MPa to 4 MPa for prolonged time in an extremely severe environment [18, 19]. Premature failure of these tubes has been reported to be due to embrittlement and occasional overheating during service. Under the severe service conditions, the most important failure is due to creep deformation.

2.2 Reformer Tube Materials

Reformer tubes are typically made of centrifugally cast heat-resistant alloy steel containing high Cr and Ni as the major alloying elements. During 1960s and 1970s, most of the reformer tubes were cast of HK-40 alloy (25Cr-20Ni-Fe). In 1980s and early 1990s, modification of the alloys by Nb resulted in modified HP alloys [1, 20] with a typical chemical composition (wt. %) of C: 0.35-0.45, Cr: 23-27, Ni: 33-36, Mn: 1-1.5, Si: 1-2, Nb: 0.8-1.2 and balance Fe [3, 21-26]. From the mid of 1990s, micro-alloying elements like Ti, Ta, Zr are being used to improve the high temperature creep properties for service temperatures up to 1000 °C. These alloy steels are extensively used in petrochemical industries as catalyst tubes, radiation tubes and ethylene pyrolysis tubes [21-24].

The microstructure of these materials is characterized by dendritic structure with carbide network at interdendritic regions [27-29]. The creep resistant properties are strongly dependent on the amount of carbides in the matrix [30].The carbides in these materials are mainly Cr-rich (Cr_7C_3) and Nb-rich (NbC) particles [31, 32]. At high service temperature Cr_7C_3 precipitate converts to $Cr_{23}C_6$ [33] while NbC carbides are stable in term of chemical composition and morphology [34]. It has been reported that prolonged service exposure of the steel at high temperatures result in the presence of $Cr_{23}C_6$ at the outer surface of the tubes while the inner surface with the mixture of $Cr_{23}C_6$ and Cr_7C_3 are present [35-37].Addition of 0.8-1.2 wt. % Nb and Ti as micro-

TH-1394_09610307

alloying element stabilize the microstructure at service temperature against transformation of Cr_7C_3 to $Cr_{23}C_6$ by forming NbC precipitate. At 1000 °C, $Cr_{23}C_6$ carbide decomposes and chromium diffuses in to the Nb-rich carbide region to form CrNbC [38]. Long-term service exposure at elevated temperature results in chromium depletion in the matrix and coarsening of interdendritic carbides [19].

Service exposure at 950 °C for ~11 years degraded the tensile strength of these materials [27, 29]. This was attributed to a combination of matrix softening, coarsening of carbides at dendritic grain boundaries and disappearance of fine intra-dendritic precipitate degraded [39]. Tensile strength of HP40Nb steel at 900 °C increased and it almost constant beyond 1500 h of aging due to the transformation of unstable Cr_7C_3 to stable $Cr_{23}C_6$ carbide, whereas, Charpy impact strength continuously decreased with increase in aging time [19]. It was reported that at elevated temperatures the mechanical properties increase with the increase in carbon content. However, at these temperatures, the coarsening of Cr-rich carbides result in reduced ductility of the steel.

The principal failure mechanisms in reformer tubes exposed to high temperatures are due to one or more of the creep damage mechanisms like (a) microstructural degradation, (b) high temperature fatigue, (c) creep-fatigue, (d) embrittlement, (e) hydrogen damage, (f) graphitization, (g) thermal shock, (h) erosion, and (i) high temperature corrosion [40]. Chromium-rich precipitates are more prone to form cavities and micro-cracks than Nb-rich carbides of HP40Nb micro-alloy steels [27].To achieve the design life of this material, an optimum combination of temperature, pressure and alloy is essential.

2.3 Creep Deformation

Creep is defined as the time dependent deformation of a material. The basic information regarding the creep deformation of any material can be understood from a creep curve developed experimentally for a particular combination of stress and temperature. In this the dimensional changes occurring in the material with time is recorded till failure. The total strain ε_{total} at any instant is the sum total of the initial strain on loading ε_o and the time-dependent strain (creep strain) ε_c. The creep data is generated based on the following applications [41]:

TH-1394_09610307

1. Displacement-limited applications, where precise dimensions or small clearances must be maintained (eg. turbine blades, Figure 2.1(a)),
2. Rupture-limited applications, where dimensional tolerance is relatively unimportant, but fracture must be avoided (eg. pressure piping, Figure 2.1(b)),
3. Stress-relaxation-limited applications in which initial tension relaxes with time (eg. cables or bolts, Figure 2.1(c)), and
4. Buckling–limited applications for slender columns or panels carrying compressive loads (eg. wing skin of an aircraft, Figure 2.1(d)).

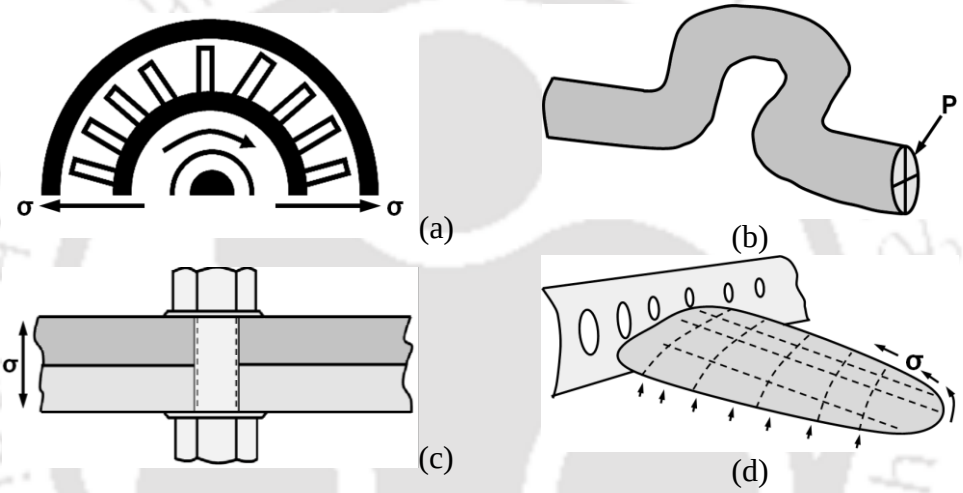

Figure 2.1 Importance of creep in four classes of design; (a) displacement-limit, (b) failure-limit, (c) relaxation-limit and (d) buckling-limit.

The creep curve is a plot of the strain vs. time for constant stress and temperature and is independent of the application. A typical creep curve is illustrated in Figure 2.2.

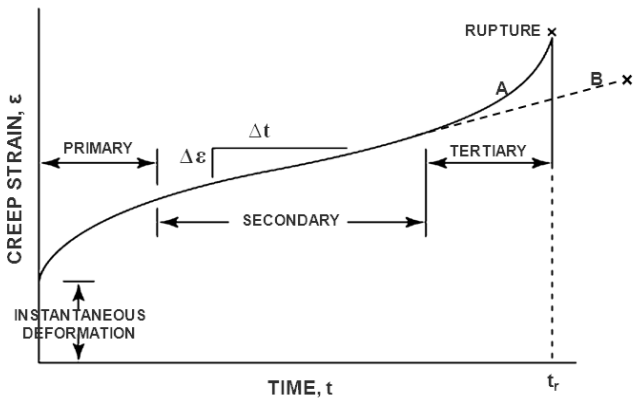

Figure 2.2. Typical creep curve showing the three steps of creep. Curve A: constant-load test and Curve B: constant-stress test [42].

TH-1394_09610307

The instantaneous strain is purely elastic and can be obtained from $\varepsilon = \sigma/E$, where E is the Young's modulus, σ is the applied stress and ε is the elastic strain. The creep curve in Figure 2.2 depicts three regimes as follows:

1. *Primary creep*, where the strain rate decreases with time due to strain hardening. Primary creep is a period of predominantly transient creep in which the creep resistance of the material increases by virtue of its own deformation.
2. *Secondary creep*, where the strain increases linearly with time and is a region of constant strain rate. In this region, a balancing between the competing processes of strain hardening and recovery exists and is also referred as steady state creep region. For design engineers this is the region of prime importance and comprises the maximum creep life.
3. *Tertiary-creep*, where the strain increases at an increasing rate with time, resulting in the final rupture. The tertiary creep is characterized by an effective reduction in cross–sectional area either because of necking or internal void formation. The time to failure is often called the time to rupture or rupture life t_r.

The typical variation in creep rate vs. total strain for the three creep regions is plotted in Figure 2.3.

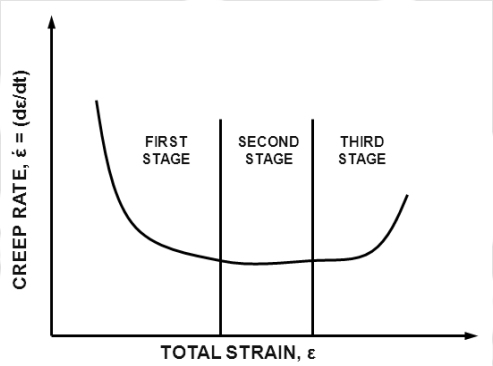

Figure 2.3. Schematic representation of strain rate in creep test as function of total strain [42].

2.4 Creep Curve Models

Various researchers have tried to explain the creep curve behavior. Andrade's creep model is being widely accepted which is based on the superposition of a transient creep and a viscous creep after the sudden strain, as illustrated in Figure 2.4. The creep rate in the transient creep decreases with time whereas the viscous creep continuously increases with time.

TH-1394_09610307

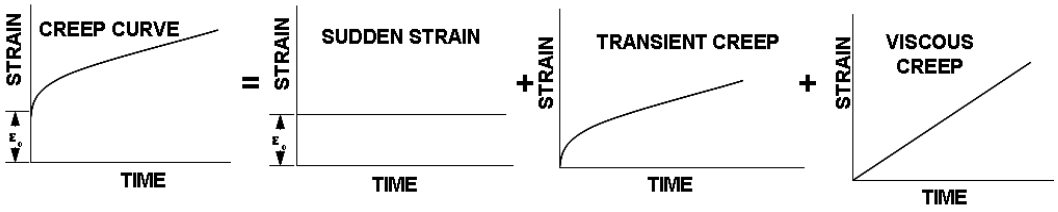

Figure 2.4. Andrade's analysis of the competing processes which determine the creep curve [42].

The creep curve can be represented by an empirical relation [42]:

$$\varepsilon = \varepsilon_0 \left(1 + \beta t^{\frac{1}{3}}\right) e^{(\kappa t)} \tag{2.1}$$

where ε is the strain in time t and β & κ are constants and ε_o is the instantaneous strain during the application of the external load. Table 2.1 highlights various mathematical expressions proposed by researchers for the three creep regions.

Table 2.1. Classical representations of primary, secondary and tertiary creep.

Model Equation	Reference
Primary creep	
Power law: $\varepsilon_p = At^p \rightarrow \varepsilon_p = A\sigma^n t^p$	43
Logarithmic: $\varepsilon_p = A_1 \log(1+bt)$	44
Exponential: $\varepsilon_p = A_2(1 - \exp(-ct))$	45
Sinh law: $\varepsilon_p = A_3 \sinh\left(ct^{\frac{1}{3}}\right)$	46
Secondary creep	
Power law: $\dot{\varepsilon}_s = A_4\sigma^n$	47
Sinh law: $\dot{\varepsilon}_s = \dot{\varepsilon}_o \sinh\left(\frac{\sigma}{\sigma_o}\right)$	48, 49
Tertiary creep	
Exponential: $\varepsilon_t = A_5\left[\exp(-mt) - 1\right]$	50 51
$\dot{\varepsilon}_t = \frac{a\sigma^n}{(1-\omega)^q}$, where $\dot{\omega} = \frac{c\sigma^k}{(1-\omega)^r}$	52
Omega: $\dot{\varepsilon}_t = \dot{\varepsilon}_o \exp(\Omega\varepsilon)$	53

TH-1394_09610307

The nature of the creep curve is heavily dependent on the stress and temperature [54-57]. The variation of the creep curve for constant stresses and temperatures are shown in Figure 2.5(a) and (b), respectively. These figures indicate that high stresses and high temperatures reduce the extent of primary creep stage, eliminate the secondary creep stage and creep rate accelerates almost from the beginning of the creep test. At intermediate stresses and temperatures, the primary and secondary creep stages are more prominent. At lowest stress and temperature, creep curves show long and well defined secondary creep stage with a very slow creep rate.

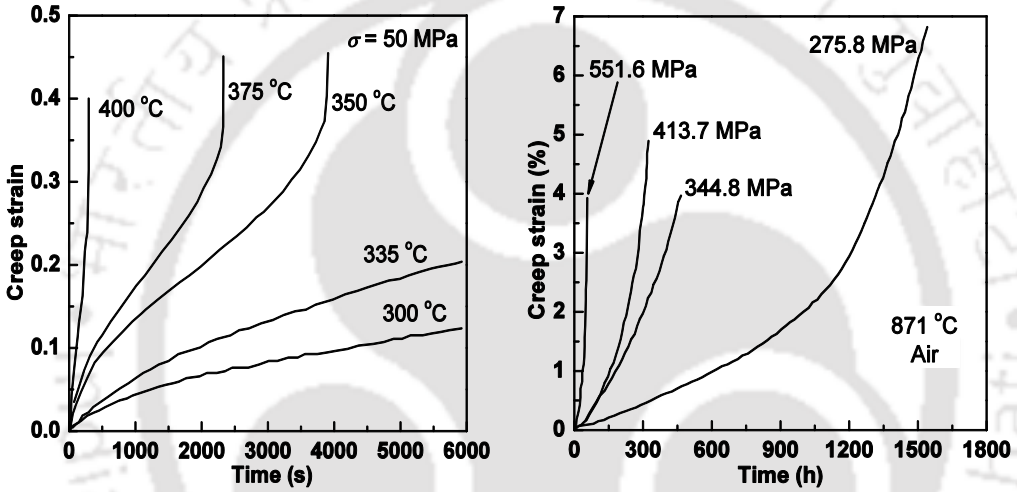

(a) (b)

Figure 2.5. Creep curves (a) of NiTaC-13 at constant temperature [54] and (b) of 5083 Al at constant stress [58].

2.5 Constitutive Equations for Steady State Creep

As mentioned earlier, a typical creep curve consists of three regions. The effective creep life of the material is determined from the secondary creep region where the creep rate remains constant for the major part of the creep life. This region experiences the minimum creep rate which is all referred to as the steady state creep rate $\dot{\varepsilon}_s$. For all practical purpose, the creep life design is based on the time elapsed where the material reaches the end of the secondary creep region or enters the tertiary creep region. This is taken in to account by estimating the minimum creep rate and the creep strain under the service conditions. The various constitutive models for the minimum creep rate proposed by researchers are presented in Table 2.2.

TH-1394_09610307

Table 2.2. Constitutive equations for strain rates proposed by several researchers.

Constitutive equation for strain rate, $\dot{\varepsilon}$ (s^{-1})	References
$\dot{\varepsilon}_s = A_0\left(\frac{\sigma}{G}\right)^{n-1}\left(\frac{\sigma q}{kT}\right)e^{\left(-\frac{H_c}{RT}\right)}$	59
$\frac{d\varepsilon}{dt} = A_1\sigma^n \exp\left(-\frac{Q_c}{RT}\right)$	60-66
$\frac{d\varepsilon}{dt} = \frac{A_2}{T}\sigma^n \exp\left(-\frac{Q_c}{RT}\right)$	56
$\frac{d\varepsilon}{dt} = A_4\left(\frac{\sigma}{\sigma_o}\right)^{n_1} \exp\left(-\frac{Q_{c_1}}{RT}\right) + A_5\left(\frac{\sigma}{\sigma_o}\right)^{n_2} \exp\left(-\frac{Q_{c_2}}{RT}\right)$	64, 66
$\frac{d\varepsilon}{dt} = A_3\left(\sinh B\sigma\right)^n \exp\left(-\frac{Q_c}{RT}\right)$	67, 68
$\dot{\varepsilon}_s = A_6 \exp\left(-\frac{\Delta H}{kT}\right)\times \sinh\left(\frac{q\sigma}{kT}\right)$	68-71
$\dot{\varepsilon}_s = \frac{1}{2}A_7 \exp\left(-\frac{H - q\sigma}{kT}\right)$	72
$\dot{\varepsilon}_s \propto \exp\left\{\left(-\frac{Q_c}{RT}\right)\left(1-\frac{\sigma G_0}{\sigma_0 G}\right)\right\}$	73
$\dot{\varepsilon}_s = A_8\left(\frac{b}{d}\right)^p\left(\frac{D}{b^2}\right)\left(\frac{\sigma}{E}\right)^n$	74
$\frac{d\varepsilon}{dt} = A_9 \exp\left(-\frac{Q_c}{RT}\right).\sinh\left(\frac{q\sigma}{RT}\right)$	70, 75
$\dot{\varepsilon}_s = A_{10}\sigma^m$	76-78
$\dot{\varepsilon}_s = \frac{A_{11}Gb}{kT}\left(\frac{b}{d}\right)^p\left(\frac{\sigma}{G}\right)^n D_0 \exp\left(-\frac{Q_c}{kT}\right)$	56, 79
$\dot{\varepsilon}_s = A_{12}\sigma^n \exp\left(-\frac{Q_c}{RT}\right)$	80
$\dot{\varepsilon} = A_{13} \exp-\left(\frac{Q_c - \beta\sigma}{kT}\right)$	81
$\dot{\varepsilon}_p = \frac{d\varepsilon_p}{dt} = \dot{\varepsilon}_0 \exp-\left(\frac{Q_c - \bar{\tau} q}{kT}\right)$	82
$\dot{\varepsilon}_s = \nu\left(\frac{b}{d_s}\right)\exp\left(-\frac{Q_{sd}}{kT}\right)\exp\left(\frac{\sigma b^2 \lambda}{kT}\right)$	83

TH-1394_09610307

$\dot{\gamma}_s = \frac{b^2(z-1)\nu}{h}\rho_s \exp\left(-\frac{Q_{sd}}{kT}\right).\sinh\left(\frac{\tau_a b^2 \lambda}{hkT}\right)$	84
$\dot{\varepsilon}_s = 2\pi\rho_s D_{sd}\varphi\left(\frac{b}{a_0}\right)^3 \sinh\left(\frac{\sigma b^2 \lambda}{2kT}\right)$	85
$\dot{\varepsilon}_s = A' \frac{DGb}{kT}\left(\frac{\sigma}{G}\right)^2\left(\frac{\sigma-\sigma_i-\sigma_T}{G}\right)$	86
$\dot{\varepsilon}_s = A' \frac{DGb}{kT}\left(\frac{\sigma-\sigma_i-\sigma_T}{G}\right)^3$	
$\dot{\varepsilon} = A\left(\frac{b}{d}\right)^p D_{eff}\left(\frac{Eb^3}{kT}\right)^q\left(\frac{\sigma}{E}\right)^n$	87

The creep constitutive equations for the steady-state creep rate for metals are based on the physical and metallurgical behavior of these materials [57]. Out of the various models, the widely used relationships are the power law approach [60], Dorn approach [88] and Prandlt approach [48]. Weertman [60] in 1955 derived a theoretical equation for minimum creep rate $\dot{\varepsilon}_s$ based on the concept of dislocations climbing over obstacles like sessile dislocations for low applied stresses. In this, the power law expression of the form

$$\dot{\varepsilon}_s = A_1 \sigma^{n_c} \exp\left(-\frac{Q_{app}}{RT}\right) \tag{2.2}$$

At high stresses and high temperature, Dorn proposed the expression for minimum creep rate $\dot{\varepsilon}_s$ as

$$\dot{\varepsilon}_s = A_2 \exp(\beta\sigma) \exp\left(-\frac{Q_{app}}{RT}\right) \tag{2.3}$$

Prandlt (1928) [48] proposed the hyperbolic sine function for the minimum creep rate at high stress as

$$\dot{\varepsilon}_s = A_3 [\sinh(\alpha\sigma)] \exp\left(-\frac{Q_{app}}{RT}\right) \tag{2.4}$$

In Eq. 2.2, 2.3 and 2.4, A_1, A_2, A_3, n_c, β and α are material constants, σ is the applied stress, Q_{app} is the apparent activation energy for creep, R is the universal gas constant (= 8.314 J K^{-1} mol^{-1}), and T is the test temperature. Material constant n_c is also called stress exponent. Eq. 2.4 can be written as

$$\dot{\varepsilon}_s = A_3 \left(\frac{e^{\alpha\sigma} - e^{-\alpha\sigma}}{2}\right) \exp\left(-\frac{Q_{app}}{RT}\right) \tag{2.5}$$

TH-1394_09610307

The value of $e^{-\alpha\sigma}/e^{\alpha\sigma}$ tends to zero when $\alpha\sigma \geq 1.5$, which is generally satisfies in practice [89]. The Eq. 2.5 then assumes the form

$$\dot{\varepsilon}_s = A_3 \left(\frac{e^{\alpha\sigma}}{2}\right) \exp\left(-\frac{Q_{app}}{RT}\right) \tag{2.6}$$

2.5.1 Activation Energy for Creep

Investigation of various materials by investigators reveals that the value of the activation energy for creep is almost equal to the activation energy for self-diffusion Q_c. It is also observed that Q_c is dependent on temperature [74, 90-100] and stress [78, 92, 94, 97, 101-103]. Activation energy for creep for a polycrystalline pure metal shows three ranges with change in range of temperature, as illustrated in Figure 2.6.

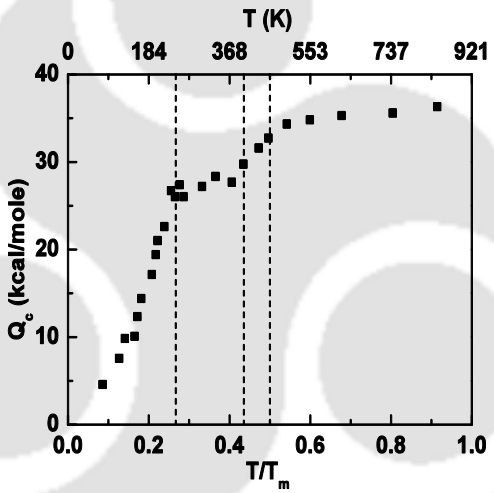

Figure 2.6. Activation energy for creep of polycrystalline aluminium as a function of temperature for creep rates in the range 10^{-6} to 10^{-4} sec^{-1} [74].

At low temperature range (range I) creep occurs due to dislocation of intersection processes [94], in range II by cross-slip and in higher temperature range (range III) by dislocation climb [94]. It is observed that activation energy Q_c depends on the strain rate [104]. Apparent activation energy is close to the value for diffusion along grain boundaries or by dislocation pipes at low temperature [105]. Table 2.3 summaries the activation energy for creep determined from the creep data for different materials.

TH-1394_09610307

Table 2.3. Activation energy for creep of different metals.

Metal	Q_c (kJ/mol)	References
Be (99.7%)	271.96	106
Al (99.99%)	142.26to 150.62	107, 109
Al – Mg	150.62	108, 109
Al – Cu Solid	150.62	108, 109
Al (99.99%)	150.62	110
Ti (99.6%)	251.04	111
Ni (98.7%)	273.63	112
Cu (pure)	184.10	113
Nb (99.8%)	313.80	114

The activation energy reported for the lattice diffusion of austenite phase is 270 kJ/mol [115]. An activation energy for creep of 260 kJ/mol and 340 kJ/mol have been reported for 304L stainless steel and AISI 310S stainless steel [116- 117], respectively. Yamane et al. (1984) [118] and Ruano et al. (1985) [119] observed that activation energy for creep increases with increase in grain size. Holmström (2010) [120] found that the apparent activation energy Q_{app} for P91 steel at a constant stress increased with increase in temperature. The activation energy for creep determined from power law expression of Nb modified HP steel is 331 kJ/mol which increases to 450 kJ/mol for temperatures above 920 °C [121].

2.5.2 Stress Exponent or Power-law Creep Index

In pure metals at high temperatures near the absolute melting temperature T_m, two transitions in creep behavior are observed. Harper-Dorn dislocation creeps occur at low stresses. The Harper-Dorn creep occurs for both high temperature creep, where lattice diffusion predominates and for low temperature creep, where diffusion along dislocation is predominant. In this condition, the stress exponent n_c is equal to 1. At high temperatures intermediate stresses, Coble diffusion creep or Nabarro-Herring creep [122] dominates and occurs due to a recovery process such as high temperature climb. In this condition, the stress exponent n_c is found to be equal to 5. With further increase in stresses, the power-law break-down and the creep prevails. At low stresses, the metal deforms by Harper-Dorn creep [122] in coarse grained materials, whereas, in fine grain sized materials, it is by diffusion creep and the strain rates are high [123].

TH-1394_09610307

Mohamed and Langdon (1974) [124, 125] and Langdon (1981) [126] found that solid solution alloys exhibit a transition from pure metal-alloy-pure metal. This transition can explain the creep mechanism of the metal which is illustrated in Figure 2.7.

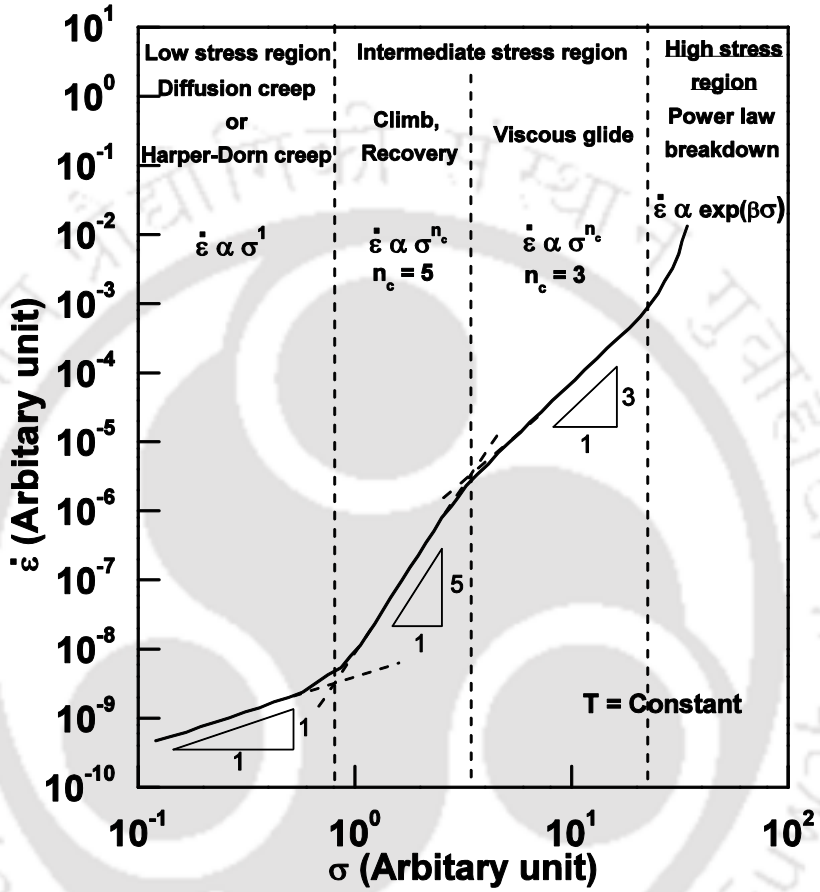

Figure 2.7. Schematic illustration of strain rate versus stress showing pure metal–alloy transition in solid solution alloys [127].

It has been found that a linear correlation exist between n_c and dimensionless material parameter A [128]. The magnitude of n_c depends on temperature (linear function of $1/T$) and the material and for iso-structural, iso-thermal case n_c is a constant [129, 130]. The value of n_c of HP-modified Nb steel under low and high stress is 6 and 19, respectively [121].

2.6 Creep Deformation Mechanisms

Creep deformation mechanisms are generally classified as dislocation glide, dislocation creep, diffusional creep and grain boundary sliding. Dislocation glide mechanism occurs at high stress, $\sigma/G > 10^{-2}$, dislocation creep (power-law behavior)

TH-1394_09610307

occurs for $10^{-4} < \sigma/G < 10^{-2}$ and diffusion creep (linear-viscous creep) occurs for $\sigma/G < 10^{-4}$. Grain–boundary sliding involves the movement of dislocations due to shear in the direction of grain boundary by increasing the temperature and/or decreasing the strain rate. The dislocation creep and diffusion creep are assisted by mass diffusion and follow Arrhenius's type expression.

2.7 Deformation Mechanism Maps

The creep behavior of materials can differ under different stress/temperature conditions. Ashby (1972) [121] first introduced the creep deformation mechanism map. These maps are graphical representation of regimes of various creep phenomenon on a normalized stress- normalized temperature plane as illustrated in Figure 2.8(a). These maps are divided into five regions of stress and temperature over which each of the deformation mechanisms is dominant. Contours of constant strain rate are superimposed in these maps which show the net strain rate (due to an appropriate superposition of all the mechanisms) at a given combination of stress and temperature. The deformation mechanism map reveals the relationship between stress, temperature and strain rate. Any one of these variables can be determined from the map if any pair of these variables is specified and the mechanism can be identified.

The deformation mechanism maps are divided into different fields based on the dominant creep mechanism. The field boundaries are obtained by equating pairs of the constitutive equations of two adjacent creep mechanisms. A deformation mechanism map with the contour plot of strain rate for tungsten is shown in Figure 2.8(b). The constitutive equations used for constructing these maps are given in Table 2.4.

Deformation mechanism maps for pure aluminium, UC, cobalt, silicon carbide, alkali metal potassium, indium antimonide (InSb), IN738LC superalloy were constructed by researchers [125-143].

TH-1394_09610307

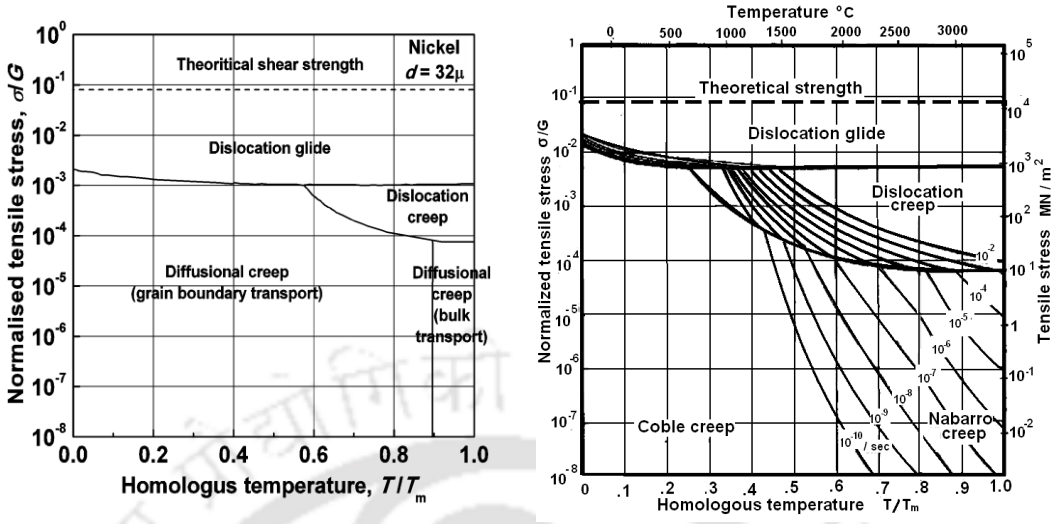

(a) (b)

Figure 2.8. Deformation mechanism map for (a) pure nickel and (b) pure tungsten [121].

Table 2.4. Constitutive equations used for constructing deformation mechanism maps [124, 125].

Mechanism	Constitutive Equation for strain rate, $\dot{\varepsilon}$ (s^{-1})
Climb	$\dot{\varepsilon} = 2.5\times10^{6}\frac{D_l G b}{kT}\left(\frac{\sigma}{G}\right)^{4.4}$
Harper – Dorn	$\dot{\varepsilon} = 1.67\times10^{-11}\frac{D_l G b}{kT}\left(\frac{\sigma}{G}\right)$
Nabarro – Herring	$\dot{\varepsilon} = \frac{B\Omega\sigma D_l}{d^2 kT}$
Coble	$\dot{\varepsilon} = \frac{150}{\pi}\frac{\Omega\sigma\delta D_{gb}}{d^3 kT}$

2.8 Fracture Mechanism

Creep seldom occurs at low temperatures, whereas at high temperature it terminates in fracture. In the creep curve, onset of tertiary creep is the deviation from the constant creep rate, which ultimately results in creep failure. During the constant stress test, tertiary stage normally precedes fracture. Tertiary creep may be caused by

(a) mechanical instability, such as the occurrence of necking which results in a localized reduction in cross-sectional area,

TH-1394_09610307

(b) microstructural instability, including grain growth or recrystallisation with single phase materials or the gradual loss of creep strength as over-ageing occurs during creep of precipitation-hardened alloys and/or

(c) nucleation and growth of internal micro-cracks which develop until the numbers and sizes of the micro-cracks are sufficient to cause the creep rate to increase.

The solid may fail by transgranular creep fracture (T.C.F.) or by intergranular creep fracture (I.C.F.) mechanisms. At temperatures approaching the melting point, many materials undergo dynamic recrystallization resulting in rupture or necking to zero cross-sections. At high temperature creep conditions, micro-cracks form and grow along grain boundaries, so that failure occurs in an "intergranular" manner. Two forms of intergranular cracking are commonly observed. Wedge-shaped cracks (*w*-type cracking) or triple point cracks often found at high stresses and intergranular cracks developing at low stresses by nucleation. These nucleated cracks grow and form round or elliptical cavities (*r*-type cracks) and link-up at grain boundaries (shown in Figure 2.9) to cause the final failure. Large stress concentrations exist when the growth of these cavities are impeded by small obstacles. The obstacles leading to cavity formation are believed to be due to:

(i) ledges or steps formed where a slip band in one grain intersects the boundary, or

(ii) non-deformable particles or hard inclusions at grain boundaries.

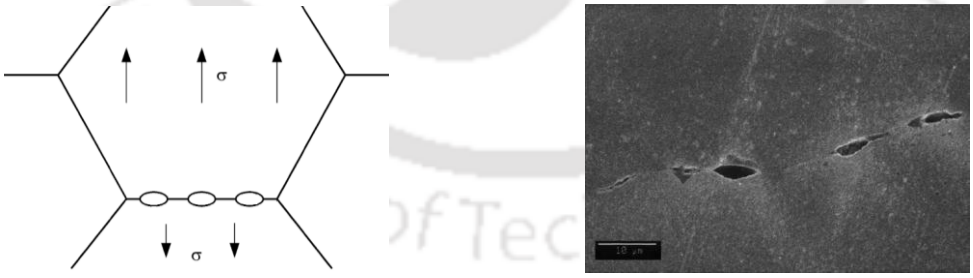

(a) (b)

Figure 2.9. (a) Cavitation (*r*-type) or voids at a transverse grain boundary and (b) micrograph of cavities in copper [142].

Grain boundary sliding results in shear stress leading to stress concentrations large enough to nucleate cracks at triple points. Further sliding causes the cracks to grow predominantly along grain boundaries and normal to the tensile stress axis is illustrated in Figure 2.10. Grain boundary sliding is responsible for the nucleation as well as the continued growth of the cavities. At high temperature creep conditions, the grains

TH-1394_09610307

within a polycrystalline material move relative to each other and form wedge or triple point cracks. i.e., *w*-type cracking initiated by grain boundary sliding. Cavities grow by diffusion when they are small, but as they increase their size, power-law creep becomes the dominant growth mechanism. As the strain rate is decreased or the temperature is raised, the *r*-type cavitation is favoured over the *w*-type. The relative movement of two adjacent grains in a polycrystalline array results in deformation of the surrounding grains, so that sliding can occur only at the rate permitted by grain deformation. The rate of grain boundary sliding and the rate of wedge crack development are then determined by the overall creep rate.

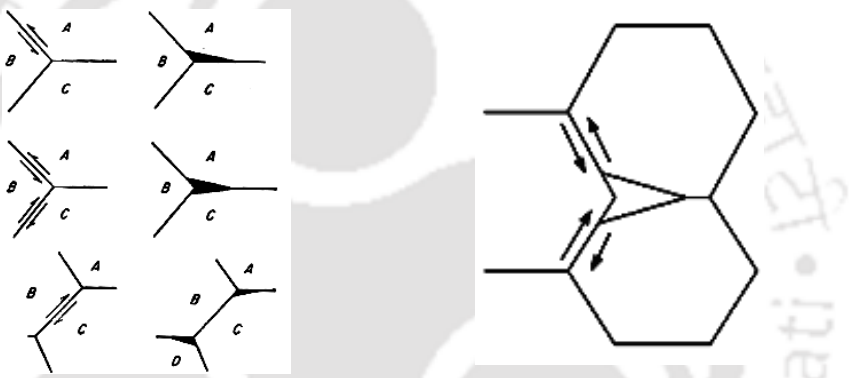

(a) (b)

Figure 2.10. Schematic drawings of (a) the way intergranular cracks form due to grain boundary sliding [42] and (b) wedge (or *w*-type) crack formed at the triple junctions.

When a cylindrical bar of a crystalline solid is pulled in tension, it fails in one of several ways as shown in Figure 2.11 [143]. It shows seven mechanisms of fracture in metals and alloys *viz.*, fracture at the ideal strength, cleavage, ductile fracture at low temperature, transgranular creep fracture, intergranular or creep-controlled fracture, pure diffusional fracture and rupture.

TH-1394_09610307

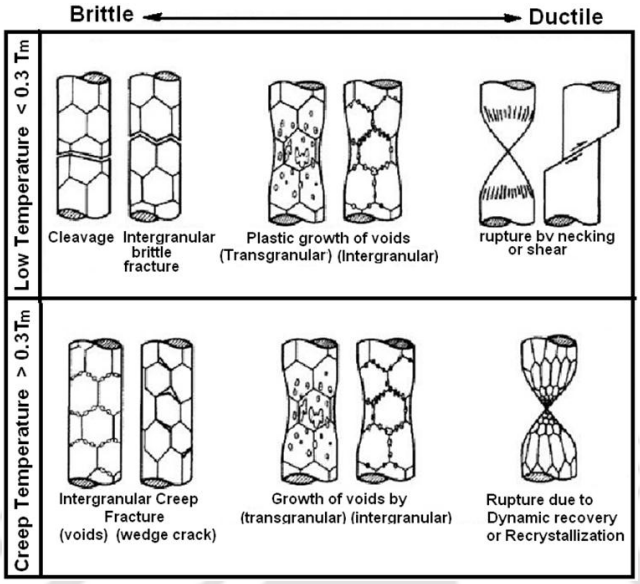

Figure 2.11. Simplest classification of creep fracture mechanisms [143].

Though the creep fracture mechanisms have been investigated in a wide range of materials, the correlation between the minimum creep rate and rupture time at constant temperature and stress is required for the successful design of the component. This correlation can be obtained by the Monkman-Grant relationships which are discussed in the subsequent sub-section.

2.9 Monkman-Grant Relationships and Creep Damage Tolerance Factor

The Monkman-Grant relationship (MGR) correlates the minimum creep rate $\dot{\varepsilon}_s$, to the time to failure t_r in materials undergoing creep failure. MGR can be [144] expressed as

$$\dot{\varepsilon}_s^{\,m} . t_r = C \tag{2.7}$$

where m and C are constants. Eq. 2.6 is useful in predicting the rupture time of a component by using short time creep test data. Available data for a wide range of alloys indicate that the values of m *and* C lie in the range 0.6 - 0.95 and 3 - 20, respectively [145-148]. Kim et al. (2000) [149] reported m in the range of 1-1.3 for type 316LN steel. Studies have revealed C to be dependent on temperature [150]. Toscano and Boček (1981) [151] reported m and C are function of stress and temperature. Considering the scatter in the experimental data, Dobes and Milicka (1976) [152]

TH-1394_09610307

introduced a failure strain ε_f term in Eq. 2.7 and proposed the modified Monkman-Grant relation (MMGR) in the form

$$\dot{\varepsilon}_s^{\,m\prime}.\frac{t_r}{\varepsilon_f} = C' \tag{2.8}$$

where *m'* and *C'* are constants. MMGR was validated for different alloys by investigators [147,153-165]. When $m = m' = 1$, Eq. 2.7 and Eq. 2.8 can be represented as

$$\dot{\varepsilon}_s.t_r = C_{MG} \tag{2.9}$$

and

$$\dot{\varepsilon}_s.\frac{t_r}{\varepsilon_f} = C_{MMG} \tag{2.10}$$

Eq. 2.9 indicates that the rupture time is inversely proportional to the minimum creep rate whereas the Eq. 2.10 indicates an inverse relationship of minimum creep rate with $\dot{\varepsilon}_s/\varepsilon_f$. Since, C_{MMG} was found to be more sensitive to cavity growth, the residual creep life could be predicted more accurately using C_{MMG} compared to that by C_{MG} [166].

Monkman-Grant relationship is based on the creep damage following first order kinetics and is valid for all the three creep stages [159, 162, 167-169]. Phaniraj et al. (2003, 2005) [157, 170] referred the Monkman-Grant Ductility (MGD) as the product of secondary creep strain rate $\dot{\varepsilon}_s$ and rupture time t_r. Since the MGD is the secondary creep strain contribution to total creep strain, it can be considered as the minimum creep ductility for materials undergoing creep deformation. Time to reach MGD t_{MGD}, the time for attaining a critical level of damage, is the useful creep life of the component. Based on continuum creep damage mechanics (CDM), Kachanov (1958) [52] and subsequently Rabotnov (1969) [51] considered creep damage as an internal state variable ω. CDM approach was further extended [171-176] to describe the coupling between creep deformation and damage by introducing a creep damage tolerance factor λ. λ was defined as the ratio of ε_f to Monkman-Grant ductility $\dot{\varepsilon}_s t_r$, expressed as

$$\lambda = \frac{\varepsilon_f}{\dot{\varepsilon}_s t_r} \tag{2.11}$$

From Eq. 2.10 and Eq. 2.11 it is evident that λ is the reciprocal of C_{MMG} [157] and is a useful parameter to assess the creep ductility of a material [172, 177]. Based on critical damage criterion, Phaniraj et al. arrived at a universal relationship between t_r and t_{MGD} in the form

TH-1394_09610307

$$\frac{t_{MGD}}{t_r} = 1 - \left(\frac{\lambda - 1}{\lambda}\right)^{\lambda} = Constant = f_{CDM} \quad (2.12)$$

Eq. 2.12 is applicable to materials where the mechanism of creep failure is dominated by cavitation. As the creep time approaches t_{MGD}, the cavity attains a critical value and the deformation enters the tertiary stage [170]. During tertiary creep, the creep rate increases at a faster rate by void growth and coalescence resulting in final failure of the component.

2.10 Creep Rupture Models

Creep strength is an important consideration for the life of structures which are to be exposed to elevated temperatures and stresses for extended periods of time. In order to maintain the creep strain well below the creep rupture strain, stringent conditions on the allowable stress are placed at locations where creep is a potential problem. In applications where weight is not of importance, this is often achieved by overdesigning the structure to minimize creep.

The creep life of structural components can be determined from the standard creep curve. However, it is unrealistic to perform creep tests for the exact service life of the structure because that would take almost more than a decade of uninterrupted creep testing for a single test. There are many recognized methods for extrapolating creep data. Acceleration of creep tests is generally carried out to reduce the test time to a reasonable level. These techniques uses stress and temperature levels significantly higher than the service stresses and temperatures to reach the limiting strain faster. The design life is again determined by developing a number of creep curves at constant stress and temperature and extrapolation of the thus generated data to the design life.

Extrapolation techniques for establishing correlations involving temperature T, time to rupture t_r, and stress σ using data developed from short time tests exists. These are generally based on the Arrhenius type of relationship between creep rate and temperature. This necessitates a number of time–temperature parameters to be determined for the prediction of creep life to longer periods. There are several uncertainties involved in using the accelerated creep test data due to which parametric models have been developed. In these techniques, it is assumed that no change in the structure occurs in the domain consisting of experimental as well as extrapolated region. Since the experimental conditions, *viz.*, stress and temperatures, are much higher than

TH-1394_09610307

the application conditions, these predictions are assumed to be safe. The various time-temperature parameters presently in use are Larson-Miller parameter, Manson-Hafred parameter, Orr-Sherby-Dorn parameter, etc. These are explained briefly in the subsequent sub-sections.

2.10.1 Larson-Miller Parameter [10]

Larson and Miller, based on the earlier Hollomon-Jaffee (1945) [178] expression for tempering of steel, first introduced the correlations between rupture time and temperature. For a given material, a plot of stress versus Larson-miller parameter ($P_{L\text{-}M}$ or L-M parameter) resulted in a single plot, regardless of the time–temperature combination. A value of Larson-Miller constant $C_{L\text{-}M}$ = 20 was initially proposed, but optimized values between 10 and 40 have subsequently been found to be suitable depending on the material. In common usage, T is taken in absolute unit (in K) and t_r in hours. This parameter can be readily derived from the stress and temperature dependence of the creep rate or time to rupture. Larson–Miller parameter $P_{L\text{-}M}$ can be expressed as:

$$P_{L\text{-}M} = f(\sigma) = T(\log_{10} t_r + C_{L\text{-}M}) \tag{2.13}$$

where $C_{L\text{-}M}$ is a constant. The detail derivation of Larson-Miller parameter is given in Appendix-I.

A plot of $\log_{10} t_r$ vs. $1/T$ for constant stresses, as shown in Figure 2.12(a), results in straight lines which are assumed to intersect at a point $C_{L\text{-}M}$ where $1/T$ approaches zero. The slope of the iso-stress lines (Q_c/2.3R) is a function of stress. In the analysis, the value of $C_{L\text{-}M}$ in Eq. 2.13 is always taken as constant and depends on the material. The time can either be the time to creep rupture or the time to a given creep strain level. A stress vs. Larson-Miller parameter master curve is obtained which is used for predicting the creep life of the material. A typical master curve obtained for 35Ni-25Cr-1Nb-Ti steel is shown in Figure 2.12(b).

TH-1394_09610307

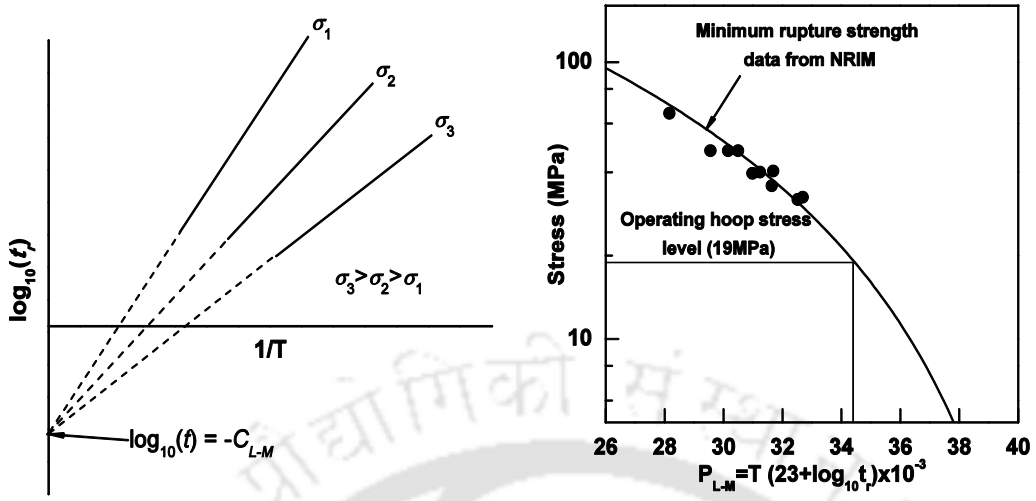

(a) (b)

Figure 2.12. (a) Schematic representation of constant stress lines for P_{L-M} and (b) plots of P_{L-M} against stress for 35Ni-25Cr-1Nb-Ti steel [23].

2.10.2 Manson–Haferd Parameter [12]

The Larson-Miller parameter clearly indicates that at a given stress the parameter $[T(C_{L\text{-}M}+\log_{10} t_r)]$ = constant, then a plot of $\log_{10} t_r$ versus $1/T$ should result in a straight line for a constant stress. The value of $(-C_{L\text{-}M})$ was the value of $\log_{10} t_r$ at point where the value $1/T$ is zero. A careful investigation would reveal that these lines are not intersecting at a single point. Manson and Hafred proposed a technique in which all iso-stress lines intersect at a point (T_a, $\log_{10} t_a$) when plotted on a $\log_{10} t_r$ - T plane. The Manson-Haferd parameter $P_{M\text{-}H}$ (or M-H parameter) in this case is expressed by the relationship:

$$P_{M-H} = f(\sigma) = \frac{(T - T_a)}{(\log_{10} t_r - \log_{10} t_a)} \tag{2.14}$$

The detail derivation of Manson-Haferd parameter is given in Appendix-II. The constant $\log_{10} t_a$ and T_a are the coordinates of the point of intercept, as illustrated in Figure 2.13(a). The $P_{M\text{-}H}$ is plotted against stress to get a linear relationship as shown in Figure 2.13(b). From this master plot the rupture time at a constant stress and temperatures can be determined.

TH-1394_09610307

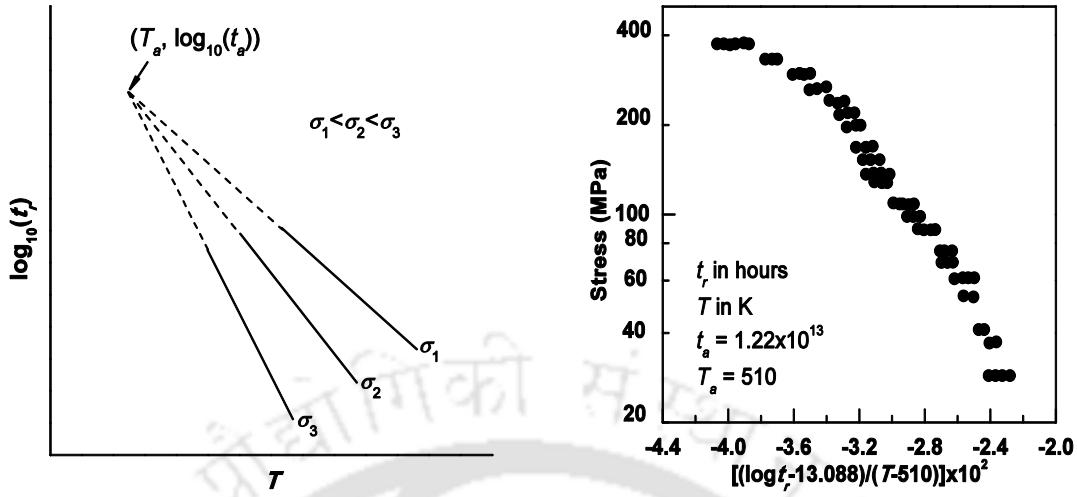

(a) (b)

Figure 2.13. (a) Schematic plot of iso-stress lines for finding constants t_a and T_a and (b) plots of for stress vs. $P_{M\text{-}H}$ for 1Cr-0.5Mo steel [179].

2.10.3 Orr-Sherby-Dorn Parameter [11]

From the fundamental relationship in creep

$$\varepsilon = f(\theta, \sigma) \tag{2.15}$$

where, ε is the total creep strain, σ is the initial stress and θ is the temperature-compensated time $\left[\theta = t\ exp\left(-\frac{Q_c}{RT}\right)\right]$, where, t is the time to reach the strain ε, T is the temperature in absolute degrees, R is the universal gas constant and Q_c is the experimental activation energy. The Eq. 2.15 appears to be reasonably valid up to the point of stress-rupture including the region of formation and growth of micro-cracks. Assuming that the strain damage depends on the applied stress and the creep strain, the Orr-Sherby-Dorn proposed the parameter $P_{O\text{-}S\text{-}D}$

$$P_{O-S-D} = \log_{10} t_r - \frac{Q_c}{2.3RT} \tag{2.16}$$

where $P_{O\text{-}S\text{-}D}$ is the Orr-Sherby-Dorn parameter and Q_c characteristic activation energy for the process which is a function of σ. The detail derivation of Orr-Sherby-Dorn parameter is given in Appendix-III. Figure 2.14(a) shows the plots of $\log_{10} t_r$ vs. $1/T$ as parallel lines for different stresses. The slope of these lines ($-Q_c/2.3R$) remains constant. Stress versus Orr-Sherby-Dorn parametric curve is shown in Figure 2.14(b). From this master plot the rupture time at a constant stress and temperatures can be determined.

TH-1394_09610307

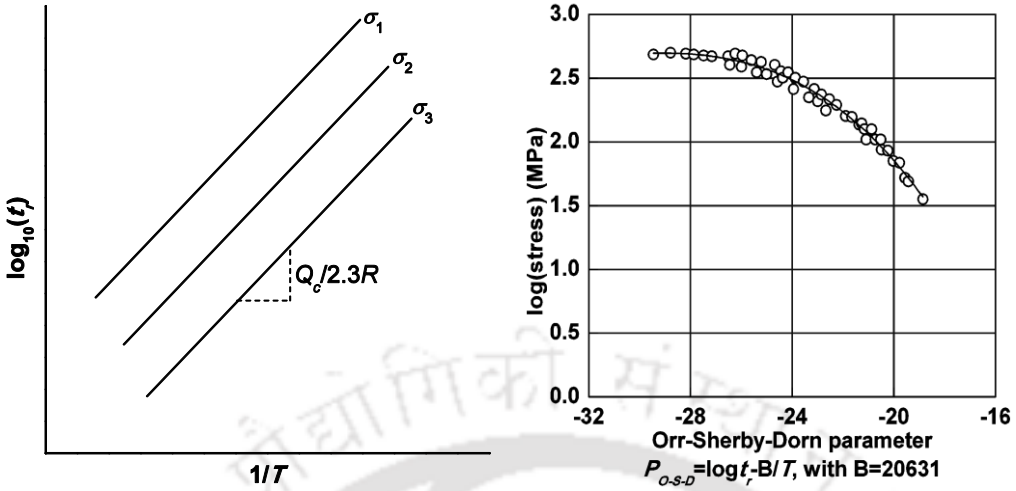

(a) (b)

Figure 2.14. (a) Schematic representation of constant stress lines for $P_{O–S–D}$ and (b) plot of stress versus $P_{O–S–D}$ [180].

Among parametric models, prediction of creep life by Larson–Miller parameter is widely used by engineers. The advantage is that this technique can be used by extrapolating short time data and predicting life of a material. However, prediction of the creep life by all the above mentioned techniques is not very accurate compared to the actual life. The inaccuracy in prediction using $P_{L\text{-}M}$ technique is mainly in choosing the value of the constant "$C_{L\text{-}M}$" in the Eq. 2.12. Engineers use this as a constant value independent of stress. It appears that the $C_{L\text{-}M}$ value should be stress dependent for accurate prediction.

Scientists found there is a huge variation in the constant value of $P_{L–M}$ [181-191] which is equal to 20 as proposed by Larson and Miller (1952) [10] for extrapolating rupture-lives from 1000 hours to greater than 10^5 hours. Subsequent investigation by various investigators revealed $C_{L–M}$ value lying in the range 8 and 57 [191]. A deeper investigation would also reveal that the value of $C_{L–M}$ is dependent on the applied constant stress [192]. Woodford (1977) [54] proposed $C_{L–M}$ to be a function of σ and modified the $P_{L–M}$ as:

$$P_{L-M} = T\left(\frac{2000}{\sigma} + \log t_r\right) \tag{2.17}$$

This expression was found to be reasonably accurate compared to the Eq. 2.12. Furillo et al. (1977) [192] derived $P_{L–M}$ using $C_{L–M}(T)$ using power-law creep function, elastic modulus normalized applied stress [$\sigma/E(T)$] and arrived at an expression for $C_{L–M}$ in the form:

TH-1394_09610307

$$C_{L-M}(T) = \log \frac{\left\{A\exp\left(-\frac{Q_c}{RT}\right)\right\}}{B} \quad (2.18)$$

The material degradation for in-service high-temperature components was estimated by a Larson-Miller parameter which was calculated from aging temperature and aging time [193, 194]. Sobrinho and Bueno (2005) [180] presented that hot tensile data can be used to determine parametric master curves.

Shlyakman et al. (2010) [195] derived a method for determining constant $C_{L\text{-}M}$ in the Hollomon temperature-time parameter [178]. The effect of carbon content on $C_{L\text{-}M}$ value in pearletic heat resistant steel was analyzed based on the Empirical Electron Theory of Solid and Molecules [196, 197]. Service condition-creep rupture property interference (SCRI) model based on Z-parameter method was used by various investigators to determine creep rupture life of materials [198-203].

Reports regarding the creep life assessment by various investigators reveal that the Larson-Miller master curve obtained are different even for same materials. This is due to the fact that the studies were carried out on materials service exposed at different conditions. Ray et al. (2003) [204] estimated remaining creep rupture life of 2 year service exposed HK40 micro-alloyed steel tube by extrapolating Larson-Miller parametric technique. In this a value of $C_{L\text{–}M}$ = 22.9 was found to be suitable. Study by Shannon and Jaske (2003) [205] on HK40 alloy found the value of $C_{L\text{–}M}$ = 15 as suitable. Jahromi and Naghi Khani (2004) [206] investigated remaining life of failed HP40Nb modified steel tube at 870 °C/13.4 MPa by Larson-Miller technique in which $C_{L\text{-}M}$ value used was 17.459 and found the remaining life as 9.2 years. Swaminathan et al. (2008) [29] investigated the remaining life of service exposed HP40Nb micro-alloyed steel tube by Larson-Miller technique. In that the remaining life of the tube was found to be 5 years at 900 °C/22.5 MPa. Their calculation was based on a $C_{L\text{-}M}$ value of 22.9. Ray et al. (2011) [39], by using a $C_{L\text{-}M}$ value of 23 found the remaining life of service exposed HP40Nb micro-alloyed reformer as 3.75 years at 950 °C/19 MPa.

2.11 Artificial Neural Network (ANN) Modeling

A number of physics based models have been successfully applied to solve wide range of engineering problems. These techniques require the precise relationship

TH-1394_09610307

between the input-output variables and boundary conditions. When the number of variables is large and the relationships are nonlinear, the solution by these techniques becomes very complicated and difficult to solve. In the past few decades, soft computational techniques viz., artificial neural network (ANN), fuzzy logic and evolutionary algorithm has emerged as powerful tools for solving complex engineering problems. Artificial neural network technique has successfully been used for solving complicated engineering problems in areas such as metal working, traditional and non-traditional machining, deformation processing, hot working, welding, etc. The advantage of ANN is that it is a data driven model, which is based on analyzing the data about a system, by finding connections between the system state variables (input, internal and output variables). The connections between the state variables can be established in availability of the sufficient input-output data sets, even if the exact physical behaviour of the system is not known. In addition, the solution by ANN is very faster compared to the physics based models.

In 1943, an ANN was first presented by neurophysiologist W. McCulloch and logician W. Pits. A neural network is a biologically inspired computational model which is similar to that of the human nervous system. An artificial neural network (ANN) can be defined as a mathematical technique that models complex linear and non-linear relationships by reasoning similar to the human brain, where a large amount of information can be stored and processed simultaneously by each neuron along the entire domain. This is basically a connectionist system, in which various nodes called neurons are interconnected. A typical neuron receives one or more input signals either externally or from other neurons and passes it through transfer or activation functions and provides an output signal. This output is transferred to connected neurons in varying intensities, the signal intensity being decided by the weights assigned. Once the ANN architecture is fixed, the output for any combination of input variables can be predicted.

Among the various neural network models, the feed forward back-propagation neural network (BPNN) is widely used especially when sufficient data sets are available. This architecture consists of three distinct layers: the input layer, the hidden layer(s) and the output layer. Each layer consists of a number of neurons. The output from the neurons of one layer is transferred as input to neurons of the succeeding layer. The first layer, called an input layer, receives data from the outside world. The second

TH-1394_09610307

layer, called the hidden layer, does not have any direct contact with the outside world. Hidden layer is essential since it allows the network to learn the relationships in the data by extracting higher-level features and facilitate generalization of outputs. Depending upon the complexity of the problem and data sets, one or more hidden layers with several neurons in each layer may be required. However, most of the engineering problem solutions were achieved by one hidden layer architecture. The last layer is the output layer, which sends information out to users.

The back propagation algorithm is a variation of a gradient descent optimization algorithm that minimizes the error between the predicted and actual output values. This algorithm involves two passes. In the forward pass, the input signals propagate from the network input to the output. In this pass, the input vector data are fed to the network at the input layer and propagated with weights and activation functions to the output layer to provide an output. Once the data at the output layer is reached, this value is compared with the actual output value of the input-output data set. The error between the predicted and actual values is computed and the error signals are sent backwards. These error signals propagate backwards from the output layer to the input layer through the hidden layer during which the weights and bias at each neurons are modified to minimize the error. This process is referred to as training. Any efficient optimization method can be used for minimizing the error through weight adjustment. Several different back-propagation training algorithms such as Levenberg-Marquardt (trainlm), Bayesian regulation (trainbr), scaled conjugate gradient (trainscg), resilient (trainrp), gradient descent (traingd), gradient descent with momentum (traingdm), etc. have been applied for training of different pattern recognition and functional approximation problems. Hegan and Menhaj (1994) [207] tested Levenberg-Marquardt algorithm on several function approximation problems and found the algorithm is very efficient.

Once the network has been trained according to the assigned learning rule, it is capable of computing the output values associated with new input vectors. The trained neural network has to be tested by supplying testing data. If the testing error is very high compared to the training error, the network is said to over-fit the data. A properly fitted network will give nearly equal training and testing errors. A summary of previous research work on ANN prediction of mechanical properties are given in the subsequent paragraphs.

TH-1394_09610307

Jones and MacKay (1996) [208] modeled yield and ultimate tensile strength for a range of commercial, wrought, and polycrystalline Ni based superalloys as a function of alloy chemistry and temperature. In a review paper, Bhadeshia (1999) [209] established the application of neural network model for predicting mechanical properties, phase transformation, machining variables, etc. Dumortier and Lehert (1999) [210] used ANN technique to predict yield strength, ultimate tensile strength and elongation of carbon and micro-alloyed steel. Datta et al. (1999) [211] applied ANN technique to predict the mechanical properties of HSLA steel using composition and thermo-mechanical process parameters as the input variables. The yield strength of superalloy as a function of composition and temperature was predicted by ANN modeling by Warde and Knowles (1999) [212, 213]. Huang and Blackwell (2002) [214] explains the process of using an ANN to developed a constitutive relationship for Inconel 718. Haque and Sudhakar (2002) [215] used ANN back-propagation model to predict fracture toughness and tensile strength of DP steel. ANN has also been successfully applied to predict the mechanical properties of materials based on the manufacturing process parameters [216-218].

Recently the application of ANN modeling has also been extended by few authors to predict the creep rupture life of materials [219-226]. Gupta et al. (2007) [227] predicted creep behaviour of a rotating disc made of Al-SiC particulate composite using particle size, particle content and temperature as input and stress and strain rates as output parameters. Sarkar et al. (2014) [228]developed a neural network model to predict diametral creep rate in Zr-2.5%Nb pressure tube using alloy composition (concentration of Nb, O, N and Fe), mechanical properties (yield strength, ultimate tensile strength and percentage elongation), temperature and average flux as an input variable.

Literature reveals the capability of ANN for predicting creep rupture life, creep rate and creep damage classification of high temperature materials. In general, the existing techniques for the prediction of the creep life of materials are by either constitutive relationships or by parametric techniques based on the data generated by carrying out limited creep tests. The prediction capability of these techniques depends on the number of available data. As mentioned in earlier sections, creep tests are very time consuming. The fact that a creep curve is a superimposition of three different creep

TH-1394_09610307

stages having different relationships in each stage complicates the process of generating physics based relationship between the time dependent creep strain, applied stress and temperature. Report regarding prediction of creep curves under various combination of applied stresses and temperatures is so far not available in the literature. Prediction of creep curves by ANN modeling with reasonable accuracy would be a major step in the area of creep of engineering materials. ANN modeling is capable of generating creep curves from limited accelerated creep tests and the data thus generated can be utilized for predicting the remaining creep life of materials by the parametric extrapolation techniques. The present work was therefore carried out to carry out accelerated creep test of HP40Nb micro alloyed steel and to establish the creep deformation behaviour by various models.

2.12 Technical Gaps

Based on the literature survey, the following areas have not been addressed or investigated by researchers.

1. Results of systematic investigation of the temperate dependent mechanical properties and fracture of HP40Nb micro-alloyed reformer tube and its correlation to the microstructure are not available in the literature.
2. The creep behaviour and damage mechanism in this material has so far not been reported. The creep curves for this material for further investigation is also not available in the open literature.
3. Investigation of the creep behaviour of HP40Nb micro-alloyed reformer tube by constitutive relationships has not been studied.
4. The validity of Monkman-Grant relationships in HP40Nb micro-alloyed reformer tube has so far not been established.
5. Modeling of a complete creep curve of metallic materials with reasonable accuracy has not been reported in the literature. It appears that modeling by data driven technique like ANN can predict the creep curve with reasonable accuracy.
6. Larson-Miller parameter technique for predicting the creep life of materials needs to be critically reviewed. Reports reveal that for simplicity, the term $C_{L\text{-}M}$ is always considered as constant and was arrived at by trial and error method. A large variation in the value of $C_{L\text{-}M}$ has been reported for the same materials by various

TH-1394_09610307

authors. However, it appears that that $C_{L\text{-}M}$ is a function of applied stress and hence modification in the Larson-Miller parameter technique needs to be carried out.

7. Comparison of the creep rupture life by different established parametric techniques and constitutive modeling in metallic materials has so far not been carried out.

2.13 Research Objectives

The main objectives of the thesis are as follows.

1. To investigate the tensile creep behavior of HP40Nb micro alloyed reformer tube at different temperatures and stresses.
2. To develop creep constitutive equations, validate the Monkman-Grant relationships and determine the creep damage tolerance factor for the steel.
3. To generate a model and therefore predict creep curve at different stresses and temperatures as a function of applied stress σ, temperature T and time t of the investigated steel by ANN and forecasting creep life of the tube by Larson-Miller parametric technique.
4. To compare the predictability of the creep life of the above material by parametric techniques viz., Larson-Miller parameter, Manson-Haferd parameter and Orr-Sherby-Dorn parameter.
5. To investigate whether the term $C_{L\text{-}M}$ in the Larson-Miller parameter technique for prediction of creep life should be a constant or a function of stress.

In order to meet the above objectives, the investigation carried out as per the following activities:

1. Design and development of a constant creep testing setup.
2. Evaluate the mechanical properties at room and elevated temperatures and its fractography.
3. Carry out creep experiment on HP40Nb micro-alloyed steel at different stress levels varying from 45 MPa to 120 MPa and temperatures varying from 650 °C to 1050 °C and generate creep data at various conditions.
4. Study the microstructure of the material before and after creep test using optical microscope, XRD, SEM, TEM, and EDX.
5. Modeling the creep strain by ANN technique and establish its usefulness in predicting creep curves.

TH-1394_09610307

6. Modeling of creep behavior by constitutive equations and by existing parametric techniques. An attempt was also made to modify the constant $C_{L\text{-}M}$ in the expression for Larson-Miller parameter as a function of applied stress and compare the results with the case where $C_{L\text{-}M}$ is considered a constant.

The present chapter presents the literature summary related to the thesis topic. The main research gaps in the area of elevated temperature creep of metallic materials has been highlighted and the objectives of the work have been identified. The methodology adopted for meeting the objectives is presented in detail in the subsequent chapter.

TH-1394_09610307

CHAPTER 3

RESEARCH METHODOLOGY

3.1 Introduction

This chapter presents the methodology adopted for meeting the objectives of the thesis work. The experimental procedures and techniques of analysis of the results are highlighted. This includes design and development of the creep testing set up, creep testing procedures, microstructural characterization of the test samples using optical microscopy (OM), scanning electron microscopy (SEM), field emission scanning electron microscopy (FESEM), transmission electron microscopy (TEM), energy dispersive X-ray (EDX) analysis and X-ray diffraction (XRD) technique. The creep analysis was carried out by constitutive and parametric models and the creep curve was predicted using artificial neural network modeling. Finally, the creep life of the material was determined by a modified Larson-Miller technique using the ANN predicted creep curve. The detailed procedures are explained in the subsequent subsections.

3.2 Experimental Procedures

3.2.1 Raw Material

The raw material used for the investigation was HP40Nb micro-alloyed austenitic stainless steel reformer tube having an inside diameter of 106 mm and 15 mm wall thickness, and supplied by Numaligrah Refineries Ltd., India. The reformer tube was manufactured by Doncasters Paralloy Limited, England by centrifugally casting. The reformer tube was used for hydrogen generation where the hottest part was exposed to 995 °C at a pressure of 2.5 MPa gas pressure. The tube was having an inner diameter of 106 mm and wall thickness of 15 mm. The chemical composition of the steel determined by Optical emission spectrometer (Make: Thermo Fisher Scientific Inc., Model: ARL 3460) indicted that the alloy composition was as per the ASTM A297 and that confirmed with the specification of the manufacturer.

3.2.2 Metallographic Sample Preparation

Specimens for microstructural investigation were prepared by standard metallographic specimen preparation technique. Transverse section of the reformer tube was sliced by wire cut electrical discharge machining (WEDM). The sliced specimen of

TH-1394_09610307

5 mm thickness was mounted in thermosetting resin using a hot mounting press (Make: Buehler, Model: Simplimet-2) at 20.7 MPa and 150 °C. The specimens were then polished in a grinder/polishing machine (Make: Buehler, Model: Ecomet-6). The grinding /polishing was carried out using SiC coated polishing discs with grit sizes 240, 320, 600, 1000 and 1500 in sequence. The lubricant used was water. Subsequently, cloth polishing was carried out using 0.5 µm sized alumina suspension dispersed in distilled water at a disc speed of 120 rpm. The polished specimens were then ultrasonically cleaned in acetone for 5 minutes, dried and preserved in a vacuum desiccator.

3.2.3 Optical Microscopy

The metallographically polished samples were etched using freshly prepared glyceregia solution (10 ml glycerol + 15 ml HCl + 5 ml HNO_3). After proper etching, the samples were washed in running water and dried. The etched specimens were observed under an upright optical microscope (Make: Carl Zeiss, Model: Axiotech) under monochoromatic light. The digital images were captured and analyzed by Axio Vision Rel.4.2 software.

The grain size of the specimen was determined by line intercept method. A grid of parallel lines of known length was superimposed on the micrograph taken at 10X magnification. The number of intercepts (intersections with grain boundaries) per unit length l_p was determined. The average grain size d is the mean intercept length $\bar{l}$which can be expressed as

$$d = \bar{l} = \frac{1}{l_p} \tag{3.1}$$

Grain size was measured at three different locations, such as near inner surface, near outer surface and at the middle of the wall thickness. At each location ten observations were taken and averaged to get average grain size.

3.2.4 Scanning Electron Microscopy

Unetched polished samples were gold coated using a plasma sputter coater and were observed under SEM (Make: LEO, Model: 1430 VP) and FESEM (Make: Zeiss, Model: Sigma). Images were captured by secondary electron (SE) detector and backscattered electron detector (BSD).Majority of the SEM imaging were carried out with accelerating voltages in the range of 10-20 kV and working distance of 15 mm.

TH-1394_09610307

The composition of various phases present in the matrix were analyzed using energy dispersive X-ray spectroscope EDX (Make: Oxford, Model: INCA X-Sight) attached with electron microscopes. Quantitative analysis of constituent phases was carried out using high purity cobalt as the reference standard. Qualitative distribution of various elements in the specimen matrix over specific area was obtained by X-ray elemental mapping technique.

3.2.5 X-ray Diffraction

The crystal structure of the steel and various phases present were identified by X-ray diffraction (XRD) technique. Samples of size10 mm × 10 mm × 3 mm was sectioned by WEDM and cleaned with acetone. XRD analysis was carried out (a) in as-received condition and (ii) after a heat treatment. For the case of (ii), the sample was heated in air at 1000 °C for 72 hour in a muffle furnace followed by quenching in water at room temperature. Prior to carrying out the XRD analysis, the samples were polished using standard metallographic technique. Since the quantity of fine precipitates present in the alloy was very less, one set of samples were immersed in glyceregia solution to dissolve away iron. By this technique, only the iron was dissolved in the solution. By this all the fine second phase particles present in the alloy matrix formed a fine suspension in the glyceregia solution. These precipitate / particles were filtered and cleaned with isopropyl alcohol and dried for XRD analysis.

X-ray diffraction was carried out using Cu Kα radiation (λ = 1.54 Å) at a tube rating of 40 kV and 40mA in a commercial powder X-ray diffractometer (Make: Rigaku, Model: RINT 2500TRAX-III). XRD pattern was obtained for 2θ in the range 30-80°. The reflected X-rays were collected by a scintillation X-ray detector at an interval of 0.03° and a step-time of 0.3 second. The possible phases present in the powder and solid samples were identified by comparing the peak position and intensity with JCPDS database.

3.2.6 Transmission Electron Microscopy

The crystal structure of the samples were investigated using a 200 kV TEM (Make: JEOL, Model: JEM 2100TEM). The powder particles obtained for carrying out the XRD analysis was used for the TEM study. The powder samples were taken on a

TH-1394_09610307

400 mesh carbon coated copper grid and then the copper grid was placed in the sample holder of the TEM. Selective area diffraction (SAD) patterns were obtained which were then indexed to identify the structure of the particles. Inter-planar spacing of the crystal was evaluated from the HRTEM images.

3.3 Mechanical Property Test

Details regarding evaluation of the tensile properties at room and elevated temperatures and creep testing are discussed in the subsequent sub-sections.

3.3.1 Tensile Test

Flat tensile specimens having gauge section of 25 mm length and cross-sectional area of 6.5 × 3 mm^2 were machined from the reformer tube by WEDM. The specimens were prepared such that the axis of each specimen was parallel to the longitudinal axis of the reformer tube. The geometry of the flat tensile specimen is shown in Figure 3.1.

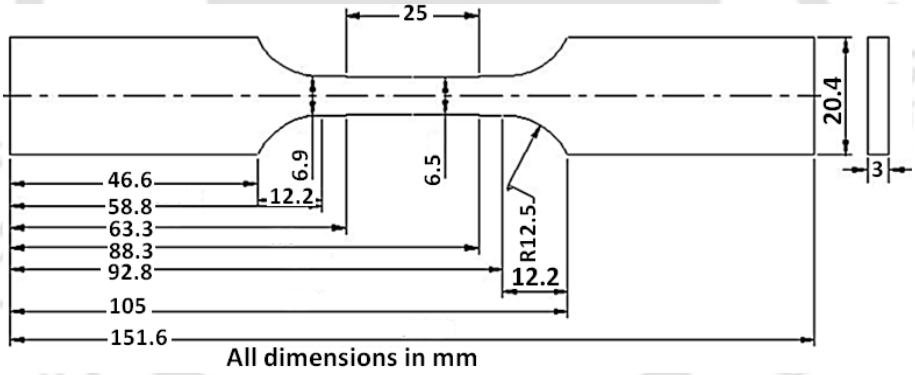

Figure 3.1. Schematic of the flat tensile test sample.

Tensile tests were carried out using a 100 kN capacity servo hydraulic controlled universal testing machine (Make: INSTRON, Model: 8801). A split-type two-zone resistance heated split type high temperature furnace (Make: INSTRON SFL, Model: SC 1706) attached with the machine was used for the elevated temperature tests. The specimen was heated to the test temperature and the test temperature was controlled with an accuracy of ± 1 ˚C using the PID controller attached with the furnace set up. To ensure uniform temperature across the specimen gauge section, the sample was soaked for 10 minutes before the tensile load was applied. Tensile loading of the samples were carried with a constant actuator speed of 0.05mm/min till failure. A high temperature extensometer (Make: Epsilon Technology Corporation, Model: 3548HI-025M-010-HT)

TH-1394_09610307

attached to the specimen was used to measure the displacement across the 25 mm gauge length. During the test, the load vs. extension data were acquired and recorded by the UTM (Merlin) software available with the UTM. Tensile testing was carried out at room temperature (27 °C), 200 °C, 400 °C, 600 °C, 800 °C, 1000 °C and 1200 °C.

From the load vs. extension data, the stress-strain curves were plotted. The Young's modulus *E*, ultimate tensile strength (UTS) and fracture strain ε_f were determined for the steel. 0.2 % off set strength was taken as the yield strength (YS) of the material. The true stress-true strain (σ -ε) plot obtained, was assumed to follow the Holloman-Ludwig equation which is of the of the form $\sigma = K\,\varepsilon^n$ [229] where, σ is true stress, *K* the strength coefficient, ε the true plastic strain and *n* is the strain-hardening exponent. The strain hardening exponent, *n* for various test temperatures were determined using the expression [230]:

$$n = \left[\frac{\partial(\log\sigma)}{\partial(\log\varepsilon)}\right]_{T,\dot{\varepsilon}} \tag{3.2}$$

The tensile fracture surfaces were observed under SEM to study the failure mode during the tensile tests. The specimen were also sliced longitudinally followed by metallographic polishing. The polished surfaces were also investigated under the microscope to investigate defect nucleation and growth during the tensile tests.

3.3.2 Creep Test

The reformer tube used for the present investigation was having outside diameter of 136 mm with a wall thickness of 15 mm which can be considered as a thin cylinder. Since the tube was designed for an internal gas pressure of 2.75 MPa, the hoop stress and axial stress in the tube during service corresponded to 4.86 MPa and 2.43 MPa, respectively. The creep tests were carried out on flat specimen machined as per the orientation and geometry illustrated in Figure 3.2.

It was decided to carry out longitudinal creep tests. A creep testing set up was designed and developed for carrying out the creep test under constant true stress conditions. The details regarding the design and development of the creep test set up are given in the subsequent sub-section.

TH-1394_09610307

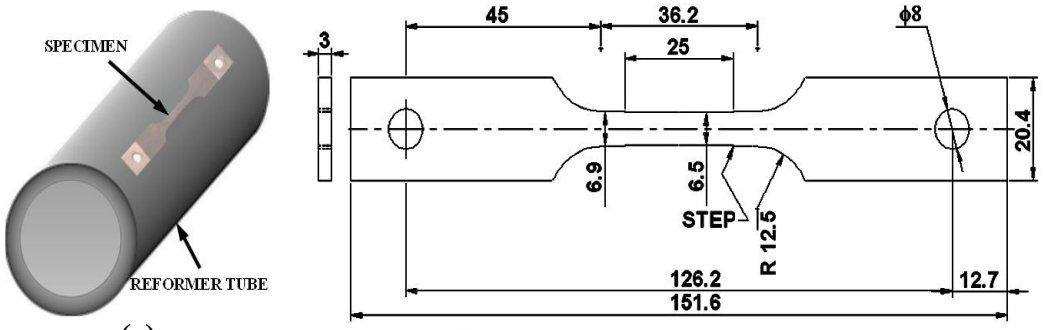

(a) (b)

Figure 3.2. (a) Flat creep specimen machined from reformer tube and (b) schematic of the flat creep test specimen (all dimensions are in mm).

3.3.2.1 Design and Development of Constant Stress Creep Test Set-up

The following assumptions were made for the creep set up design.

a) During creep deformation, the volume of the gauge length will remains constant.

b) Transverse strains assumed negligible.

c) The creep set up to be designed for a gauge length extension of 15 mm corresponding to a true strain of 0.4.

During the longitudinal creep strain, since the cross section continuously decreases for maintaining the constant volume relationship, the area of the gauge section continuously decreases with gauge length extension. To maintain a constant true stress condition, it is required that the external load on the specimen will have to continuously decrease with increase in gauge length extension. The load vs. gauge length extension for a constant stress σ at any instant can be obtained as follows:

Let, L_{gauge}, W_0 and t_0 be the initial length, initial width and initial thickness of the gauge section of the sample, respectively. The instantaneous load F_i on the specimen,

$$F_i = \sigma \times A_i \tag{3.3}$$

From the constant volume relationship, the instantaneous area of the gauge section A_i is related to change in gauge length Δ and initial area A_o by the relationship:

$$A_i = \frac{L_{gauge} \times A_o}{L_{gauge} + \Delta} \tag{3.4}$$

Combining Eq. (3.3) and Eq. (3.4), we get

$$F_i = \sigma \times A_i = \sigma \times \frac{L_{gauge} \times A_o}{L_{gauge} + \Delta} \tag{3.5}$$

TH-1394_09610307

Figure 3.3 shows the load vs. elongation plot for constant true stresses of 120 MPa, 80 MPa, 68 MPa and 47MPa, for a gauge length of 25 mm. The figure indicates that load vs. elongation plots are non-linear. Close observation of the curves indicates that for constant stresses of 47 MPa, 68 MPa and 80 MPa, the curves can be almost approximated as straight lines with different slopes.

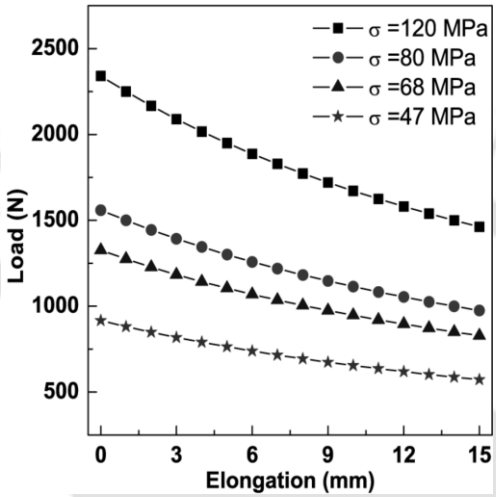

Figure 3.3. Load vs. elongation plots required for constant stresses.

Figure 3.4 shows the curves superimposed with the fitted strain lines. During the specimen gauge length extension of up to 15 mm, the maximum deviations from the required values were estimated to be within ± 5 %. Since an error of ± 5 % deviation in load during the creep test can be acceptable for these experiments, it was decided to conduct the creep tests assuming a linear relationship for the between the load and the gauge length extension. For a constant true stress testing with 120 MPa stress, the load deviation from the required values were found to be higher when approximated with a straight line fit.

Figure 3.5 shows the experimental set up designed and fabricated for carrying out the longitudinal creep tests. The set up consists of a load frame, impedance heater set up, infrared (IR) pyrometer, high definition video camera, data acquisition system for measurement and recording of specimen temperature and load acting on the specimen. The detailed descriptions of each are as follows:

a) Load frame: The load frame consists of a steel frame with a top plate and a bottom plate connected rigidly using four vertical cylindrical columns. A power screw

TH-1394_09610307

attached with a nut at the top end passes freely through the top plate. The bottom end of the screw is fixed to a mild steel disc as shown in the figure. Rotation of the nut

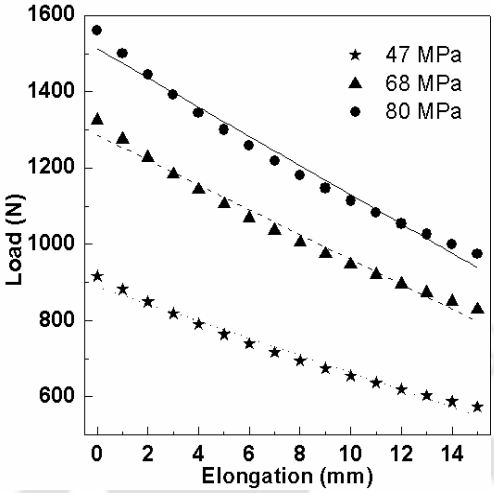

Figure 3.4. Load vs. elongation plots required for constant stresses with straight line fit.

facilitates axial movement of the power strew and the disc. The rotation of the disc is constrained by means of 4 guide rods fitted to the top plate and passing through 4 brass bushes inserted in to the disc. A tension spring is connected to the steel disc and the upper extension rod by means of pin joints. The specimen is held between the upper extension rod and the lower extension by means of pins. Lower end of the lower extension rod is attached to an S-type load cell which is fixed to the bottom plate of the load frame through extension rods. Rotation of the nut results in axial movement of the power screw thereby loading the spring to the required value and elastic energy is stored in the spring. During the tensile extension of the specimen, a part of the stored energy is released thereby reducing the external load on the spring. Single springs with spring constants of 22.4 N/mm, 33.7 N/mm and 42 N/mm were used for carrying out creep tests at constant stresses of 47 MPa, 68 MPa and 80 MPa respectively. The detailed calculations of the spring constants are given in Appendix-IV. Since, the load vs. extension plot for the creep test with constant stress of 120 MPa was highly non-linear, use of a single spring results in higher deviation of load from the required value. Hence, the set up was modified using inclined tension springs with spring constant of 59.39 N/mm to achieve the desired nonlinearity. The design details for regarding this modification are given in Appendix -V.

TH-1394_09610307

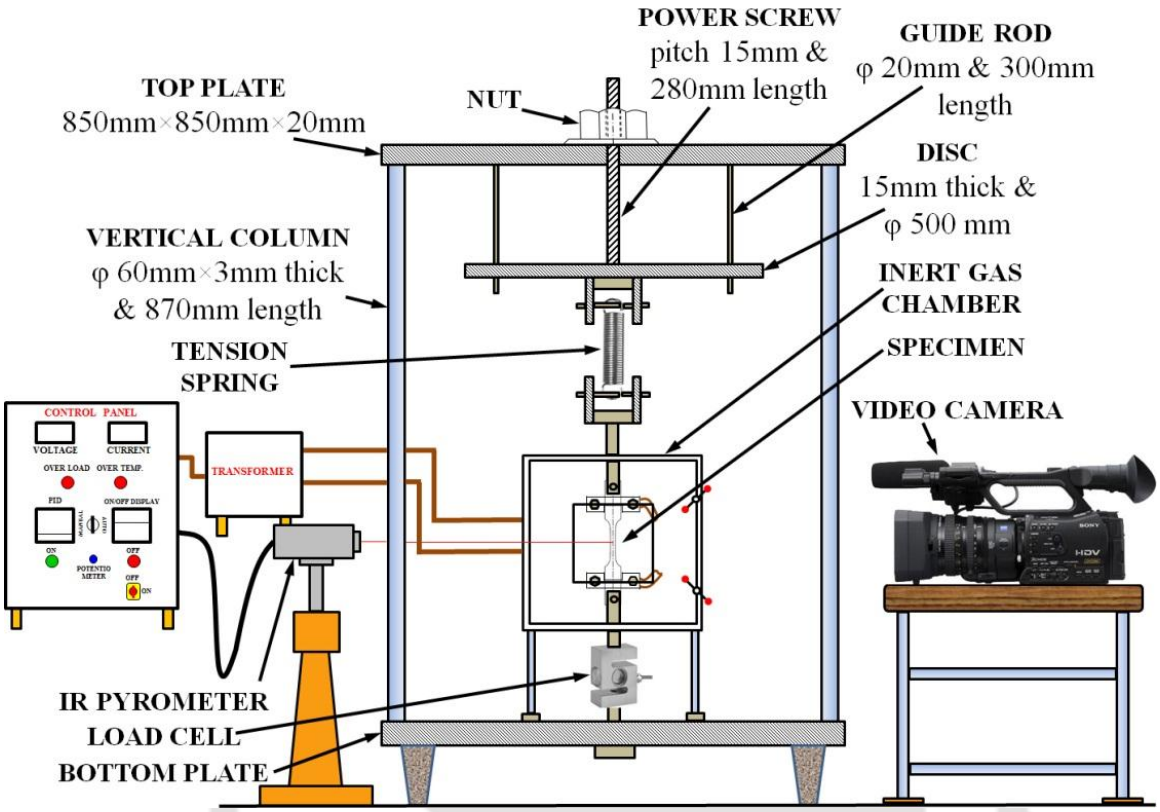

Figure 3.5. Schematic diagram of low stress creep apparatus.

b) Impendence heater system: Heating and maintaining the specimen at the required temperature was carried out using an impedance heater system. The schematic diagram of the heater assembly is shown in Figure 3.6. The creep specimen was held in the testing setup by means of extension rods (Part-J). The test specimen was heated to the required temperature by the impedance heater (Part A). Specimen temperature was measured using IR pyrometer (Part H) and the specimen temperature was precisely controlled by manual control of the input current to the transformer by means of a highly sensitive potentiometer. The specimen was enclosed in a stainless steel (SS) chamber having quartz windows for observation and capturing digital video images of the specimen during the experiments. Inert gas was maintained in the chamber by purging with high purity (99.9% pure) argon gas.

c) Infra-red pyrometer: The temperature of the specimen was continuously monitored by an IR pyrometer (Make: Accurate Sensors Technologies Ltd., Model: AST 250).

d) Video camera: A high definition video camera (Make: Sony, Model: HVR-Z7P) was used for the digital video capturing of the specimen images during the creep tests. Digital video frames were used for the determination of the gauge length

TH-1394_09610307

extension of the specimen during the creep deformation by image analysis technique.

e) Data acquisition system: The external load on the specimen was measured using an S-type load cell (Make: Precision Electronic Instruments Co., Model: LC34810 500R). Specification of the load cell is shown in Appendix-VI. The load on the specimen was monitored by a digital load indicator which was connected to a data acquisition (DAQ) system (Make: VPL Infotech & Consultants, Model: I 7018). The DAQ was interfaced to the computer system through RS 232 cable. The load on the specimen was continuously acquired and stored by the DASYLab®8.0 data acquisition software. Load acquisition rate was the average of every 5 seconds interval.

The extension rods connected to the creep specimen were INCONEL 718. Figure 3.7 shows the arrangement of constant stress creep testing apparatus with impedance heater, pyrometer, load indicator, video camera and inert gas chamber.

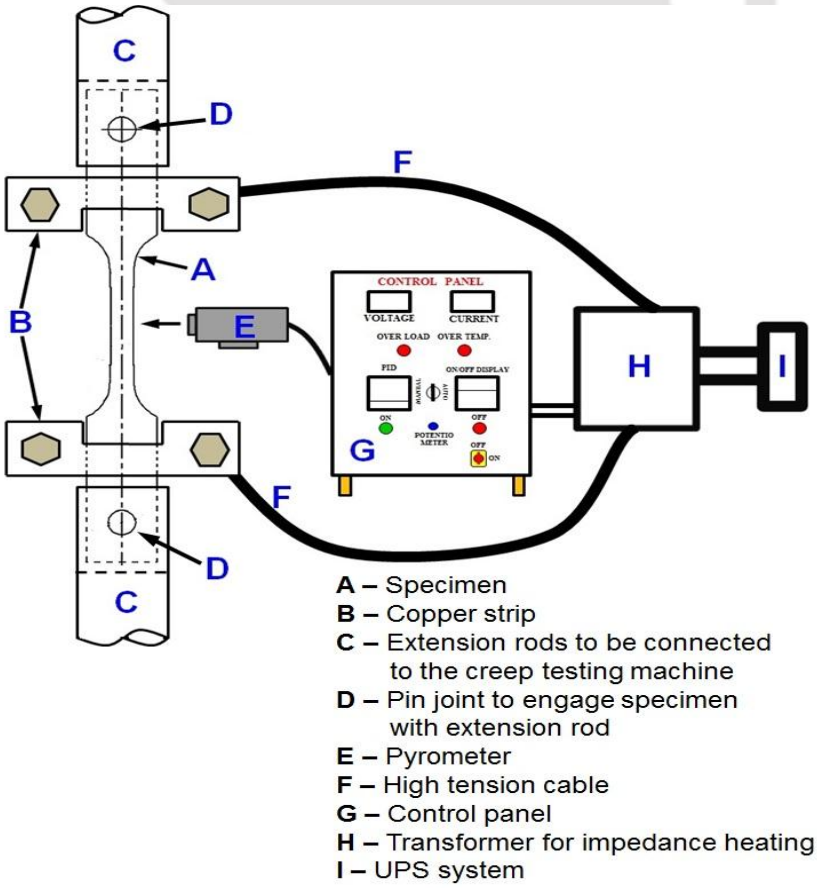

Figure 3.6. Schematic of the impedance heater assembly.

TH-1394_09610307

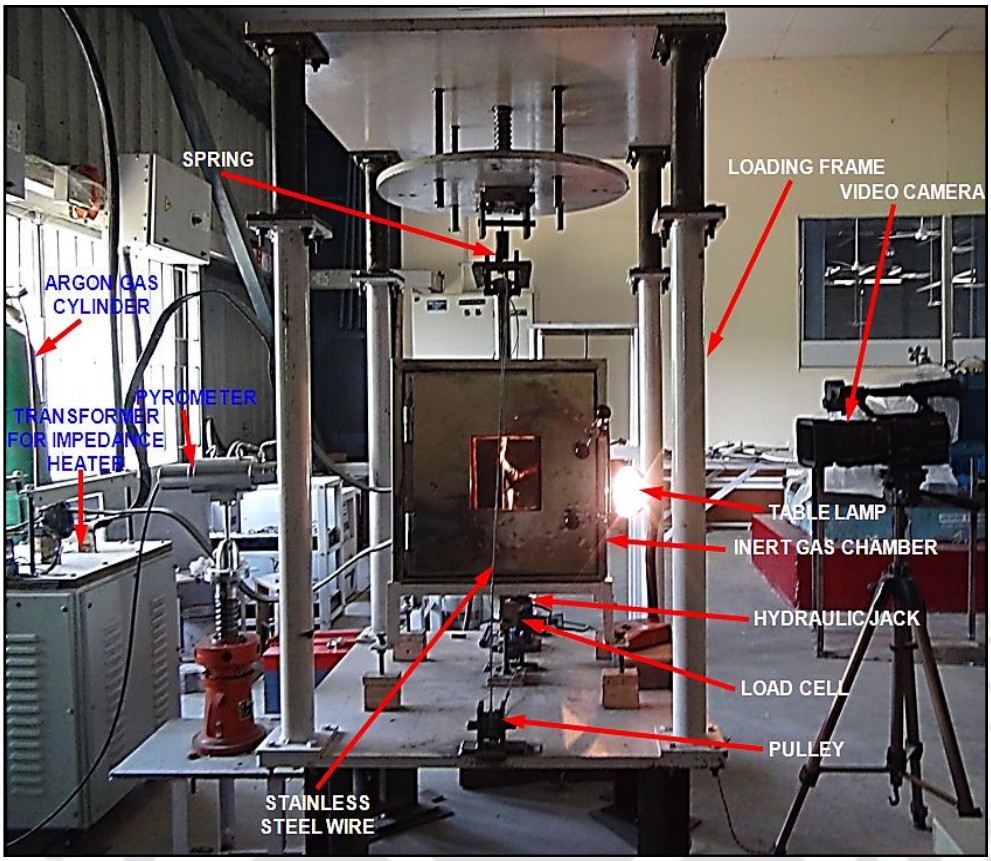

Figure 3.7. Arrangement of low stress creep testing apparatus with impedance heater, pyrometer, load indicator, video camera and inert gas chamber.

The load cell, pyrometer, and strain measurements by video imaging were calibrated. The load vs. gauge length extension for each constant stress experiment was also checked and was found satisfactory. Details regarding the calibration are discussed in the subsequent sub-sections.

3.3.2.2 Calibration of Load Cell

The S-type load cell (Figure 3.8(a)) used for the measurement of the creep tests was calibrated using the UTM mentioned in section 3.3.1. The S-type load cell along with the digital display unit and DAQ system was fixed to the grips of the UTM through the extension rods. The load cell was loaded monotonically in the UTM at a machine cross head speed of 0.5 mm/minute. The load vs. time data from the UTM and the DAQ system of the S-type load cell were continuously recorded and compared. Figure 3.8(b) shows the plot of the load recorded by the UTM vs. the S-type load cell DAQ system. The results indicated that the load cell value obtained from the DAQ system was as per

TH-1394_09610307

the calibration chart provided by the supplier and was deviating from the UTM load cell values by only +1.32 %.

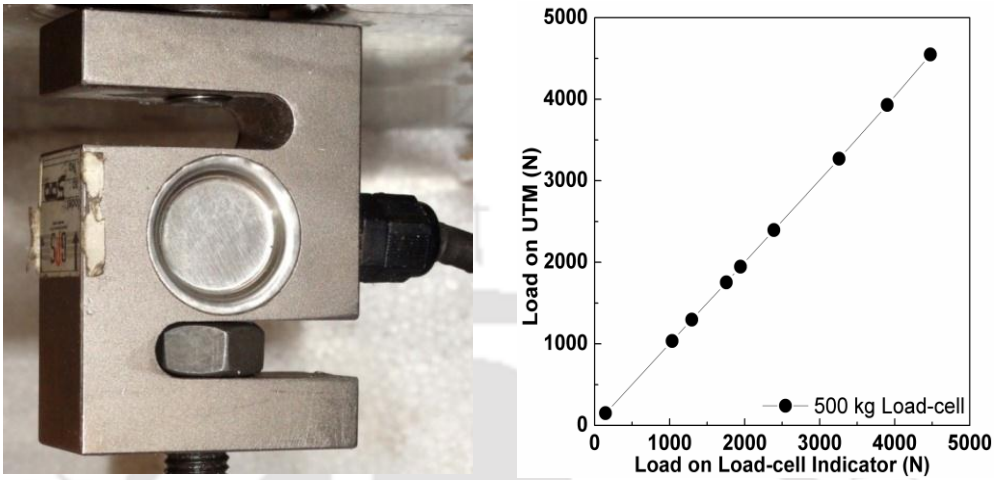

(a) (b)

Figure 3.8. (a) S-type load cell and (b) variation of load on load cell indicator vs. load on UTM machine for 500kg load cell.

3.3.2.3 Calibration of Strain Measurement System

It was expected that the gauge length extension during the creep tests would be around 15 mm. The maximum travel length for the commercially available high temperature extensometers are of the order ± 5 mm. Hence, it was decided to determine the creep strains by image analysis of the digital frames obtained by video capturing of the gauge length during the experiment. A high speed digital HD video camera (Make: Sony, Model: HVR-Z7P) was used for capturing the specimen gauge length extension during the creep tests. The accuracy of the strain measurement technique was required to be ascertained. For this tensile tests were carried out on 3 mm thick flat tensile specimen made out of aluminium. Tensile loading was carried out in the same UTM mentioned earlier. Two parallel lines corresponding to 25 mm gauge length were marked on the flat surface of the tensile specimen for the measurement of sample extension. For comparison purpose, a 25 mm gauge extensometer (Make: INSTRON, Model: 2620-601) was attached on the opposite face of the specimen at points corresponding to the two parallel lines. The specimen was loaded in tension with the actuator speed of 0.5 mm/minute. The specimen extension vs. time plot from the extensometer was recorded during the tensile loading. Simultaneously, the digital video recording of the two parallel lines were also carried out. From the video frames, the

TH-1394_09610307

distances between the two parallel lines were determined by image processing. The change in length between the parallel lines gave the specimen extension across 25 mm distance. The time dependent specimen extension was plotted. From the above data, the specimen extension values obtained by the image analysis were plotted against the extensometer reading. Figure 3.9 shows plot of specimen extension by image analysis vs. extensometer reading. The plot indicates a straight line fit with a slope of 1 with coefficient of determination R^2 of 0.998, indicating a very high confidence level in the strain measurement by the video recording followed by image analysis technique.

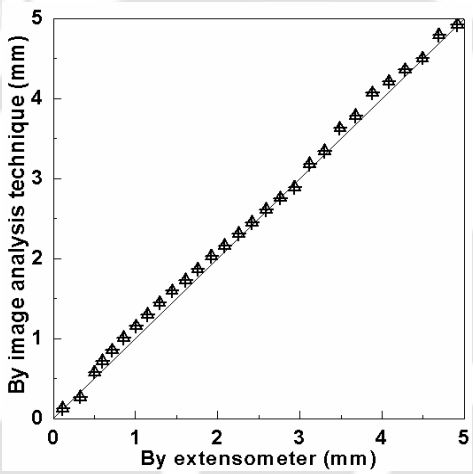

Figure 3.9. Plot of specimen extension by image analysis vs. extensometer reading.

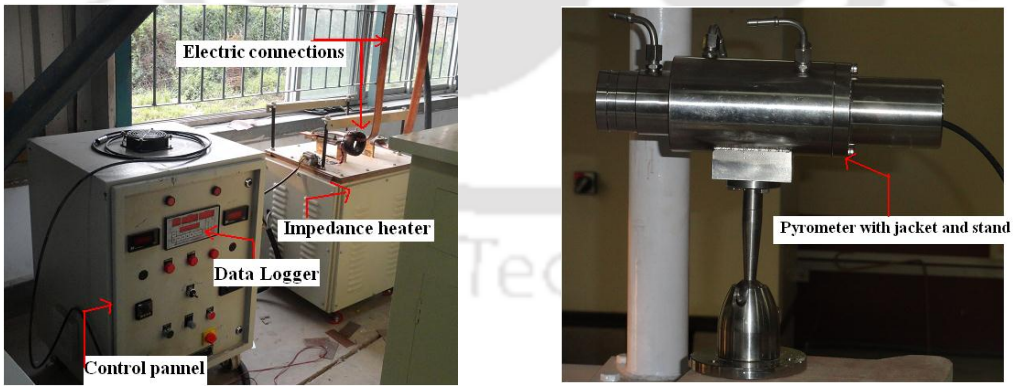

(a) (b)

Figure 3.10. Photographs of (a) impedance heating system and (b) non-contact IR pyrometer.

3.3.2.4 Creep Testing Procedure

The tensile creep specimen was attached to the load frame as shown in Figure 3.11. The particular spring for achieving the required load vs. displacement plot for the

particular constant true stress test was used for each stress level. Sample was connected electrically to the impedance heater and heated to the required temperature within 30 seconds and maintained constant within ± 3 °C by manually controlling the input current of the heating system. The required ampere for each temperature was pre-determined before the start of the actual experiment. Temperature of the specimen was measured continuously by the IR Pyrometer. The video recording was also carried out continuously till failure of the specimen.

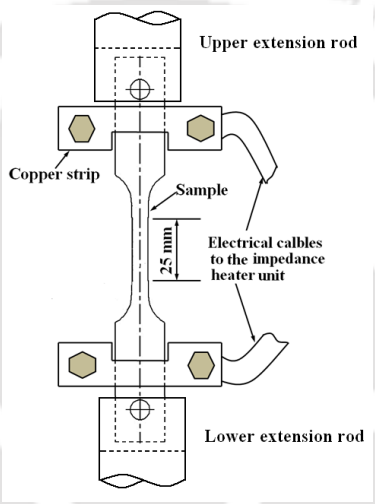

Figure 3.11. Schematic diagram of the specimen attachment.

Gauge length elongation was measured by image analysis technique. From the digital video recording picture frames at regular time interval of testing was separated by image capture software (Make: Video LAN, Version: VLC 2.1). From each such frame, elongation of gauge length was measured between the parallel slots provided in specimen by image analysis technique. The elongation was determined in terms of pixel by picture manager (Make: Microsoft Corporation, Version: Picture Manager 4). Finally, pixel value was converted to engineering unit by comparing with image taken prior to loading and engineering strain and true strain was determined.

Initially, the required load vs. displacement plot for each constant stress test was verified by carrying out a trial experiment using a mild steel sample as dummy. Only after achieving the full confidence in the experiment, the actual experiment on the HP40Nb steel was conducted.

TH-1394_09610307

3.3.3 Creep Test Matrix

In the present methodology, it was decided to carry out accelerated creep experiments at high stresses and temperatures and from these date the creep life of the material would be determined by extrapolation techniques. The experimental matrix for the present investigation is shown in Table 3.1. Due to the long duration of tests, it was decided to carry out only one experiment under each test condition.

Fracture surface and microstructural observation of the samples were carried out after creep tests in order to identify fracture behavior and deformation mechanism of the material.

Table 3.1. Creep-rupture test experimental matrix ("√" indicates the experiments carried out)

Temperature	Constant true stress (MPa)			
(˚C)	120	80	68	47
650	√	----	----	----
700	√	----	----	----
750	√	√	√	----
800	√	√	√	√
825	----	----	√	----
850	√	√	----	√
900	----	√	√	√
925	----	√	----	----
950	----	√	√	√
1000	----	----	----	√
1050	----	----	----	√

3.4. Analysis of Creep Test Data

The data obtained from the creep tests were used for

1. development of constitutive equation for steady state creep rate
2. verifying the Monkman-Grant relationships
3. parametric study for obtaining the creep life of the material
4. modeling the creep curve for various combinations of stress and temperature by artificial neural network (ANN) technique.

The details are shown in the subsequent sub-sections.

3.4.1 Constitutive Modeling of Creep Behaviour

The creep stress exponent n_c and apparent activation energy for creep Q_{app} of power law creep (Eq. 2.2) for steady state creep rate were determined from the

TH-1394_09610307

experimental creep data. The value of creep stress exponent n_c was determined from the slope of double logarithmic straight line plot of minimum creep rate vs. applied stress for constant temperatures. The existence of creep threshold stress σ_{th} is a stress below which creep cannot be measured at a given temperature, was verified graphically. Threshold stress σ_{th} at constant temperatures were determined from a bilinear plot of minimum creep rate to the $1/n_c$ power $(\dot{\varepsilon}_s)^{1/n_c}$ vs. applied stress σ. The value of σ_{th} for a particular temperature was obtained by extrapolating linear fit of the creep data to the stress axis where the value of $(\dot{\varepsilon}_s)^{1/n_c}$ is equal to zero. The apparent activation energy for creep Q_{app} at constant stress was determined graphically by plotting $\ln(\dot{\varepsilon}_s)$ vs. the inverse of the absolute temperature. The slope of the plot of constant stress lines is equal to - Q_{app}/R. The value of n_c and Q_{app} were used to identify creep deformation mechanism(s) by comparing with microstructure and creep fractography. The material constants A_1, A_2, A_3, n_c, β and α of Eq. 2.2, Eq. 2.3 and Eq. 2.4 were determined by the method of least squares. Values of minimum creep rate were calculated using these constants for combination of stress and temperature and compared with experimental $\dot{\varepsilon}_s$ values.

3.4.2 Monkman-Grant Relationships

Analysis of the creep data by Monkman-Grant relationship was carried out from the creep curve data. The notations used for the data analysis are shown schematically in Figure 3.12. The minimum value of the slope of the creep curve was used as the minimum strain rate $\dot{\varepsilon}_s$ and that corresponded to the slope of the secondary creep region. The tangent to the creep curve at the point corresponding to the minimum creep rate was extended to intersect the strain axis at t = 0 and $t = t_r$ at points A and B respectively. The primary creep strain ε_1 and the secondary creep strain ε_2 corresponded to distance OA and BD-OA respectively. Since, the total rupture strain was ε_f, the tertiary strain ε_3 was determined as ε_f–(ε_1+ε_2). The time t_{os} was assumed to be the time required for the onset of secondary creep, whereas time $t_t = t_r - t_{ot}$ was taken as the creep time during the tertiary creep deformation, where t_r is the time to rupture and t_{ot} is the time at the onset of tertiary creep. The Monkman-Grant ductility (MGD) was taken as the secondary creep strain ε_2 which was the product of minimum strain rate and rupture time $(\dot{\varepsilon}_s . t_r)$. The time to reach Monkman-Grant ductility t_{MGD} was the time taken to

TH-1394_09610307

reach the tertiary strain. From Eq. 2.10, minimum strain rate $\dot{\varepsilon}_s$ and strain to failure ε_f, were expressed in terms of creep damage tolerance factor λ.

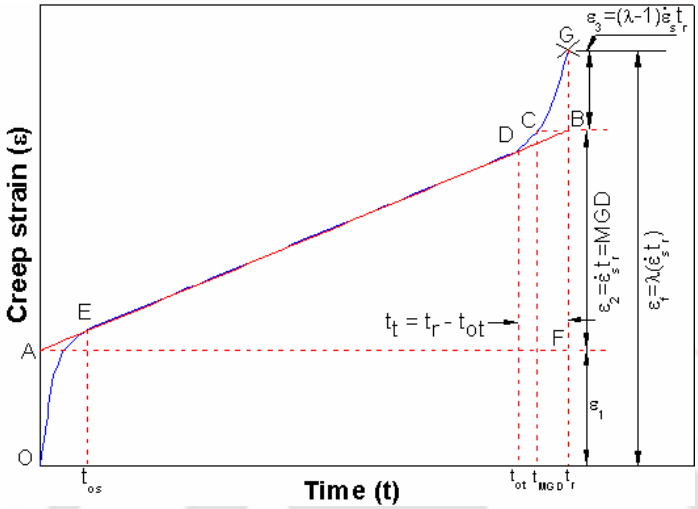

Figure 3.12. Typical creep curve showing different material parameters used for explaining creep behavior of the steel.

3.4.3 Artificial Neural Network Modeling

The creep data obtained from the experiments were used for the artificial neural network. The ANN modeling was carried out by the multiple layer precipitation (MLP) feed forward back propagation network. Figure 3.13 shows a typical Neural Interpretation Diagram (NID) for feed-forward back propagation hierarchical artificial neural network.

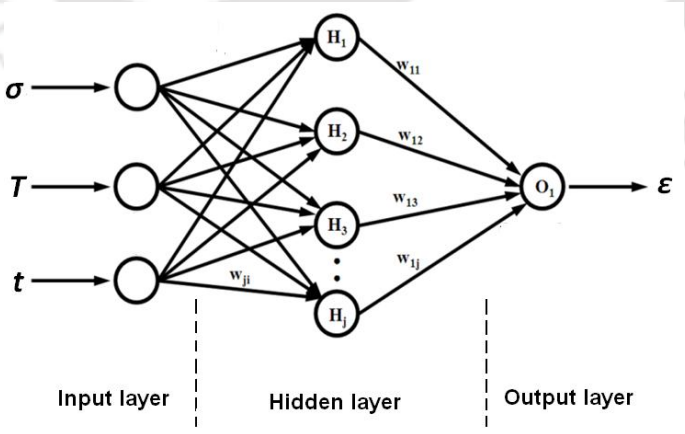

Figure 3.13. The neural network architecture.

During the creep deformation, the creep strain ε is dependent on three independent parameters σ, T and t. Hence, the input layer in the present network consisted of three neurons representing these parameters. The output layer consisted of

TH-1394_09610307

one neuron representing the creep strain. Training of the neural network was done in MATLAB® (Make: Math Works Inc., Version: R2010a) software using *trainlm* function. By the *trainlm* training function the weights and bias values in a back propagation algorithm is updated as per the Levenberg-Marquardt optimization algorithm, which is a highly efficient method for solving non-linear optimization problems.

22 creep experiments were carried out till failure under different combinations of stress and temperatures as shown in Table 3.1. From these 22 experiments, a total of 1262 input–output data sets were obtained for the ANN modeling. Out of these, it was decided to use 732 as training data, 376 as testing data and 154 as validation data. All the values of stress, temperature and time were mapped to lie between 0.1 and 0.9.

To decide the best neural network architecture and processing function, a number of numerical experiments with single hidden layer neural networks and *tansig* and *logsig* processing functions were carried out by varying the number of neurons in the hidden layer. The *tansig* and *purelin* processing functions were found to be most suitable for the input to hidden layer and hidden to output layer respectively. The *tansig* function gives the output in the manner

$$\text{Output of the neuron} = \frac{e^{CI} - e^{-CI}}{e^{CI} + e^{-CI}} \tag{3.6}$$

where I is the net input to the neuron and C is a constant. The *purelin* function gives the output in the manner

$$\text{Output of the neuron} = CI \tag{3.7}$$

The root mean square functional error used as a measure of performance as given by [231]

$$RMS_{err}^{f} = \sqrt{\frac{\sum (E_i - P_i)^2}{N{E_i}^2}} \tag{3.8}$$

where E_i is the experimental value, P_i is the predicted value and N is number of data set. Both training and testing error were calculated separately. Effective error for training and testing data is given by

$$\text{Effective error} = \text{maximum of } [RMS_{err}^{f} \text{ of training data, } RMS_{err}^{f} \text{ of testing data}] \tag{3.9}$$

TH-1394_09610307

A maximum deviation in error of ± 15 % was considered as a second error norm during the training and testing.

The training error goal for the creep strain was varied between 10^{-2} and 10^{-5}. An error goal of 10^{-4} was found to give the best results. After a number of trials with various initial weights and biases, one hidden layer neural network with 15 neurons in the hidden layer was frozen with an error of 33.6 % in predicting the creep strain for the entire 732 input-output data sets. The trained network model showed an error of 31.9 % while testing with the 376 data sets. Table 3.2 shows the details of the frozen ANN architecture.

Table 3.2. ANN architecture used for the simulation.

Number of input layer units	3
Number of hidden layers	1
Number of hidden layer units	15
Number of output layer units	1
Total data set used	1262
Training data set	732
Testing data set	376
Validation data set	154
Activation function	*tansig* and *purelin*
Performance goal fixed	10^{-4}
Epochs required to attain goal	7373

The predictability of the trained ANN model was verified via employing standard statistical parameters such as correlation coefficient (R_{cc}), average absolute relative error (AARE) and average root mean square (RMS) error. They are expressed as:

$$R_{cc} = \frac{\sum_{i=1}^{N}(E_i - \bar{E})(P_i - \bar{P})}{\sqrt{\sum_{i=1}^{N}(E_i - \bar{E})^2 \sum_{i=1}^{N}(P_i - \bar{P})^2}} \tag{3.10}$$

$$\text{AARE (\%)} = \frac{1}{N}\sum_{i=1}^{N}\left|\frac{E_i - P_i}{E_i}\right| \times 100 \tag{3.11}$$

$$\text{RMS error} = \sqrt{\frac{1}{N}\sum_{i=1}^{N}(E_i - P_i)^2} \tag{3.12}$$

where E_i and P_i are the experimental and predicted value, respectively, $\bar{E}$ and $\bar{P}$ are the average values of E_i and P_i, respectively and N is the total number of data used in the investigation.

TH-1394_09610307

The relative importance of each input variable on the output variable was determined based on the ANN weight matrix and Garson's algorithm [232]. Garson (1991) proposed a method of partitioning the neural network weights to determine the sensitivity of each input variable in the neural network and is expressed as [233]:

$$I_j = \frac{\sum_{m=1}^{m=Nh}\left(\left(\left|w_{jm}^{ih}\right| \div \sum_{k=1}^{Ni}\left|w_{km}^{ih}\right|\right) \times \left|w_{mn}^{ho}\right|\right)}{\sum_{k=1}^{k=Ni}\left\{\sum_{m=1}^{m=Nh}\left(\left(\left|w_{jm}^{ih}\right| \div \sum_{k=1}^{Ni}\left|w_{km}^{ih}\right|\right) \times \left|w_{mn}^{ho}\right|\right)\right\}} \quad (3.13)$$

where I_j is the relative importance of the j^{th} input variable on the output variable, N_i & N_h are the number of input and hidden neurons, respectively, w are connection weights, the subscripts 'i', 'h' and 'o' refer to input, hidden and output layers, respectively and subscripts 'k', 'm' and 'n' refer to input, hidden and output neurons, respectively.

Once the ANN architecture was frozen, the fitted neural network was tested with the 154 validation input-output data sets. This validation data set was not used earlier for the training or testing purpose. The neural network was also checked by simulating the creep curves under the 22 experimental conditions mentioned in Table 3.1.

The ANN model was also used to generate further creep curves under various combinations of stress, temperature and was used for estimation of the creep life by Manson-Haferd parameter, Orr-Sherby-Dorn parameter and Larson-Miller parameter.

3.4.4 Parametric Study for obtaining the Creep Life of the Material

3.4.4.1 Manson-Haferd Parameter

The Manson-Haferd constants T_a and $\log_{10}(t_a)$ of Eq. 2.14 were determined graphically from the plot of $\log_{10}(t_r)$ vs. temperature T at constant stresses. The intersection point of extrapolated iso-stress lines corresponded to the value of T_a and $\log_{10}(t_a)$. The arithmetic mean of the converged points of paired iso-stress lines was determined and used to calculate Manson-Haferd parameter. The master curve for Manson-Haferd model was developed based on the relationship shown in Eq. 2.14. Applied stress vs. Manson-Haferd parameter was plotted. The master curve was used to predict the remaining creep life of the steel.

3.4.4.2 Orr-Sherby-Dorn Parameter

The applied stress σ vs. $P_{O\text{-}S\text{-}D}$ master curve was obtained using Eq. 2.16. Orr-Sherby-Dorn constant Q_c was determined by trial and error where the coefficient of

TH-1394_09610307

determination R^2 for the linear fit of the master plot was maximum. The master curve for Orr-Sherby-Dorn parametric technique was developed based on the relationship shown in Eq. 2.16. The master curve was used to predict the remaining creep life of the steel.

3.4.4.3 Larson-Miller Parameter

The Larson-Miller constant $C_{L\text{-}M}$ of Eq. 2.13 was determined graphically from the iso-stress plot of $\log_{10}(t_r)$ vs. inverse of temperature ($1/T$). By extrapolating linear fit of the iso-stress creep data to the $\log_{10}(t_r)$ axis where the value of $1/T$ was zero, the constant value of $C_{L\text{-}M}$ was determined. The constant value of $C_{L\text{-}M}$ was also considered as 20 to compare creep life of the investigated steel. The master curves for Larson-Miller parametric technique were developed based on the relationship shown in Eq. 2.13. Applied stress σ vs. Larson-Miller parameter $P_{L\text{-}M}$ was plotted. The master curves were used to predict the remaining creep life of the steel. In general, creep failure in engineering materials occurs at around 15 % elongation. Creep life of the steel considering the time to 0.15 creep strain (16.2 % gauge length elongation) were compared between different parametric techniques.

TH-1394_09610307

RESULTS & DISCUSSION

4.1 Introduction

The results of the experiment outlined in chapter 3 are presented in this chapter along with the discussions. The microstructure of as received micro-alloyed HP40Nb steel is discussed. The results of the tensile tests at various temperatures, the tensile fracture characteristics and results of the accelerated creep tests are discussed. Creep behaviour and life assessment of the steel is carried out supported by constitutive modeling and different parametric models. The results of ANN modeling for the prediction of creep curves are also presented and discussed.

4.2 Composition and Microstructure

4.2.1 Chemical composition of the Steel

Chemical composition of as received material is shown in Table 4.1 along with the manufacturer's specification. The results indicate that the material is conforming to the HP40Nb micro-alloyed austenitic steel.

Table 4.1. Chemical composition in weight percentage of the alloy given in ASTM A297 standard and by manufacturer.

	C	Mn	Si	P	S	Cr	Ni	Mo	Nb	Ti
Manufacturer	0.4	1	1.5	-	-	25	35	-	1.2	-
Spectrometer	0.41	-	1.25	-	-	23.56	34.95	0.037	0.81	0.037

4.2.2 Microstructure of the Alloy

Figure 4.1(a)-(f) shows the optical microstructure of the reformer tube taken at three different magnifications. Low magnification micrographs shown in Figure 4.1(a) and (b) reveal dendritic structure. A network of second phase particles is observed at the inter-dendritic regions. Microstructure of the sample near the inner wall surface reveals equiaxed grains with a continuous network of carbides at grain boundary regions (Figure 4.1(c)) whereas the carbides at the grain boundaries were in discontinuous form at regions near to the outer wall of the tube (Figure 4.1(d)). High magnification observation reveals two types of second phase particles at the grain boundary regions (Figure 4.1(e) and (f)). One is a light colored phase having laminar type (or skeleton

TH-1394_09610307

form) features whereas the other is dark colored having fine particle like features. Similar features have also been reported in the literature [39, 234].

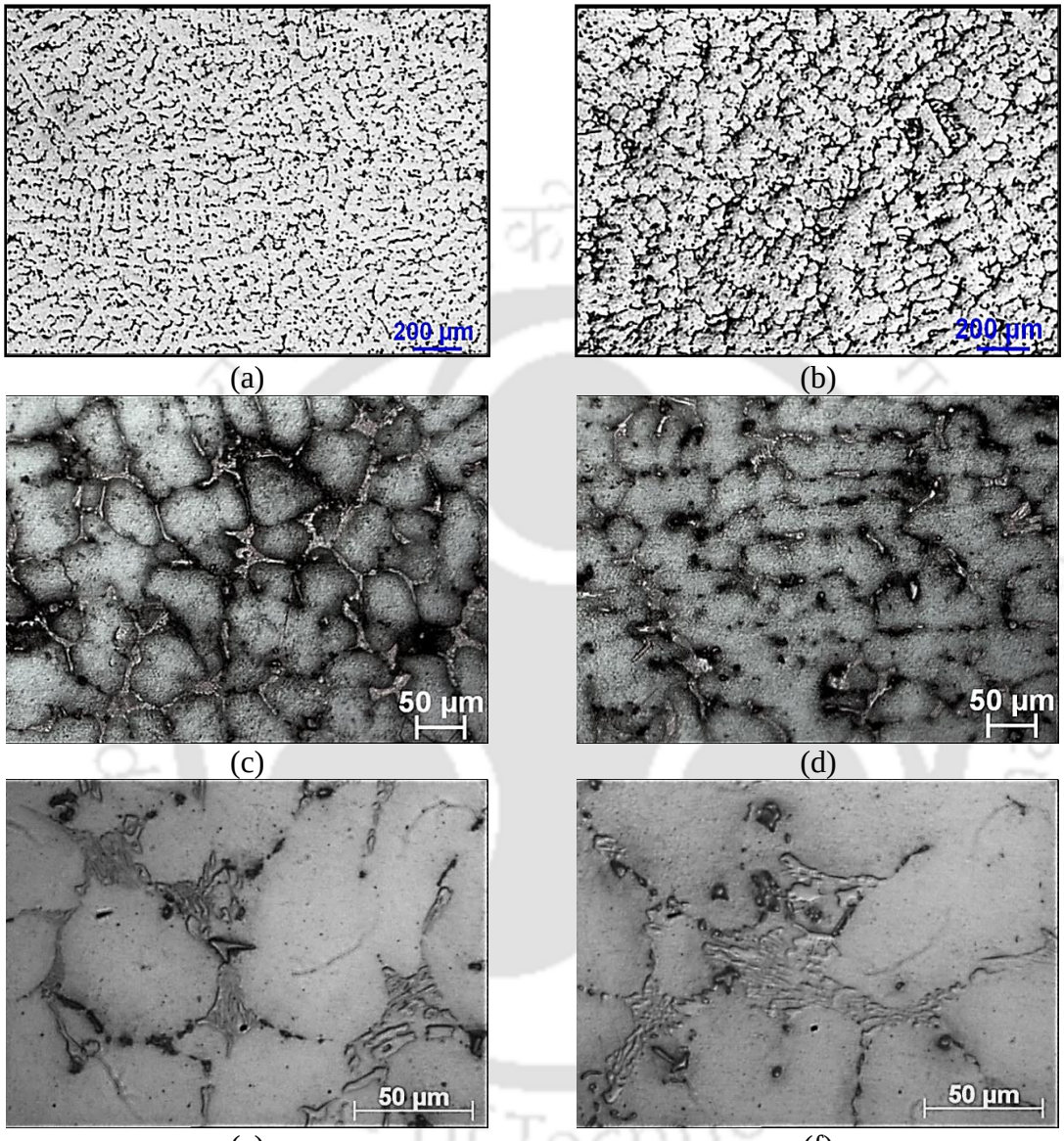

Figure 4.1. Optical micrographs of the steel at different magnifications. (a), (c) and (e) are for near inner-wall surface and (b), (d) and (f) are for near outer-wall surface.

Figure 4.2 shows the variation of the average grain size of the steel across the wall thickness. The figure shows an increase in grain size from 67 µm at the inside surface to 73 µm at the outside surface of the tube. Almeida et al. (2002) [28] and Alvino et al. (2010) [27] reported coarse grains at the outer surface of the tube compared to the inside surface in similar steels. The present steel under investigation was service exposed at 650 °C at the outer surface for prolonged period. The relative

coarse grains observed at the outer wall surface can be attributed to the slow rate of grain coarsening at the tube outer surface compared to the inner wall surface.

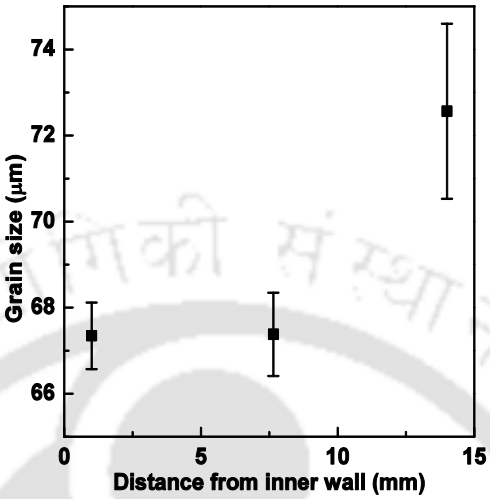

Figure 4.2. Variation of average grain size across the wall thickness of the reformer tube.

Figure 4.3 shows the SEM photomicrograph of the same specimen. SEM observation under back scattered mode reveals three different particles at the grain boundary regions of the austenitic matrix: (i) a dark gray phase (Phase-*A*) having a laminar (or skeleton type feature) type morphology, which was the major constituent of the second phase particles at the grain boundary region, (ii) a white phase (Phase-*B*) segregated at grain boundary and (iii) small quantities of very fine phase white particles (Phase-*C*).

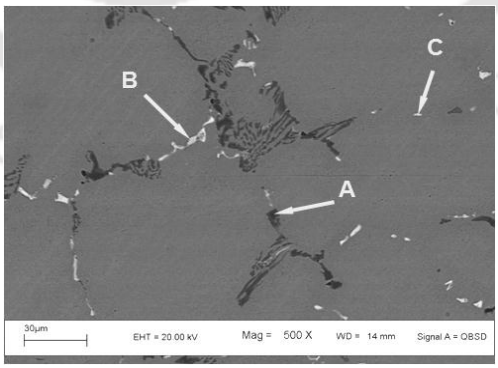

Figure 4.3. SEM backscatter electron image of as-received steel with phase *A*, phase *B* and phase *C* in matrix.

From the EDX spectrum shown in Figure 4.4, phase-*A*, phase-*B* and phase-*C* are identified as Cr–rich carbide, niobium rich carbide and (Nb,Ti) rich carbide, respectively.

TH-1394_09610307

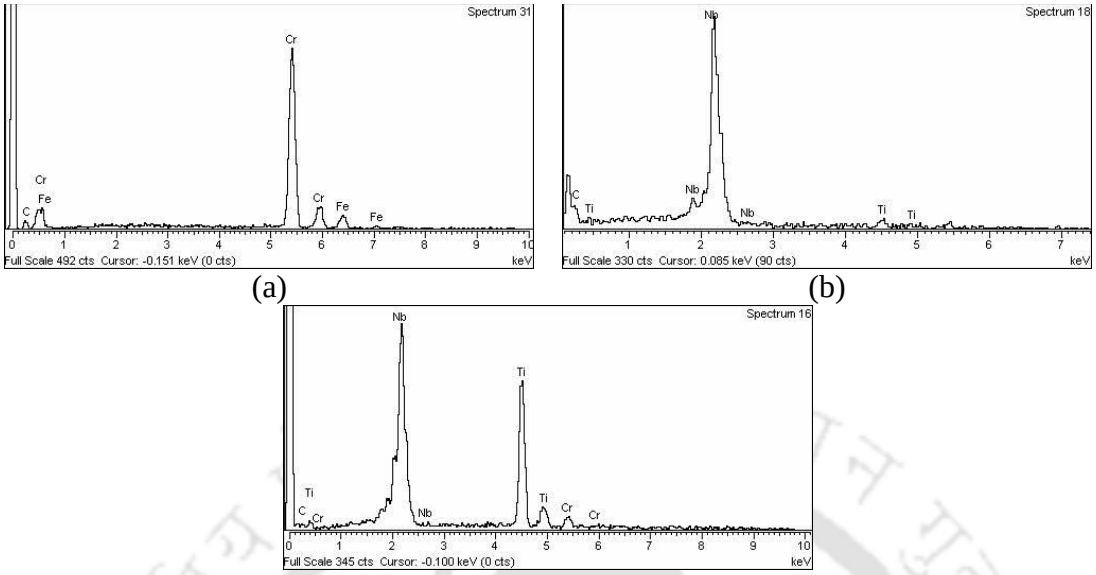

Figure 4.4. EDX spectrum of the (a) phase-*A*, (b) phase-*B* and (c) phase-*C* in the as-received steel.

Figure 4.5(b) shows the variation of results of the X-ray line scanning of Cr, Fe, Ni, C, and Nb across the line shown in the micrograph of Figure 4.5(a). The large second phase particle is identified as chromium carbide, whereas the small precipitate like phase on the right hand side of the micrograph is Nb rich carbide.

Figure 4.6 shows the distribution of Fe, Cr, Nb, Ti and Si obtained by X-ray elemental mapping confirming the results obtained by the X-ray line scanning.

4.2.3 X-ray Diffraction

Figure 4.7(a) shows the XRD pattern of the as-received steel sample. A comparison of the peaks with the JCPDS data indicates the presence of γ- Fe, Cr_7C_3, NbC, TiC and $Cr_{23}C_6$. The crystal structure of these phases are FCC (a = 3.6 Å), orthorhombic (a = 7.014 Å, b = 12.15 Å, c = 4.532 Å), FCC (a = 10.65 Å), FCC (a = 4.4 Å) and FCC (a = 4.6 Å), respectively. Earlier investigation by Soares et al. (1992) [33], Voicu et.al. (2009) [38] and Yan et al. (2011) [32] also revealed similar phases.

The XRD pattern of the second phase particles obtained in the powder form by the technique mentioned in section 3.2.5 is shown in Figure 4.7(b). The second phase particles are identified as consisting of Cr_7C_3, $Cr_{23}C_6$, NbC and TiC. Table 4.2 shows the 2θ values and its corresponding planes for these phases obtained in the carbide precipitates.

TH-1394_09610307

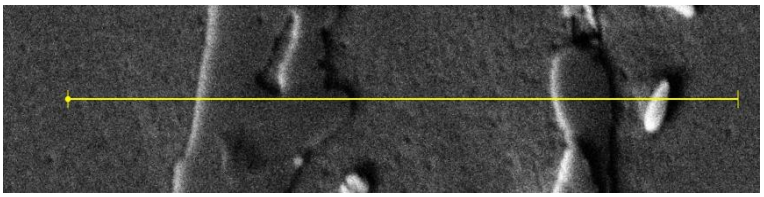

(a)

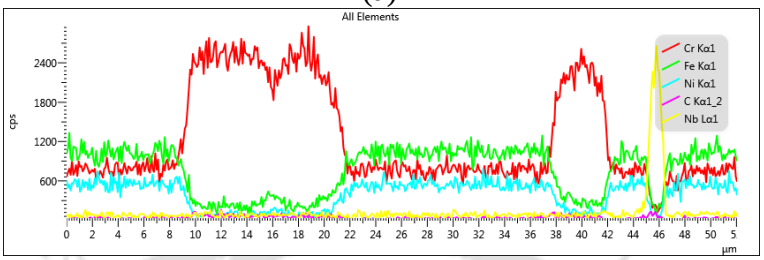

(b)

Figure 4.5. Elemental lines scan at a random region on as-received steel specimen.

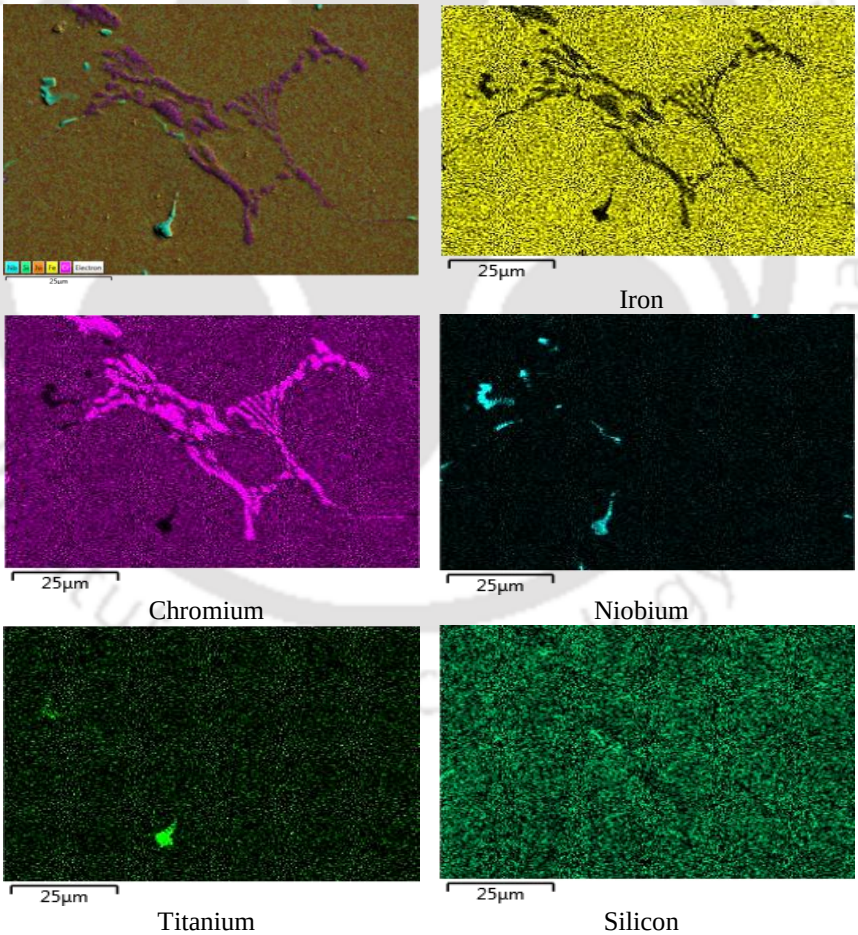

Figure 4.6. Elemental mapping of as-received steel.

Table 4.2. 2θ values and its corresponding planes for Cr_7C_3, $Cr_{23}C_6$, NbC and TiC phases taken from JCPDS file.

Cr_7C_3		$Cr_{23}C_6$		NbC		TiC	
2θ	hkl	2θ	hkl	2θ	hkl	2θ	hkl
39.19	150	37.74	420	35.30	111	33.72	111
42.55	112	41.51	422	40.99	200	39.13	200
44.17	151	44.15	511	59.36	220	56.54	220
44.70	060	48.30	440	70.99	311	67.47	311
50.19	222	50.67	531	74.67	222	70.91	222
		51.44	442				
		75.72	660				

The XRD pattern of the heat-treated steel specimen is shown in Figure 4.7(c). The pattern exhibits peaks corresponding to γ- Fe (FCC), $Cr_{23}C_6$ (FCC) and NbC (FCC). The figure does not reveal the presence of Cr_7C_3 in the steel matrix after heat treatment (exposure at 1000 ˚C for 72 hours followed by water quench).

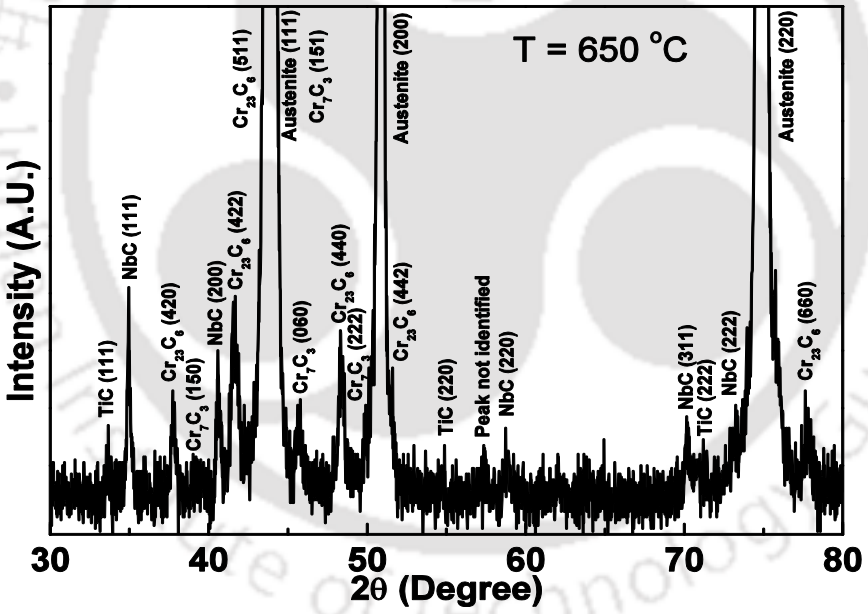

(a)

Figure 4.7. (a) XRD pattern of as-received steel.

TH-1394_09610307

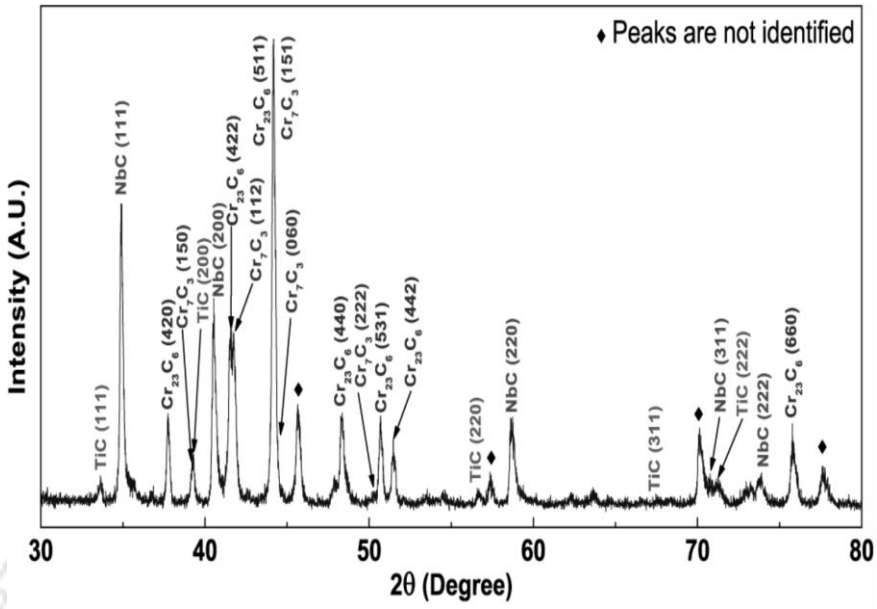

(b)

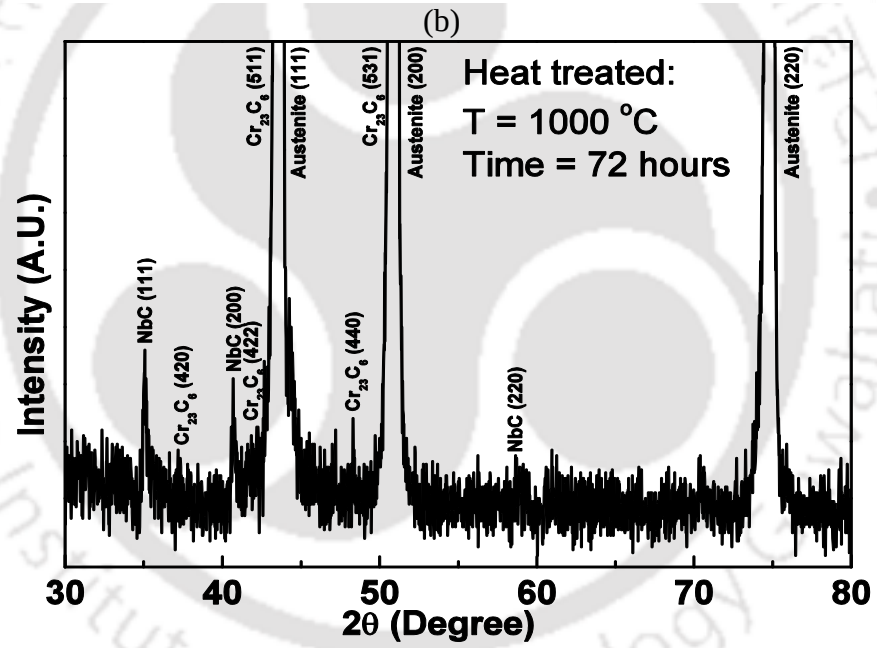

(c)

Figure 4.7. XRD patterns of (b) carbide precipitates of as-received steel and (c) heat treated steel sample at 1000 °C for 72 hours.

4.2.4 Transmission Electron Microscopy

The TEM picture of the fine particle showing the morphology along with selective area diffraction (SAD) pattern is shown in Figure 4.8. The micrograph reveals the average size of the particle as around 43 nm. Indexing of the SAD pattern confirmed these fine particles as orthorhombic Cr_7C_3 crystal structure with lattice parameters a = 7.014 Å, b = 12.15 Å and c = 4.532 Å.

TH-1394_09610307

The high resolution TEM (HR-TEM) image of Cr-rich phase present in the as-received steel is shown in Figure 4.9. The Inverse Fast Furrier Transform (IFFT) image shows a crystalline structure of the carbide precipitate. The study confirmed that the particle as Cr_7C_3 where the inter-planar spacing of (0 8 1) plane was measured as 1.442 Å.

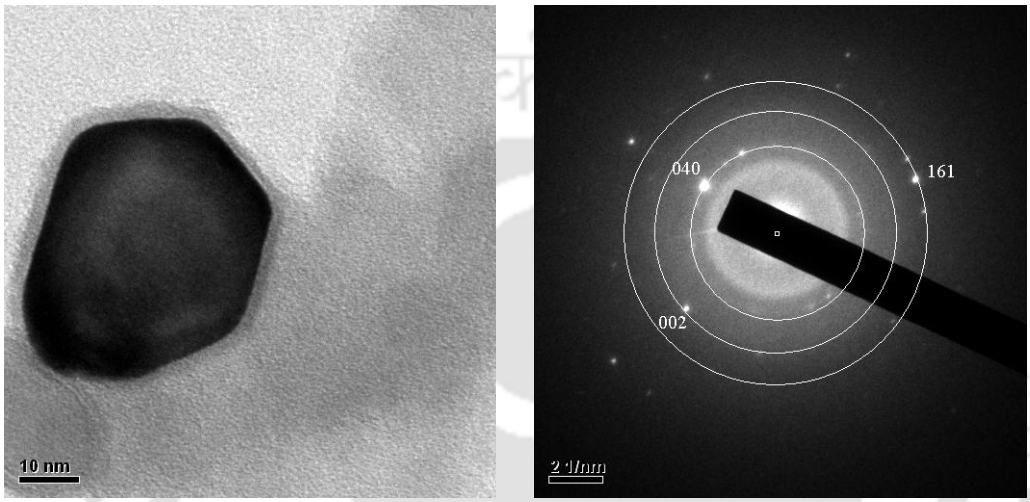

(a) (b)

Figure 4.8. (a) Bright-field TEM image and (b) corresponding indexed SAD pattern of the fine precipitate identified as Cr_7C_3 in the as-received steel.

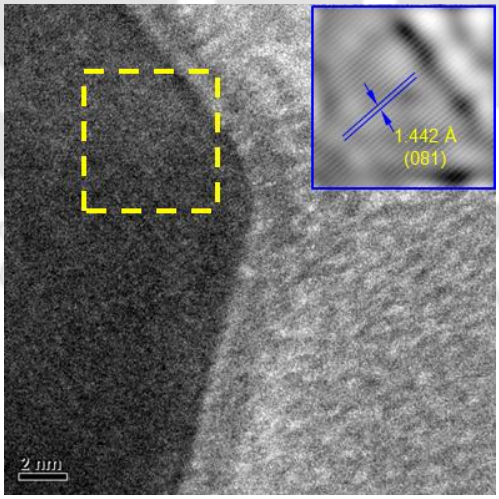

Figure 4.9. HR-TEM image of a Cr-rich fine precipitate.
Measurement of the lattice spacing indicated the precipitate is Cr_7C_3.

Figure 4.10 shows the TEM image and the SAD pattern of the carbide precipitate obtained from the steel heat-treated for 72 hours at 1000 °C. The size of these particles is determined to be around 292 nm in length and 137 nm wide. Analysis

TH-1394_09610307

of the SAD pattern of Figure 4.10(b) reveals the particle as face centered cubic structured $Cr_{23}C_6$ with a lattice constant of 4.6 Å.

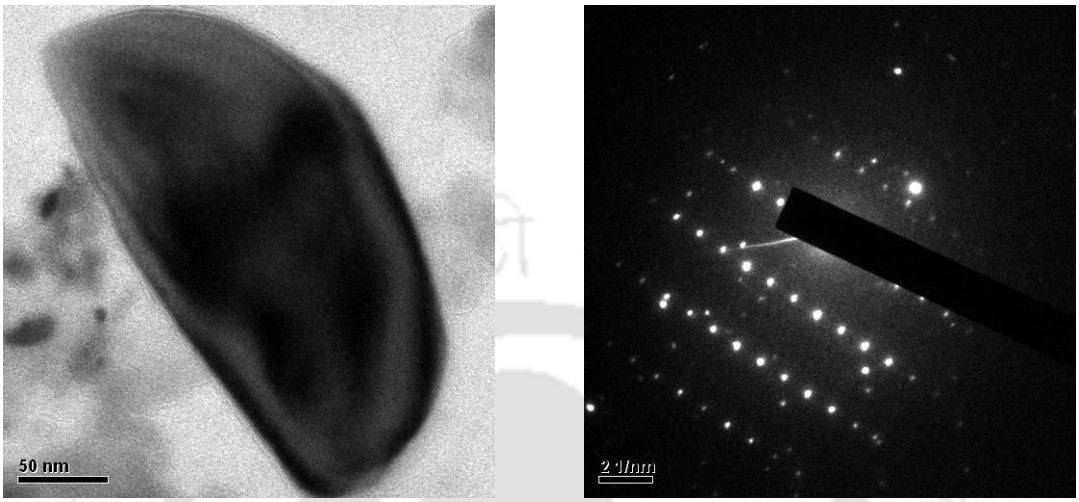

(a) (b)

Figure 4.10. (a) TEM bright-field image and (b) corresponding SAD pattern of the coarse precipitate identified as $Cr_{23}C_6$ in the heat-treated steel for 72 hours at 1000 °C.

Figure 4.11 shows the HR-TEM images of the particle. Measurement of the interplanar spacing at the selected areas revealed 1.875 Å and 3.777 Å which corresponds to (4 4 0) and (2 2 0) planes of $Cr_{23}C_6$. In this sample, the presence of Cr_7C_3 and NbC were not observed.

Investigation of the microstructure by OM, SEM-EDX, XRD and TEM reveals the presence of Cr_7C_3, NbC, TiC and $Cr_{23}C_6$ at the grain boundary regions of the centrifugally cast austenitic steel matrix. The Cr_7C_3 particle dissolves in γ-iron when heat treated above 1000°C. The high strength of the material at elevated temperatures is attributed to the presence of the carbides. The strength of the steel is expected to decrease with dissolution of the carbides at elevated temperatures.

TH-1394_09610307

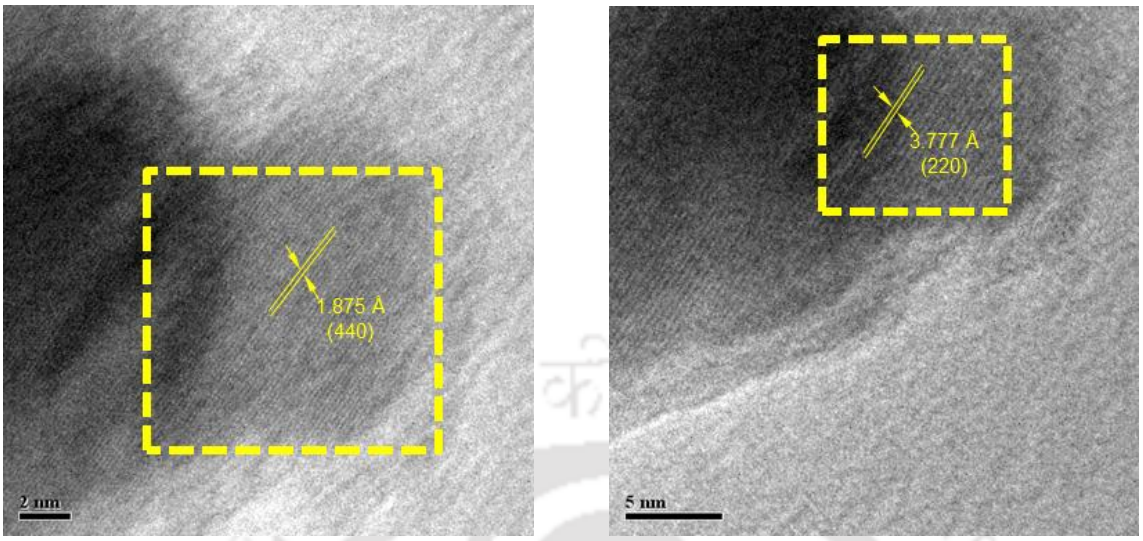

(a) (b)

Figure 4.11. HR-TEM images indicated interatomic layer spacing found by Fourier transform of a Cr-rich precipitate in the heat-treated steel for 72 hours at 1000 °C. Measurements of the lattice spacing indicated the $Cr_{23}C_6$ precipitate.

4.3 Mechanical Properties of the Steel

4.3.1 Hardness Properties

Variation of Vickers hardness (HV) of the steel across the wall thickness of the reformer tube is shown in Figure 4.12. Though the hardness of the investigated steel was found to be higher than that reported in the literature [29, 39, 204, 235], only a marginal increase in the hardness (~4.5%) is observed across the tube thickness. The high hardness obtained for the present steel is due to the fact that the literature reported values are for the steels that have failed by creep deformation.

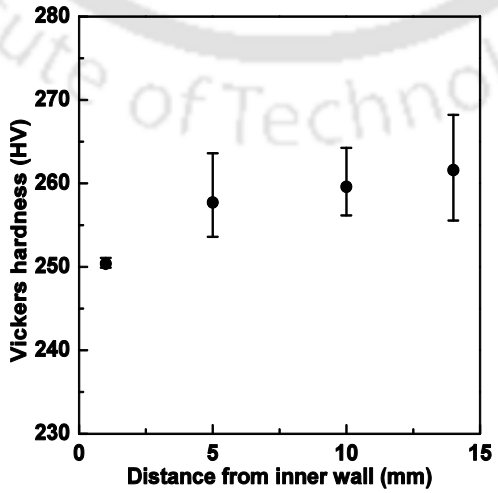

Figure 4.12. Variation of Vickers hardness across the wall thickness of the reformer tube.

TH-1394_09610307

4.3.2 High Temperature Tensile Properties

Table 4.3 shows the results of the tensile tests at various temperatures.

Table 4.3. Tensile test results of the steel at elevated temperatures.

Temperature (°C)	*E* (GPa)	YS (MPa)	UTS (MPa)	Elongation (%)
27	167.8	213	364.9	6.5
200	178.4	152	299.5	5
400	171.9	148	316.3	6.8
600	165.4	130.2	331.1	11.4
800	141.3	86.2	119.1	17.8
1000	72	31.7	42.9	38.9
1200	38.2	20.2	21.3	7.8

Figure 4.13(a)-(c) show the plot of Young's modulus *E*, yield strength (YS) and ultimate tensile strength (UTS) of the steel tested at various temperatures. Due to unavailability of standard data, the test results are compared with the values of the as-cast material reported by the manufacturer [236]. Figure 4.13(a) shows a marginal decrease in *E* value when the test temperature was raised from 27 ˚C to 600 ˚C. A rapid and continuous decrease in Young's modulus is observed as the test temperature is raised from 600 ˚C to 1200 ˚C. The service exposed steel shows higher value up to a test temperature of 800 °C compared to the manufacturer's reported value of the as-cast steel. With further increase in the test temperature Young's modulus is found to be lower than that of the as-cast steel. At 800 °C test temperature, Young's modulus of the investigated steel was found to be 31% higher than the as-cast steel reported. However, above 1000 °C, a reverse trend was observed. At 1000 °C, Young's modulus value of the as-cast steel is 32 % higher than that of investigated steel.

Figure 4.13(b) indicates a continuous decrease in YS with increase in temperature. The lower value of YS is observed for the service exposed steel at all test temperatures compared to the manufacturer's data. At 800 °C, the YS of the as-cast steel reported by the manufacturer is 58 % higher than that of investigated steel. From Figure 4.13(c), the ultimate tensile strength (UTS) of the steel is found to decrease marginally when the temperature is increased up to 600 °C. With further increase in test temperature, a rapid decrease in UTS is observed. The UTS values reported by the manufacturer are 19 %, 54 % and 63 % higher than that for the investigated UTS value at test temperature 27 °C, 800 ˚C and 1000 ˚C, respectively. The decrease of *E*, YS and

TH-1394_09610307

UTS value with increase in temperature compared to as-cast indicates that the material has become degraded due to prolonged service exposure. Ductility of the steel at lower temperature is low and increased with increase in temperature up to 1000 ˚C. However, the percentage elongation decreased from 22.6 % to 7.8 % with increase in temperature from 1000 ˚C to 1200 ˚C.

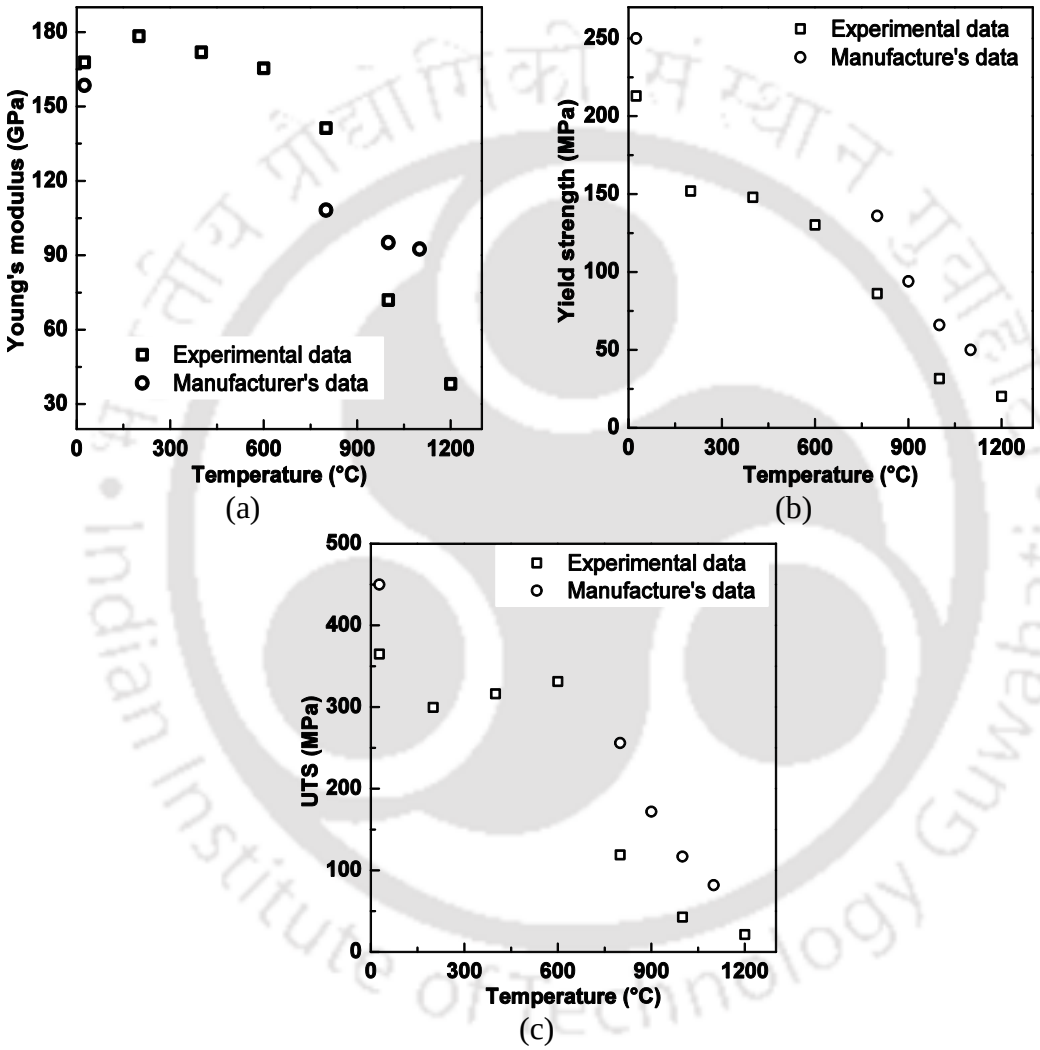

Figure 4.13. (a) Young's modulus, (b) yield strength and(c) ultimate tensile strength as a function of temperature.

True stress-true strain curves and strain to failure obtained for the steel at various test temperatures are shown in Figure 4.14(a)-(b). The flow stress of the steel is strongly dependent on the test temperature. Figure 4.14(b) indicates low failure strains ε_f for the material at lower temperatures up to 600 ˚C. Within this temperature region, the onset of plastic deformation is accompanied by high strain hardening rate $d\sigma/d\varepsilon$, which

TH-1394_09610307

decreases with increase in strain. At a test temperature of 800 °C, the onset of plastic deformation was accompanied by a strain hardening region up to a true strain or around 0.015, beyond which effectively no strain hardening was observed. The material undergoes a large amount of plastic deformation at a constant stress, prior to failure. At 1000 °C, the material behaved as if perfectly plastic material. The true plastic strain to failure at 1000 °C was 0.21. However, above 1000 °C, the steel was perfectly plastic. However, the material was characterized by sharp loss in ductility. At 1200 °C, the yield strength of the material was 20 MPa with a true strain to failure value of 0.075.

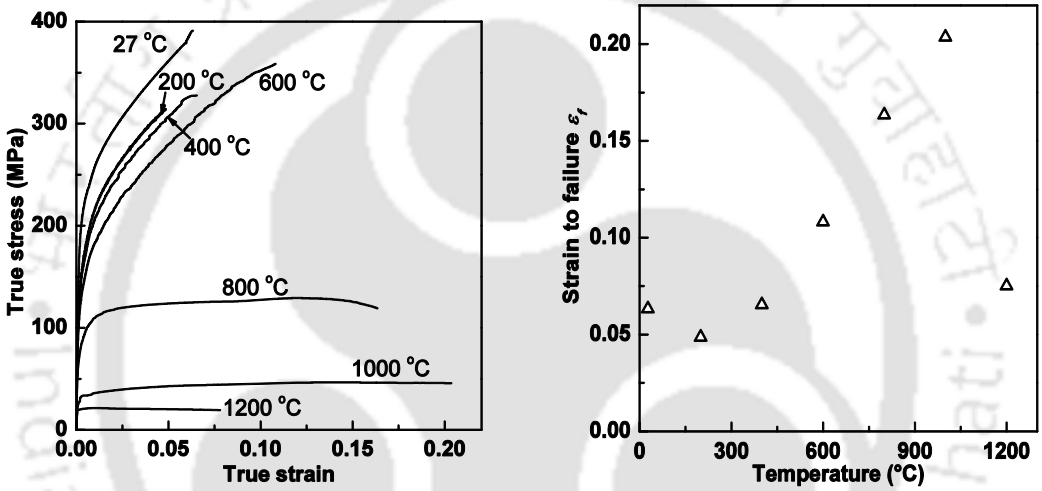

Figure 4.14. (a) True stress-true strain curves at various test temperatures and (b) strain to failure as a function of temperature.

The plot of strain hardening exponent *n* versus temperature is shown in Figure 4.15. The value of *n* increase with increase in the test temperature up to 600 °C. After reaching a maximum value of 0.284, *n* is found to decrease sharply with increase in test temperature. At 1200 ˚C, the value of *n* was determined to be 0.05 which indicates negligible work hardening.

Figure 4.16 shows the photographs of the tensile specimen after fracture. The specimen tested up to 600 ˚C illustrates that the fracture occurred in the direction almost perpendicular to the specimen axis. At the test temperature of 800 °C and 1000 °C necking was observed. The specimen tested at 1200 °C shows that the fracture surface is inclined at an angle to the transverse axis of the specimen.

TH-1394_09610307

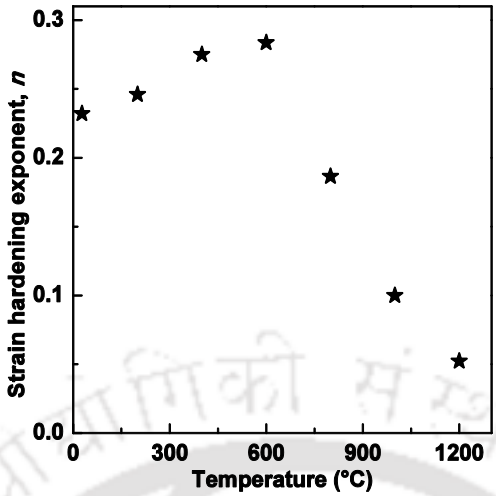

Figure 4.15. Strain hardening exponent as a function of temperature.

Figure 4.17(a)-(j) show the SEM fractographs of the specimen, tensile tested at different temperatures. Low magnification observation of the sample tested at 27 ˚C reveals quasi cleavage features. A few number of large void like features can be seen on the fracture surface as shown in Figure 4.17(a). Observation at high magnification as shown in Figure 4.17(b), reveals trans-granular cleavage features and micro-cracks on the fracture surface indicating the dominant failure as a brittle failure. Similar features are observed in samples tested at temperatures up to 600 ˚C as shown in Figure 4.17(c) and (d).

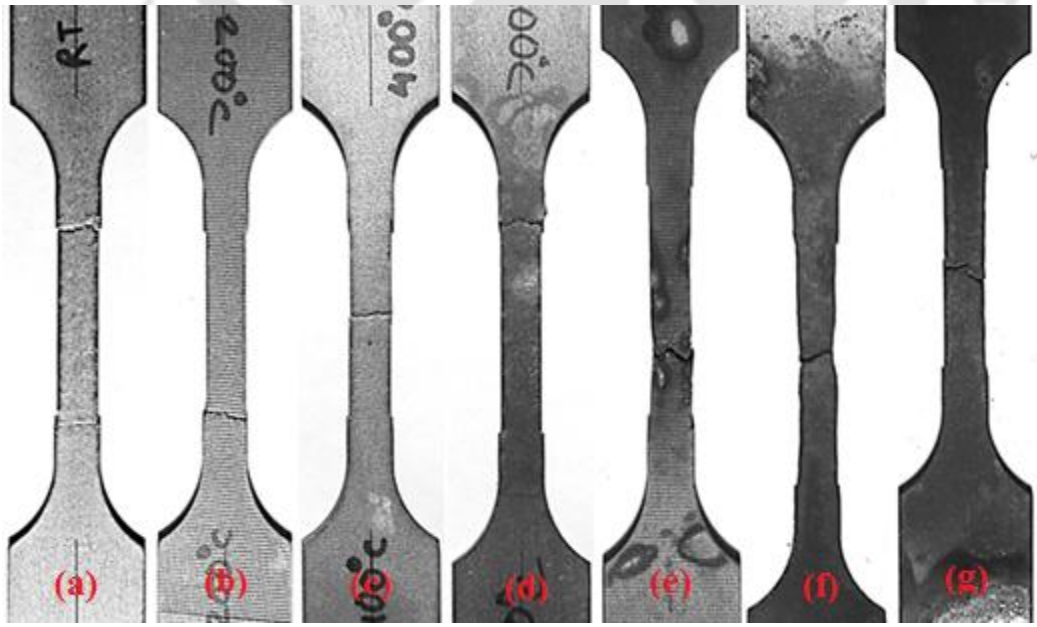

Figure 4.16. Photographs of fractured tensile specimens tested at (a) 27 °C, (b) 200 °C, (c) 400 °C, (d) 600 °C, (e) 800 °C, (f) 1000 °C and (g) 1200 °C.

TH-1394_09610307

The fractographs of the sample tested at 800 ˚C are shown in Figure 4.17(e) and (f). The features indicate extensive plastic deformation of the grains before final failure. Since, the microstructure of the material revealed carbides present at grain boundary regions, during the tensile loading at temperatures up to 1000 ˚C, the main mechanism of failure can be due to the deformation of the grains by multiple slip rather than by micro-void coalescence. Figure 4.17(g) & (h) show SEM fractograph of the sample tested at 1200 ˚C, indicating inter-granular failure. Low magnification observation indicates the presence of large voids. Observation at high magnification shows voids and micro-cracks at particle-matrix interface and grain boundary regions.

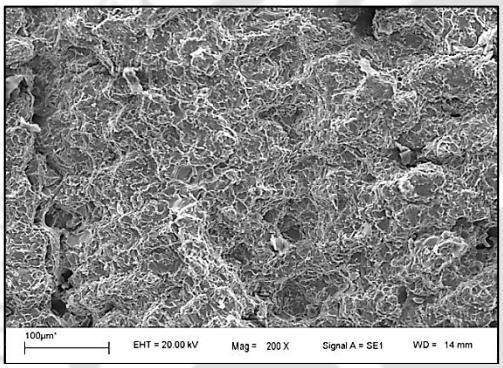

(a)

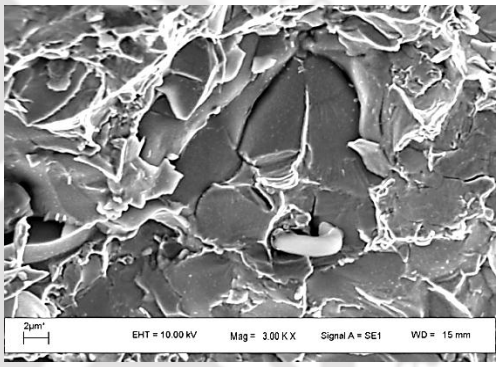

(b)

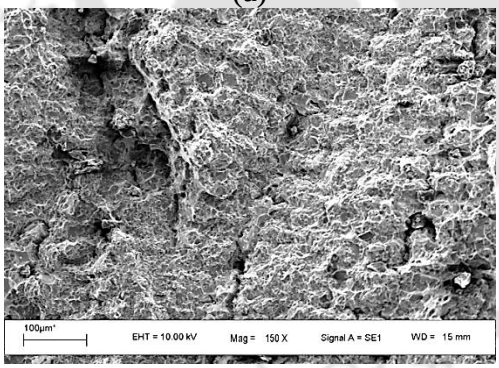

(c)

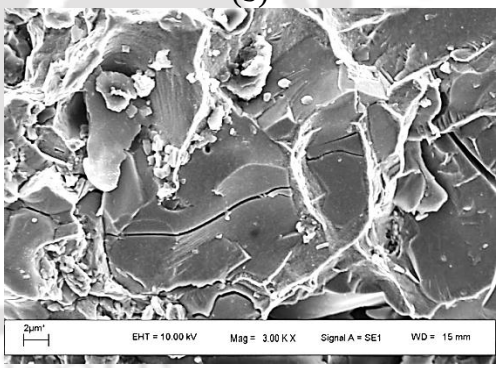

(d)

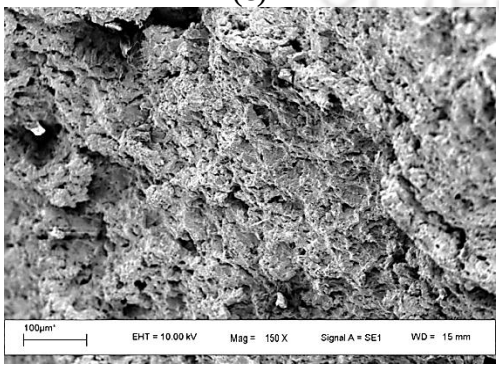

(e)

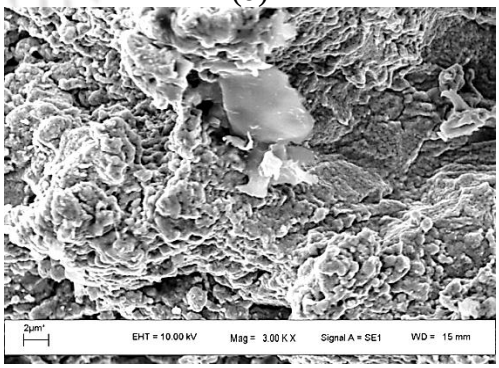

(f)

TH-1394_09610307

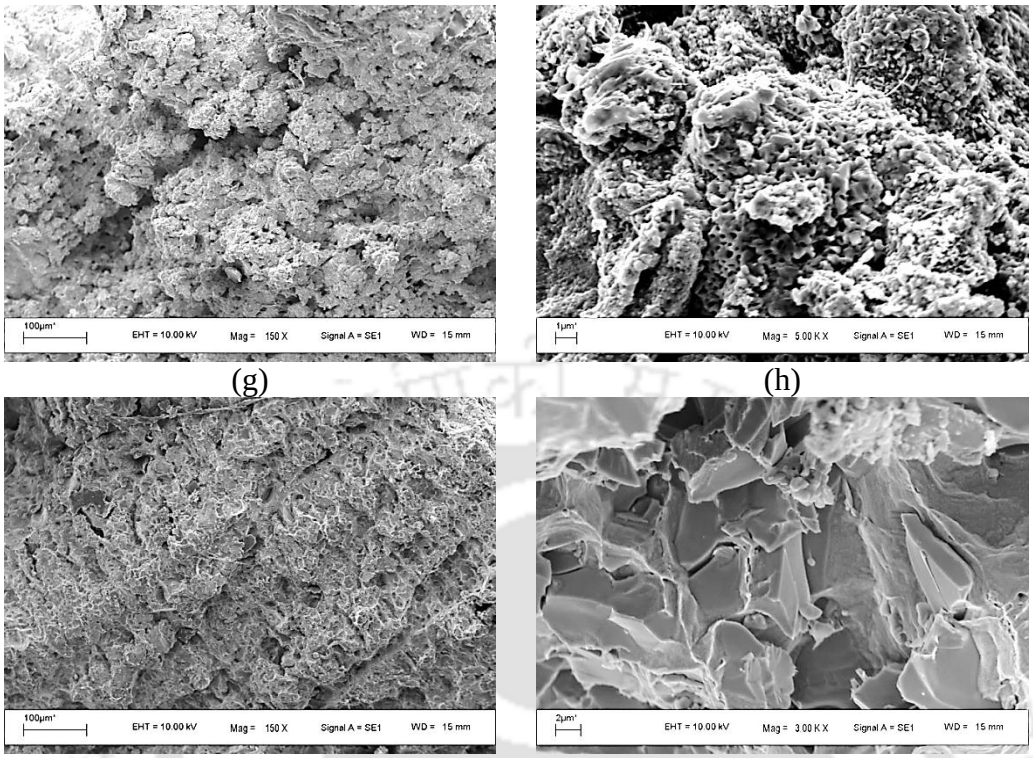

(g) (h)

(i) (j)

Figure 4.17. SEM fractographs of tensile tested samples at (a) & (b) 27 °C, (c) & (d) 600 °C, (e) & (f) 800 °C, (g) & (h) 1000 °C and (i) & (j) 1200 °C at lower and higher magnification.

OM observation (Figure 4.18) of the longitudinally sectioned and the polished surface of the samples tested at 1200 ˚C revealed voids nucleated at the carbide-matrix interfaces at regions of grain boundaries. The propagation of the voids is along grain boundary regions. The features indicate coalescence of the micro-voids nucleated at the particle-matrix interface and the fracture path is along the grain boundaries. The low ductility exhibited by this steel at 1200 ˚C is due to inter-granular failure.

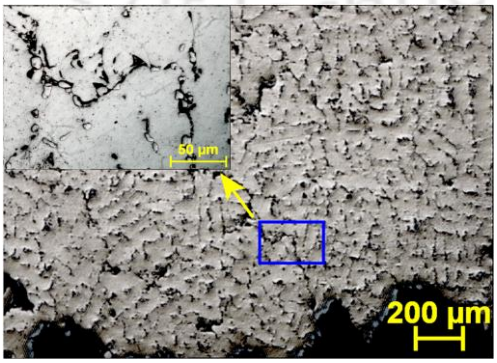

Figure 4.18. Optical micrograph of longitudinal gauge section of the specimen tensile tested at 1200 ˚C.

TH-1394_09610307

4.3.3 Creep Test

The results of the creep tests carried out on the steel are presented and discussed in the following sub-sections. The development and the analysis of load-displacement behavior during creep test, creep behavior, constitutive equations for creep, creep mechanism, fracture behavior during creep, Monkman-Grant and modified Monkman-Grant relationship, creep damage tolerance factor, different creep rupture parameterization techniques and creep life of the steel are discussed.

4.3.3.1 Load-Displacement Behavior

The load vs. displacement plot obtained from creep tests on HP40Nb micro-alloyed steel at various temperatures and stress levels are shown in Figure 4.19. Maximum percentage deviation and RMS error for 700 °C/120 MPa, 850 °C/80 MPa, 800 °C/68 MPa and 950 °C/47 MPa are given in Table 4.4 and indicating satisfactory values.

4.3.3.2 Creep Curves

Creep curves obtained from all the 22 experiments are shown in Appendix-VII. The nature of the creep curve depends on the test temperature and stresses. From the creep curves, the following observations are made:

- The total time to failure decreased with increase in temperature at a particular applied stress
- The total time to failure decreased with increase in applied stress at a particular temperature
- The three well defined creep stages are found only for combinations of low or intermediate applied stresses and temperatures.
- At high temperatures and / or applied stresses, steady state creep region was almost absent.

TH-1394_09610307

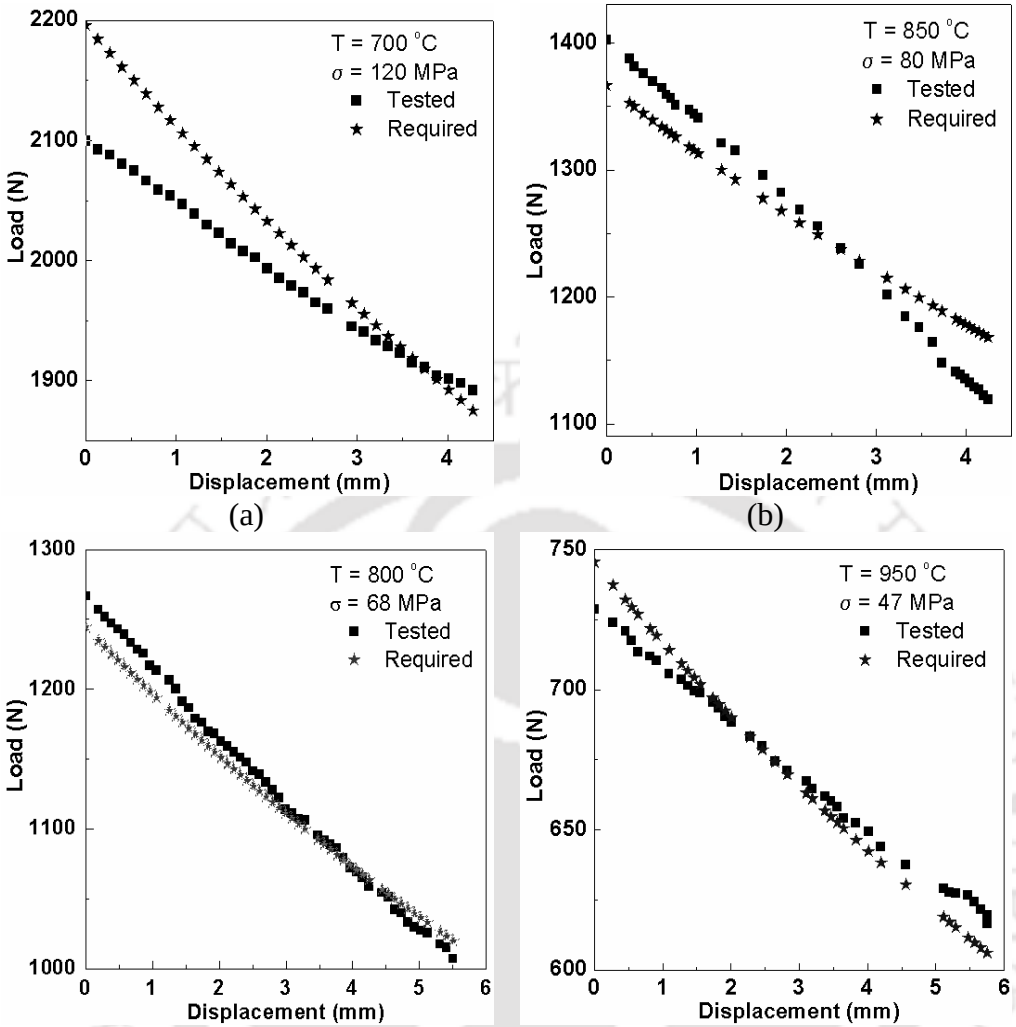

Fig. 4.19. Load vs. displacement plot for (a) 700 °C/120 MPa, (b) 850 °C/80 MPa, (c) 800 °C/68 MPa and (d) 950 °C/47 MPa.

Table 4.4. Maximum percentage deviation and RMS error for various true stresses and temperature.

True Stress (MPa)	Temperature (°C)	Maximum deviation (%)	RMS error (N)
120	700	+0.90 -4.40	49.10
80	850	+2.62 -4.17	31.37
68	800	+1.90 -1.25	13.10
47	950	+2.46 -2.26	8.66

Few of the creep curves obtained for the steel at constant stress and temperatures plotted on linear scale are shown in are shown in Figure 4.20 and Figure 4.21 respectively.

TH-1394_09610307

Figure 4.20(a) illustrates creep curves of the steel tested at 47 MPa stress and at 800 °C, 900 °C and 1000 °C. At 800 °C, the primary creep region was followed by a long constant creep rate region. The tertiary creep region was reached after a strain of 0.075, and the final failure occurred at a strain of around 0.112. The failure strain increased with increase in temperature. The tertiary creep strain decreases with increase in temperature. The steady state creep rate increased with increase in test temperature. Similar trend is observed in creep curves obtained when tested at 68 MPa, 80 MPa and 120 MPa.

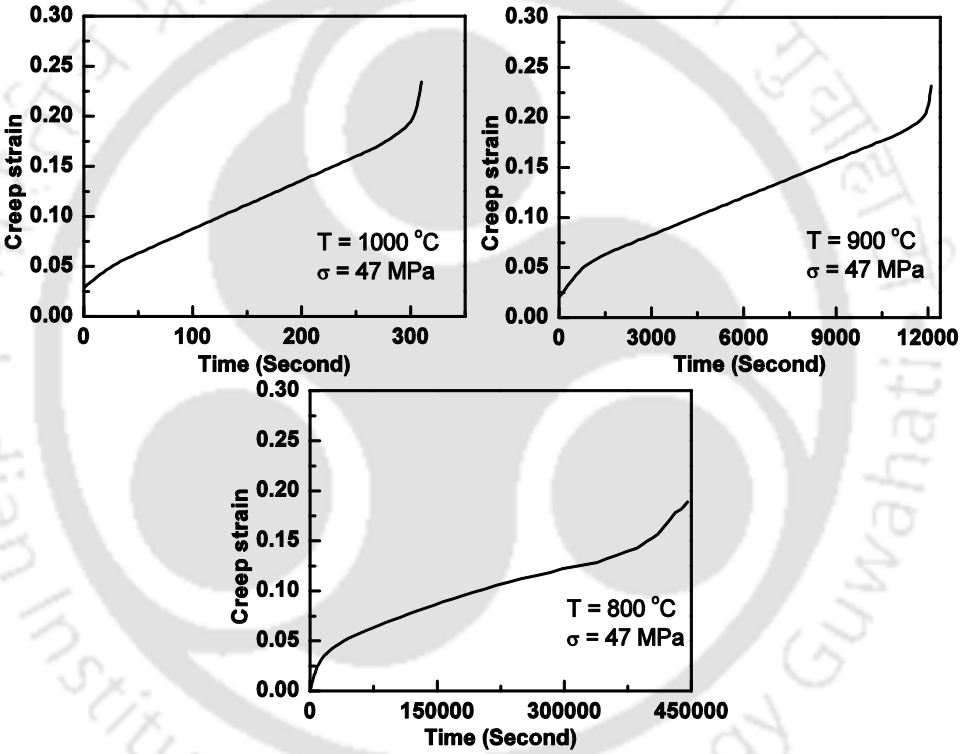

Figure 4.20. (a) Creep curves at stresses of 47 MPa for different temperatures.

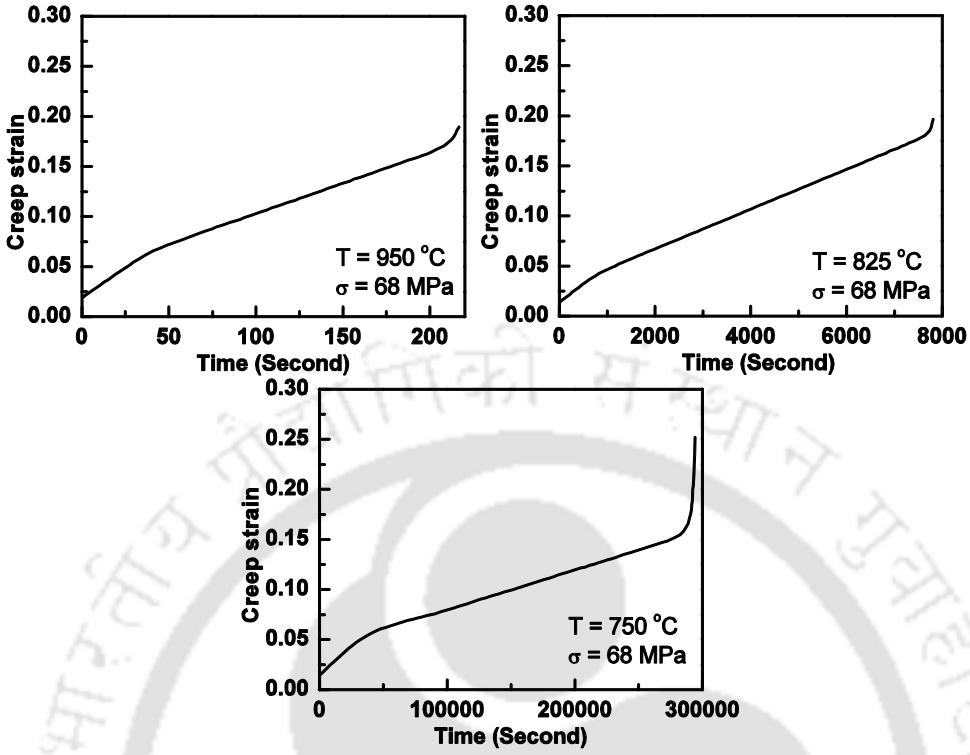

(b)

Figure 4.20. (b) Creep curves at stresses of 68 MPa for different temperatures.

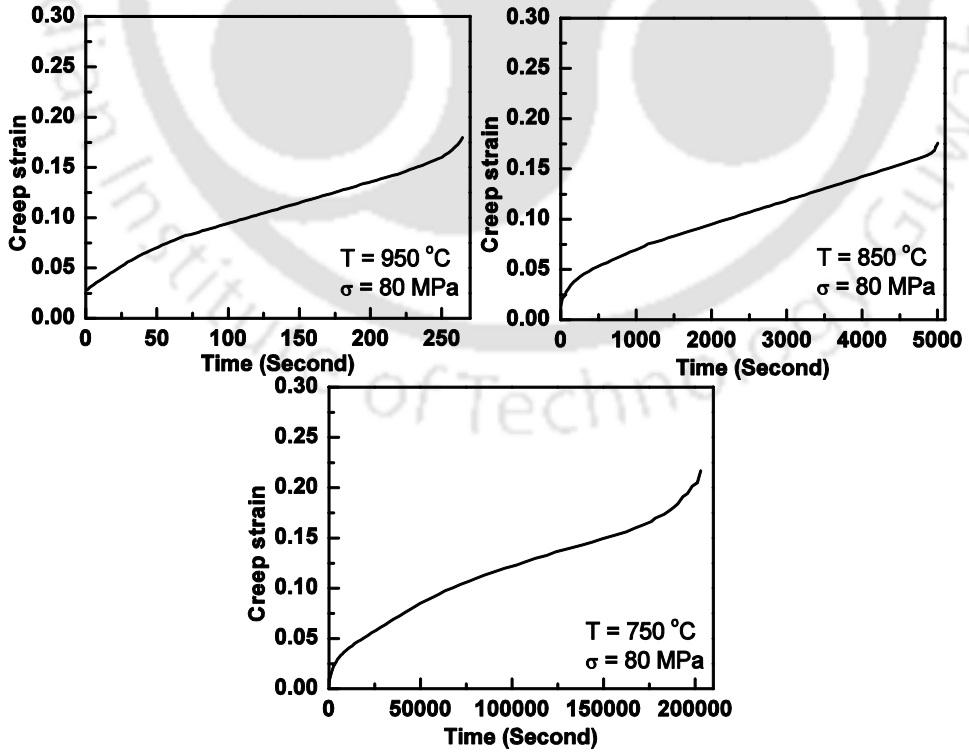

Figure 4.21. (a) Creep curves at stresses of 80 MPa for different temperatures.

TH-1394_09610307

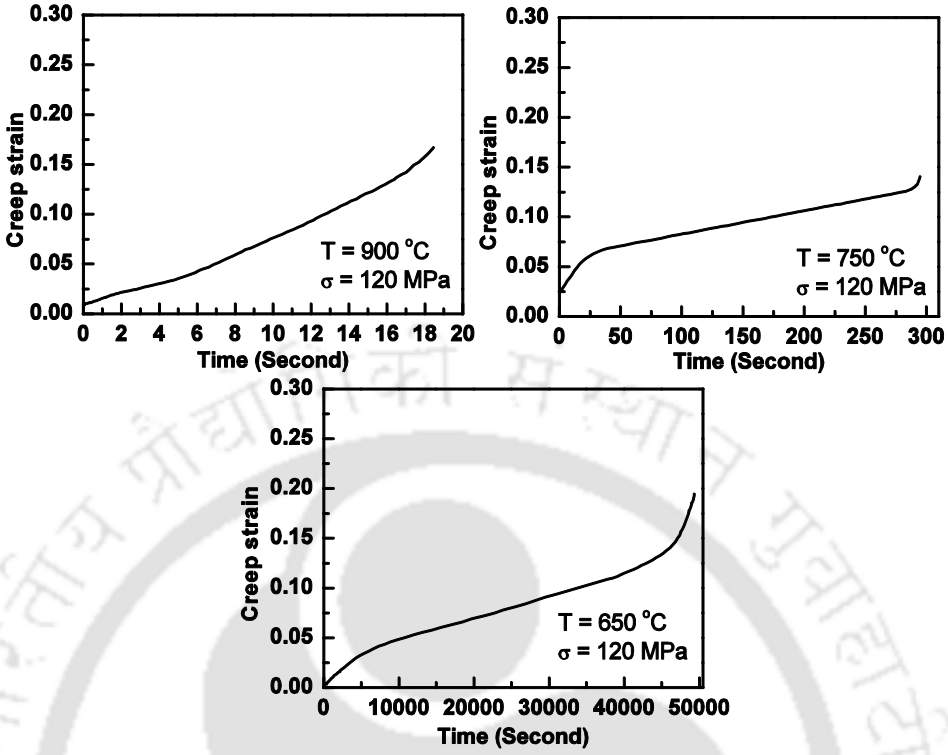

(b)

Figure 4.21. (b) Creep curves at stresses of 120 MPa for different temperatures.

Figure 4.22(a) shows the effect of temperature on the creep curve at an applied constant stress of 80 MPa. Figure 4.22(b) shows the effect of applied stress on the creep curve at 900 °C. At high stress and high temperature the extent of primary stage is reduced and eliminates the secondary stage. Under these circumstances, the creep rate accelerates almost from the beginning of the creep test and the tertiary creep stage is reached at the early stages of creep deformation. At lower temperatures and stresses, creep curves with three well defined stages are found. The well-defined second stage creep is pronounced under conditions that favor very slow creep rate.

Figure 4.23(a) to (d) show the plot of creep strain rate vs. strain plots for the four stresses. At lower stress or temperature, the creep curves show long and well defined secondary creep region. The initial stage of creep deformation is characterized by a continuous decreasing strain rate. This is since at lower temperatures or stresses, the dislocation motion becomes extremely difficult since the density of dislocation and other lattice defects increase with increase in strain. Since the material is at elevated temperature, the thermal activation may allow the flow of metal to take place. The combined effect of the above phenomenon results in continuous decrease in strain rate

TH-1394_09610307

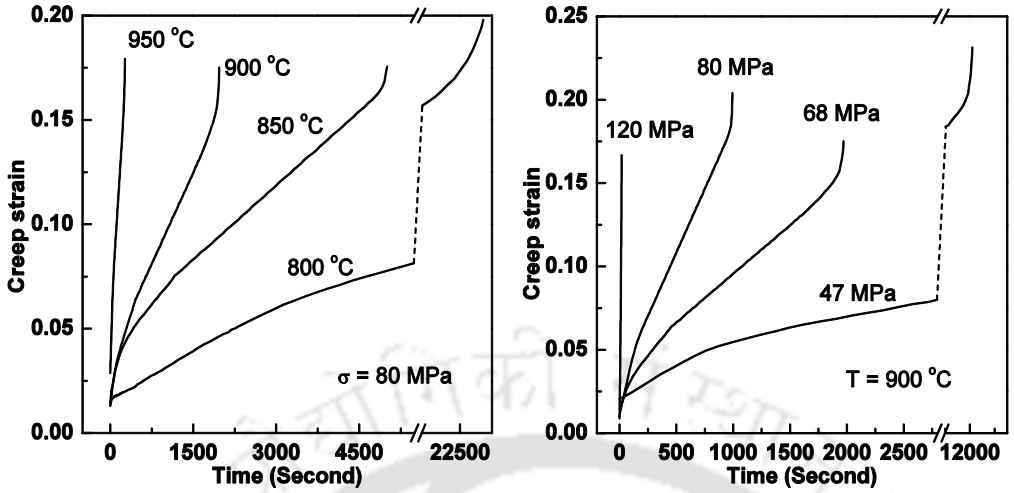

Figure 4.22. Creep curves at (a) constant stress of 80 MPa and (b) constant temperature of 900 °C.

in the primary creep region. The process continues till the rate of work hardening is well balanced by the rate of metal flow and softening due to recovery. Under these conditions, the creep deformation enters the secondary stage (or steady state creep region) where the strain rate attains a constant minimum value. The total strain in the secondary creep region contributes to the effective creep life of the material. In the range of temperature and stresses where recovery occurs, defects like void nucleation at grain boundary region and inter-crystalline fracture can occur with prolonged time. Void nucleation results in decreased effective cross sectional area carrying the load *i.e.* effectively the stresses are increased. Under this condition growth of the voids is liable to occur thereby accelerating the creep rate and the deformation gradually enter the tertiary creep stage. Once the tertiary stage is reached, the void growth accelerates, resulting in increased creep rate with increase in strain leading to the final failure.

At higher temperatures the thermal activation permits softening and the metal flow at a faster rate. The work hardening rate reduces with increase in temperature due to annihilation of dislocations or vacancies resulting in metal softening. The combined effect of the two phenomenon results in acceleration of the creep rate almost from the beginning of the creep test and hence, as evident from Figure 4.22 and 4.23, the secondary creep region is almost absent at high temperatures. At 47 MPa, 68 MPa, 80 MPa and 120 MPa the strain range for minimum creep rates at the investigated temperatures lies between 0.0007 - 0.28, ε = 0.017 - 0.21, ε = 0.0077 - 0.22 and ε =

TH-1394_09610307

0.0032 - 0.19 respectively. The creep strain for most of the combination of stresses and temperature was found centered around 0.2.

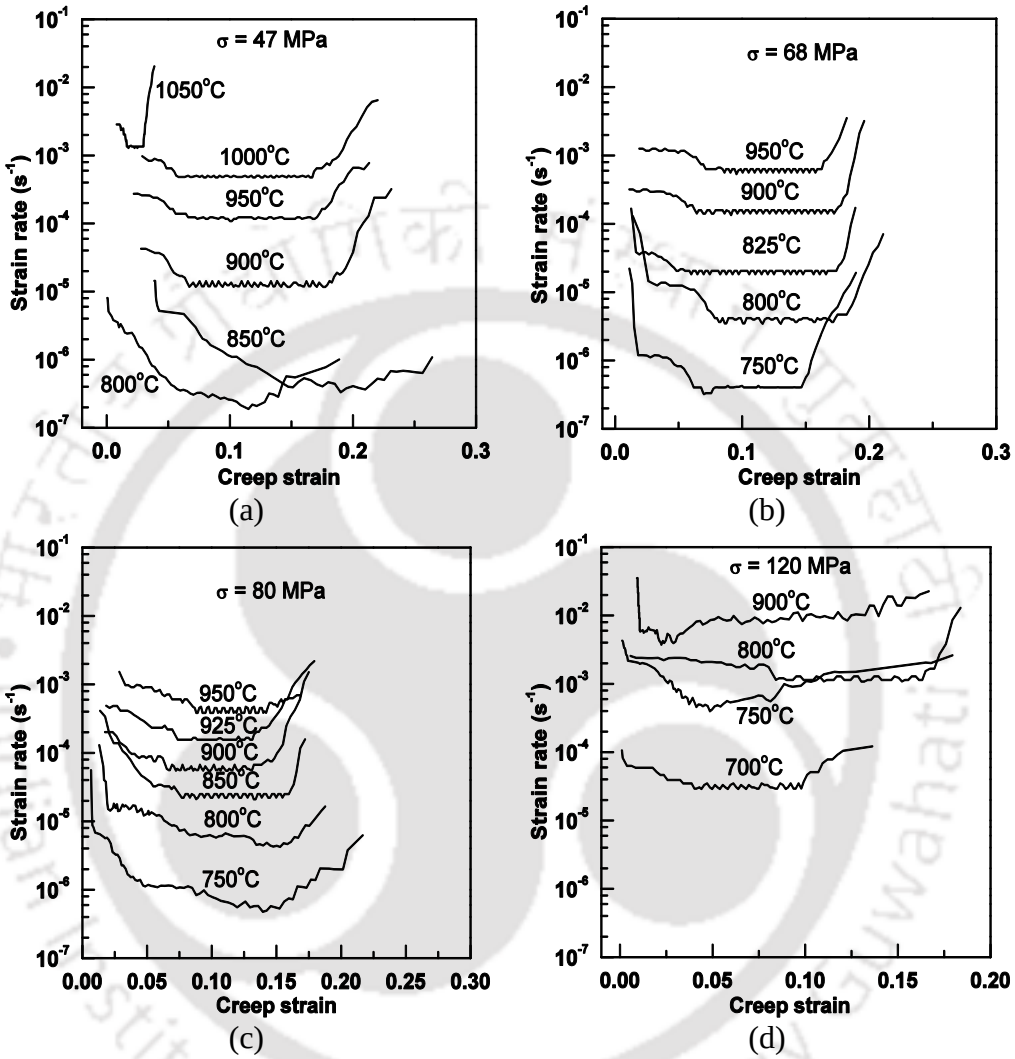

Figure 4.23. Variation in creep strain rate $\dot{\varepsilon}$ with increasing creep strain at stresses (a) 47 MPa, (b) 68 MPa, (c) 80 MPa and (d) 120 MPa for different temperatures.

4.3.3.3 Creep Strains and Rupture Time

Figure 4.24(a) & (b) show semi-logarithmic plots of the strains (ε_2 and ε_f) and relative strains $\varepsilon_i/\varepsilon_f$ (where i = 1, 2 and 3) vs. minimum creep rate $\dot{\varepsilon}_s$ obtained from all the experiments. The maximum value of strain to rupture and secondary strain were found to be 0.28 and 0.26, respectively. As shown by the trend lines, the strains (ε_2 and ε_f) tend to decrease with increasing minimum creep rate. Figure 4.24(b) indicates high scatter in the experimental data for the relative secondary strain $\varepsilon_2/\varepsilon_f$ and tertiary strain

TH-1394_09610307

$\varepsilon_3/\varepsilon_f$. The trend lines shown in Figure 4.24(b) indicate an increasing trend for the relative secondary strain vs. minimum creep rate whereas the relative primary and tertiary strains show a decreasing trend. Average values for the relative secondary strain and tertiary strain are 60 % and 18 % respectively.

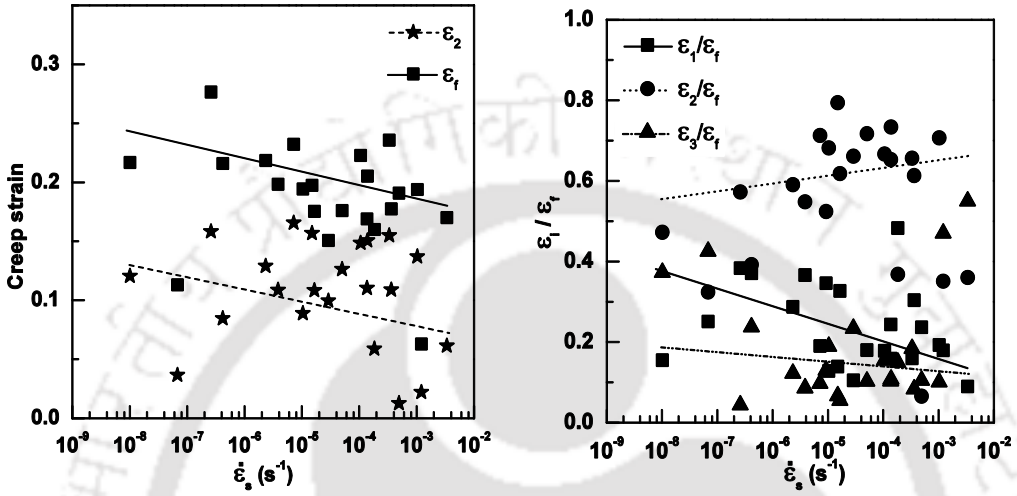

(a) (b)

Figure 4.24. Effect of (a) strain to rupture, secondary strain and (b) relative strain for three creep regions on minimum creep rate of the steel.

Figure 4.25(a) shows the plot of ε_2 and ε_f vs. applied stress, obtained from tests carried out at 750 ˚C and 900 ˚C. For both cases, ε_2 and ε_f decrease with increase in stress. Figure 4.25(b) shows the plot of relative secondary strain vs. stress. The relative secondary strain $\varepsilon_2/\varepsilon_f$ decreases with increase in stress. Similar trend was observed at all temperatures investigated.

Figure 4.26(a) shows the plot of ε_2 and ε_f vs. T at 47 MPa and 80 MPa. The figure indicates a large scatter in the data. The figure shows a marginal increase in ε_2 with increase in temperature, whereas, the rupture strain decreased with increase in temperature. Figure 4.26(b) indicates the contribution of secondary strain to the total rupture strain. The relative secondary strain increases with increase in temperature up to 1000 °C at constant stress. The results also indicate that the contribution of secondary strain increases with the increase in stress up to 900 °C.

TH-1394_09610307

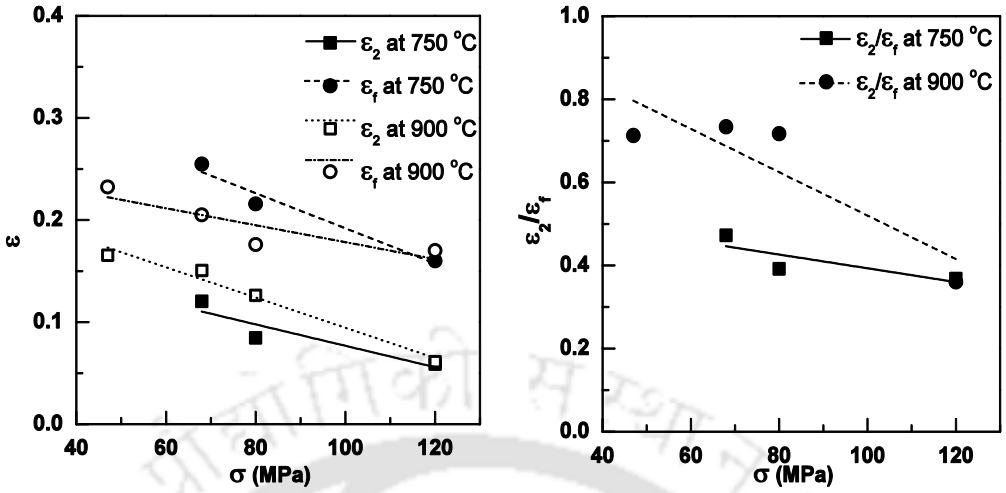

(a) (b)

Figure 4.25. Effect of stress on (a) strain to rupture, and secondary strain and (b) relative strain in secondary region, of the steel at temperatures of 750 ˚C and 900 ˚C.

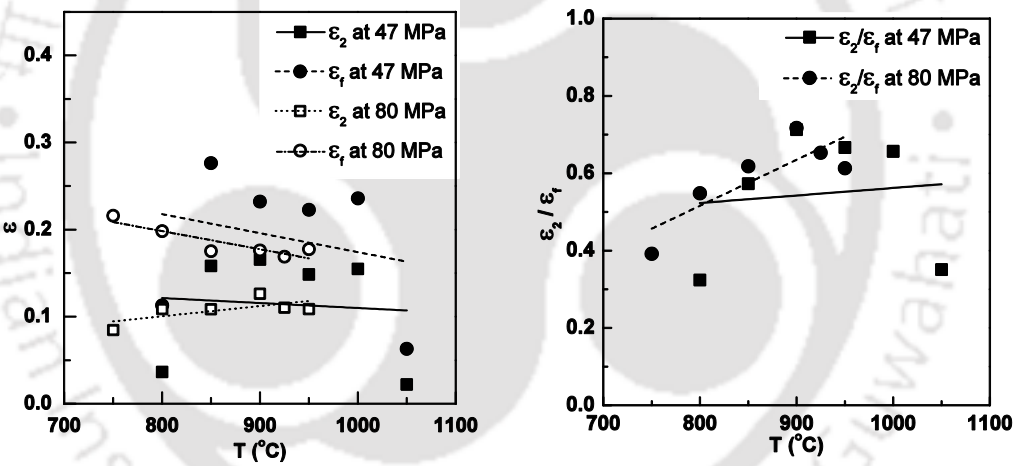

(a) (b)

Figure 4.26. (a) Strain to rupture and secondary strain and (b) relative secondary strain as a function of temperature at stresses of 47 MPa and 80 MPa.

Figure 4.27(a) shows the plot of ln(σ) vs. ln(t_r) at test temperatures of 800 °C, 850 °C and 900 °C. The figure indicates a decrease in rupture time as the applied stress is increased. The minimum rupture time of 19 second is obtained when tested at 900 °C/120 MPa and whereas the maximum time of 441728 second (122.7 hours) was obtained when tested at 800 °C/47 MPa. The variation of rupture time with temperature is shown in Figure 4.27(b). It is evident from the figure that the rupture time decreases with increase in temperature for all stresses. At a constant temperature, the rupture time increases with decrease in applied stress.

TH-1394_09610307

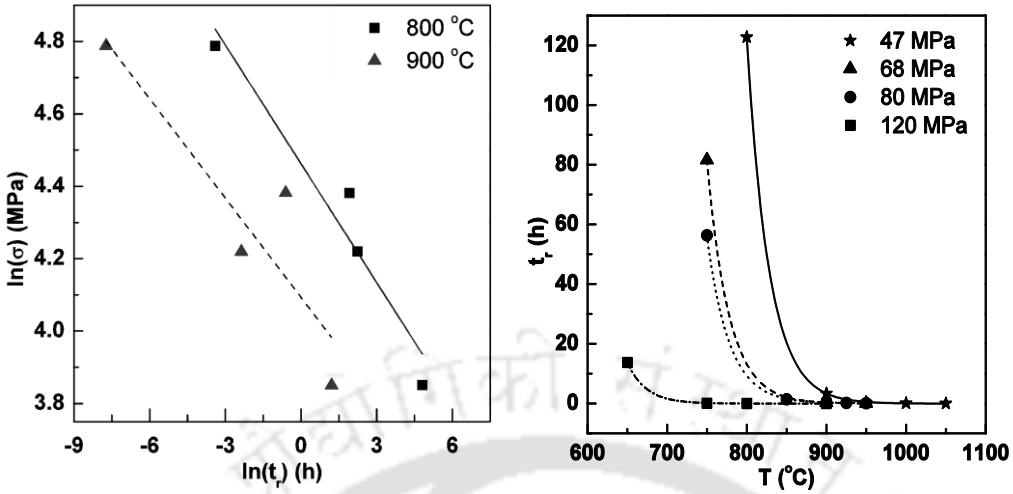

(a) (b)

Figure 4.27. Plot of (a) stress vs. rupture time, (b) rupture time vs. temperature for the steel.

Figure 4.28(a) & (b) shows the plot of $\dot{\varepsilon}_s$ vs. σ and T, respectively. It is observed that the $\dot{\varepsilon}_s$ increases with the increase in stress at a constant temperature. The value of $\dot{\varepsilon}_s$ is also increased with increase in T at a constant σ. At a stress of 47 MPa, the $\dot{\varepsilon}_s$ at 800 °C is two orders of magnitude higher that that at 900 °C, whereas it is only around one order magnitude higher when tested at 120 MPa.

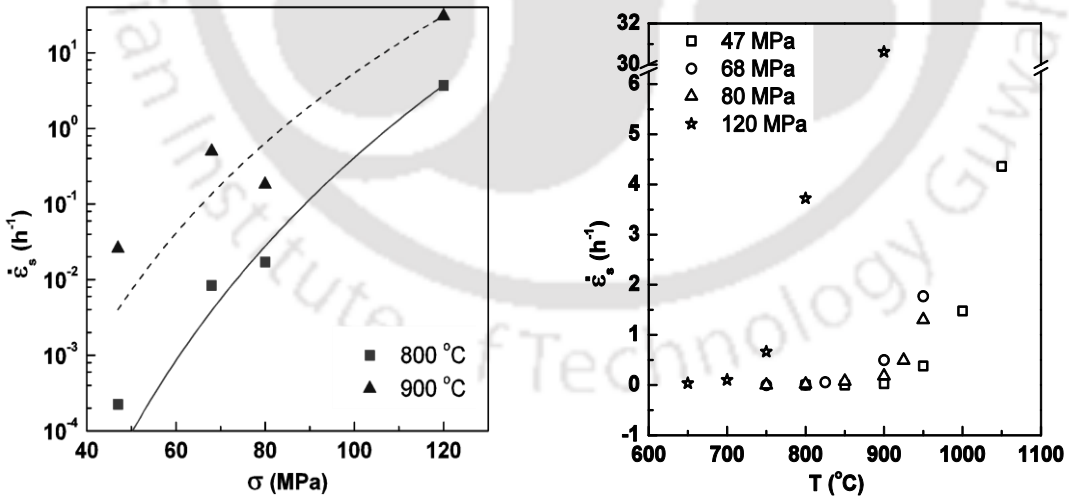

(a) (b)

Figure 4.28. Plot of minimum creep rate vs. (a) stress and (b) temperature for the steel.

4.3.4 Constitutive Modeling

As discussed in section 2.4, the creep constitutive equations relating to minimum creep rate $\dot{\varepsilon}_s$ with temperature T and stress σ can be expressed as any of the following:

TH-1394_09610307

$$\dot{\varepsilon}_s = A_1 \sigma^{n_c} \exp\left(-\frac{Q_{app}}{RT}\right) \quad (4.1)$$

$$\dot{\varepsilon}_s = A_2 \exp(\beta\sigma) \exp\left(-\frac{Q_{app}}{RT}\right) \quad (4.2)$$

$$\dot{\varepsilon}_s = A_3 [\sinh(\alpha\sigma)] \exp\left(-\frac{Q_{app}}{RT}\right) \quad (4.3)$$

where A_1, A_2, A_3 are pre-exponential factors n_c, β, α are constants, Q_{app} is the apparent activation energy for creep and R is the universal gas constant (= 8.314 J K^{-1} mol^{-1}) and T is the temperature in Kelvin. Pre-exponential factors, n_c, β and α are physical constants which can be determined from the creep test data. The constant n_c is also known as creep stress exponent. The observed activation energy for creep depends on the operating mechanism of creep. Depending on the combinations of stress and temperature, there may be different mechanisms operating which cannot be alienated out from the experimental data. Therefore, the activation energy obtained from experimental data is referred to as apparent activation energy for creep Q_{app}.

The stress exponent n_c for this steel is determined from the $\log(\dot{\varepsilon}_s)$ vs. $\log(\sigma)$ plot for different temperatures as shown in Figure 4.29(a). The slope of the linear fits for the plots yielded n_c values in the range from 2.6 to 16.8 with an average value of 8.9. The plot of n_c as a function of temperature is shown in Figure 4.29(b) indicates a non-linear relationship between n_c and T.

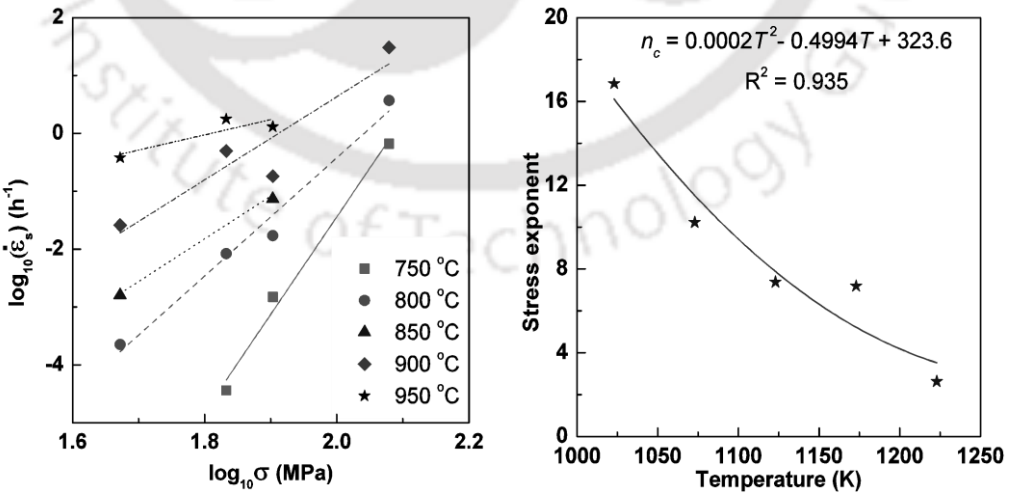

(a) (b)

Figure 4.29. (a) Determination of creep stress exponent n_c and (b) effect of T on n_c for the steel.

The value of n_c is related to T by a second order polynomial equation of the form

TH-1394_09610307

$$n_c = 0.0002T^2 - 0.4994T + 323.6 \quad (4.4)$$

where T is the test temperature expressed in Kelvin. The value for the stress exponent n_c is comparable to values reported in the literature for austenitic stainless steels [115, 237].

The threshold stress σ_{th} for a particular temperature was determined from the corresponding n_c value from the $(\dot{\varepsilon}_s)^{1/n_c}$ vs. σ plot as mentioned in section 3.4.1 where the linear intercept at which $\dot{\varepsilon}_s{}^{1/n_c} = 0$ is taken as σ_{th}. Modifying equation (Eq. 4.1) by incorporating the threshold stress into the analysis, the equation becomes

$$\dot{\varepsilon}_s = A_1(\sigma - \sigma_{th})^{n_c} exp\left(-\frac{Q_{app}}{RT}\right) \quad (4.5)$$

Table 4.5 gives the σ_{th} value with coefficient of determination R^2, for three different temperatures, obtained from Figure 4.30. Since, the threshold stress values are very small compared to the applied stress the σ_{th} in Eq. 4.5 is neglected for further analysis.

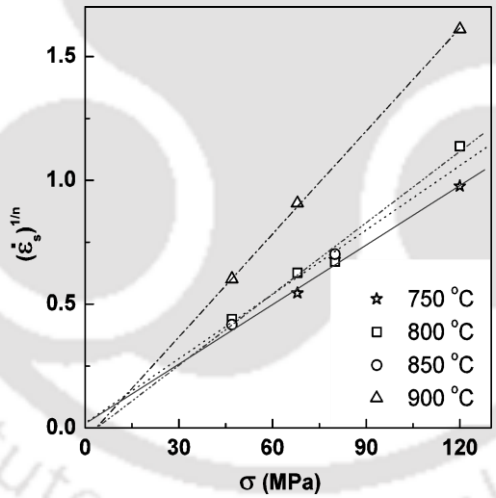

Figure 4.30. Determination of threshold stress for creep.

Table 4.5. Computed threshold stress for the creep test.

Temperature, T (°C)	Threshold stress, σ_{th} (MPa)	Coefficient of determination, R^2
800	0.0354	0.982
850	0.0123	0.985
900	0.0382	0.999

The apparent activation energy of the power-law creep equation was determined from plot of $\ln(\dot{\varepsilon}_s)$ vs. $1/T$ corresponding to each stress as shown in Figure 4.31(a). The

TH-1394_09610307

Q_{app} for the stresses 120 MPa, 80 MPa, 68 MPa and 47 MPa are 252.4 kJ/mol, 335.4 kJ/mol, 409 kJ/mol and 492.1 kJ/mol respectively, with an average value of 372.2 kJ/mol. The plot of Q_{app} as a function of σ shown in Figure 4.31(b) indicates a non-linear relationship between Q_{app} and σ. An empirical relation between Q_{app} and stress obtained by a polynomial fit is of the form:

$$Q_{app} = 0.0285\sigma^2 - 8.1146\sigma + 814.26 \tag{4.6}$$

where Q_{app} is the apparent activation energy in kJ/mol and σ is the applied stress in MPa.

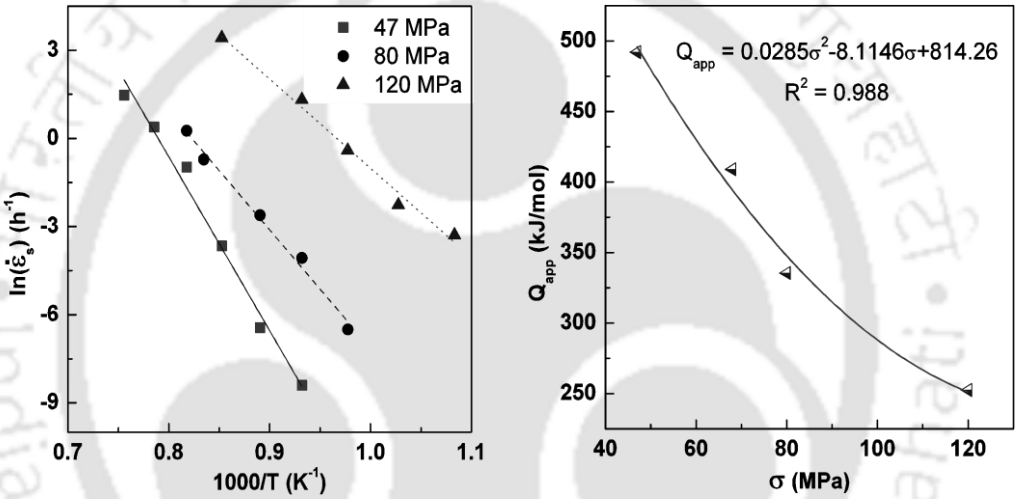

(a) (b)

Figure 4.31. (a) Determination of apparent activation energy Q_{app} and (b) effect of σ on Q_{app}.

Large scatter in the creep data is observed due to nonlinear behavior of the creep deformation. Since, n_c is a function of temperature and Q_{app} is a function of stress, a precise determination of constant A_1 is difficult. A least squares fit technique was used for determining the creep constitute parameters. The constitutive parameters obtained by the least squares fit are shown in Table 4.6 for Eq. 4.1 to 4.3.

Table 4.6. Creep constitutive parameters of Eq. 4.1, 4.2 and 4.3 and correlation coefficients.

Eq. 4.1	A_1	Q_{app} (kJ/mol)	n_c	R^2
	9.42×10^{-6}	321.67	8.3	0.98
Eq. 4.2	A_2	Q_{app} (kJ/mol)	β	R^2
	5.66×10^{5}	295.7	0.1038	0.95
Eq. 4.3	A_3	Q_{app} (kJ/mol)	α	R^2
	8.53×10^{5}	290.04	0.1174	0.77

TH-1394_09610307

Based on the data shown in Table 4.6, the following constitutive relationships are obtained for the $\dot{\varepsilon}_s$:

$$\dot{\varepsilon}_s = 9.42 \times 10^{-6}\sigma^{8.3}\exp\left(-\frac{312670}{RT}\right) \quad (4.7)$$

$$\dot{\varepsilon}_s = 5.66 \times 10^{5}\exp(0.1038\,\sigma)\exp\left(-\frac{295700}{RT}\right) \quad (4.8)$$

$$\dot{\varepsilon}_s = 8.53 \times 10^{5}[\sinh(0.1174\,\sigma)]\exp\left(-\frac{290040}{RT}\right) \quad (4.9)$$

From the value of coefficient of determination R^2 shown in Table 4.6, the best creep constitutive equation is the power law equation (Eq. 4.7).

Figure 4.32(a) shows the plot of $\dot{\varepsilon}_s$ vs. $1/T$ obtained experimentally and using Eq. 4.7 for different stresses. The plot of $\dot{\varepsilon}_s$ vs. σ obtained experimentally and using Eq. 4.7 for different temperatures are shown in Figure 4.32(b). In terms of the trend in variation of $\dot{\varepsilon}_s$ with $1/T$ (or σ), both figures show that there is a good agreement between calculated values and the experimental data. A variation of one order of magnitude in the value of $\dot{\varepsilon}_s$ between experimentally obtained value of $\dot{\varepsilon}_s$ and that obtained by constitutive equation is generally accepted for modeling of creep deformation [116]. Hence, the constitutive relationship obtained by Eq. 4.7 is acceptable for the creep deformation of the investigated steel.

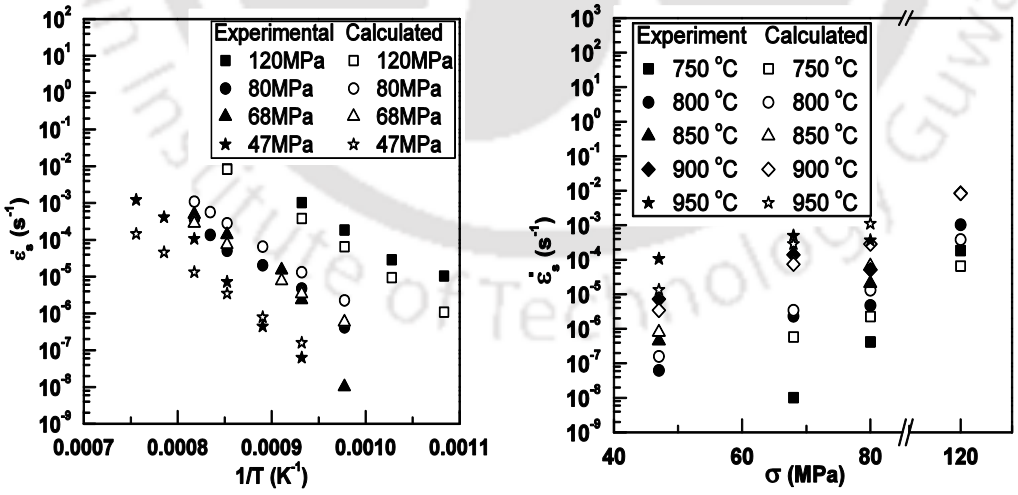

(a) (b)

Figure 4.32. Variation of experimental $\dot{\varepsilon}_s$ and calculated $\dot{\varepsilon}_s$ using Eq. 8 with (a) $1/T$ and (b) σ.

TH-1394_09610307

4.3.5 Creep Mechanism and Fractography

The longitudinal section of the specimen after creep failure was metallographically polished and observed under the optical microscope. Figure 4.33 and 4.34 show the micrographs of the specimen tested at 650 ˚C / 120 MPa and 900 ˚C / 68 MPa, respectively. Low magnification micrographs reveal presence of a large population of voids near the fracture surfaces. These voids are present at grain boundary region. Observation under high magnification reveals nucleation of voids at the carbide-matrix interface regions. The size and morphology of the voids indicate considerable growth after nucleation during deformation at high temperature. Since, the carbides are present at the grain boundary regions, the path of void growth is found to be along the grain boundaries.

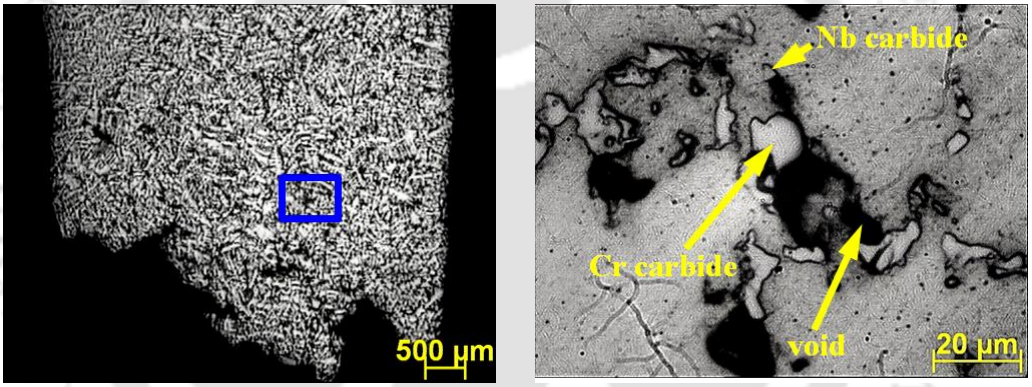

(a) (b)

Figure 4.33. (a) Low magnification and (b) selected area high magnification optical micrograph of longitudinal rupture section after creep test at 650 ˚C/120 MPa

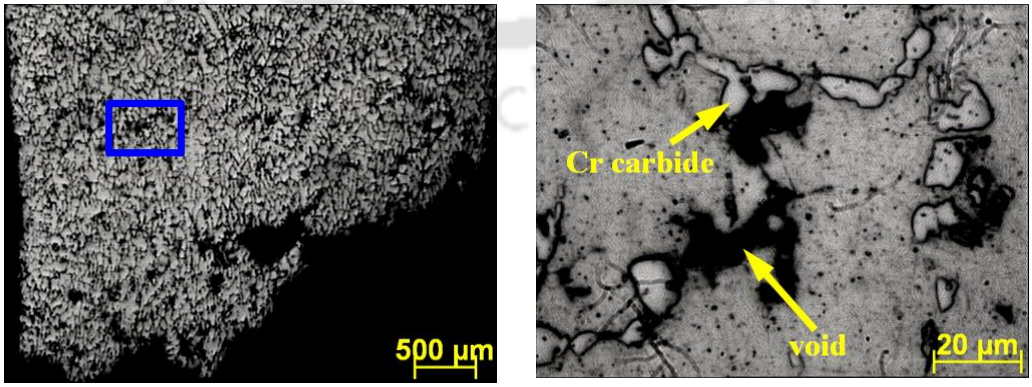

(a) (b)

Figure 4.34. (a) Low magnification and (b) selected area high magnification optical micrograph of longitudinal rupture section after creep test at 900 ˚C/68 MPa.

Similar features are observed (Figure 4.35) when specimen tested at 850 ˚C / 47 MPa and studied using SEM. The SEM micrographs reveal the size of the voids away from the fracture surface as around 3-8 μm. The features reveal the failure mechanism by nucleation of voids in the vicinity of carbides, its subsequent growth along the grain boundaries and coalescence resulting in the final failure.

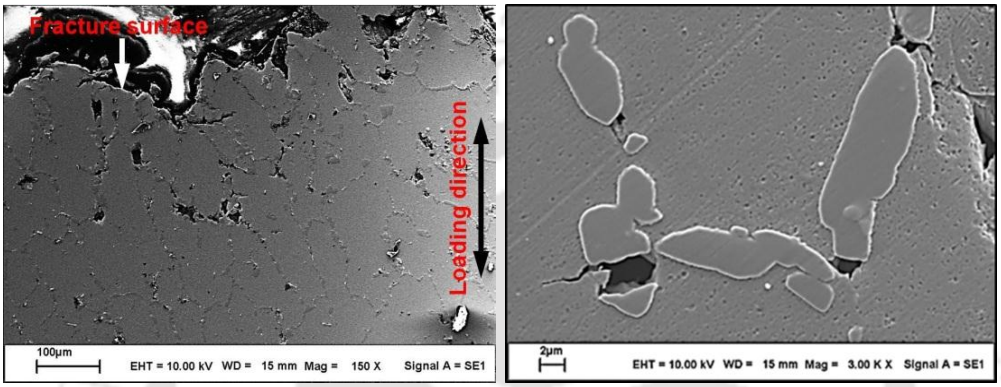

(a) (b)

Figure 4.35. SEM images at (a) low and (b) higher magnification of cracks along the longitudinal section after fracture at 850 ˚C/47 MPa.

Figure 4.36 shows the images of x-ray elemental mapping for Fe, Cr, Ni, Nb, Si and Ti at regions near to the fracture surface of creep tested specimen. The figures reveal nucleation of micro-voids in the vicinity of Cr-rich carbides.

Figure 4.37(a) & (b) show the SEM images of the fractured surface of the specimen tested at 650 °C/120 MPa. Image obtained at low magnification (Figure 4.37(a)) reveals fracture surface of specimen failed at ductile mode of failure. High magnification image reveals dimple features along with interface micro cracks at the particle matrix interface regions. At some regions cleavage features are also observed. Fractographs of specimen tested at 900 °C/120 MPa shown in Figure 4.38 (a) & (b) reveal the failure of the sample in fully ductile manner. Almost the entire surface shows dimple feature characteristics of micro void nucleation and coalescence.

.

TH-1394_09610307

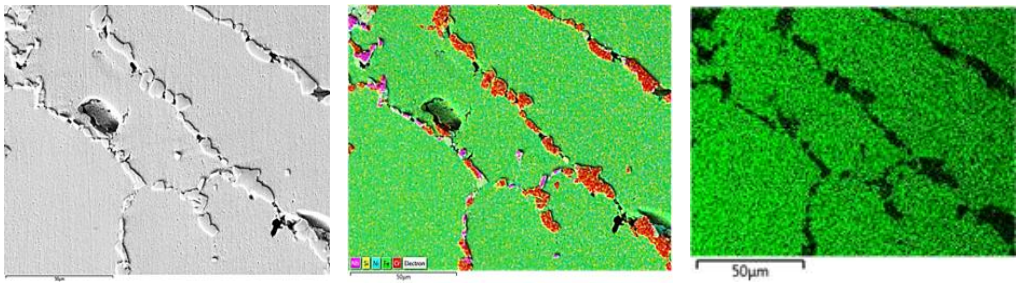

Iron

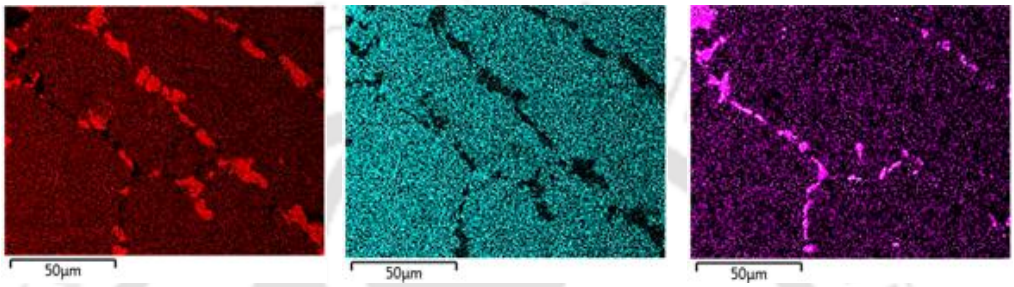

Chromium Nickel Niobium

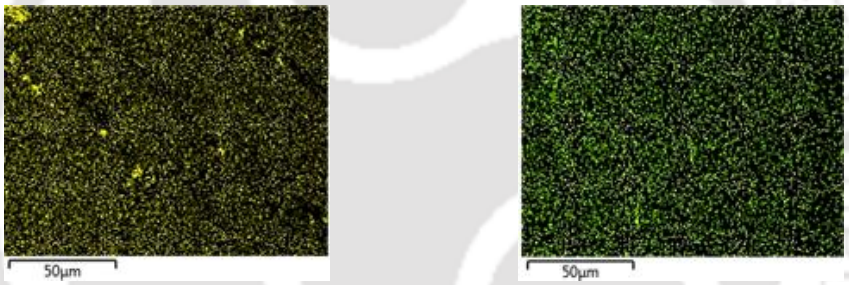

Silicon Titanium

Figure 4.36. X-ray elemental mapping (Fe, Cr, Ni, Nb, Si and Ti) on creep tested specimen at 650 ˚C/120 MPa.

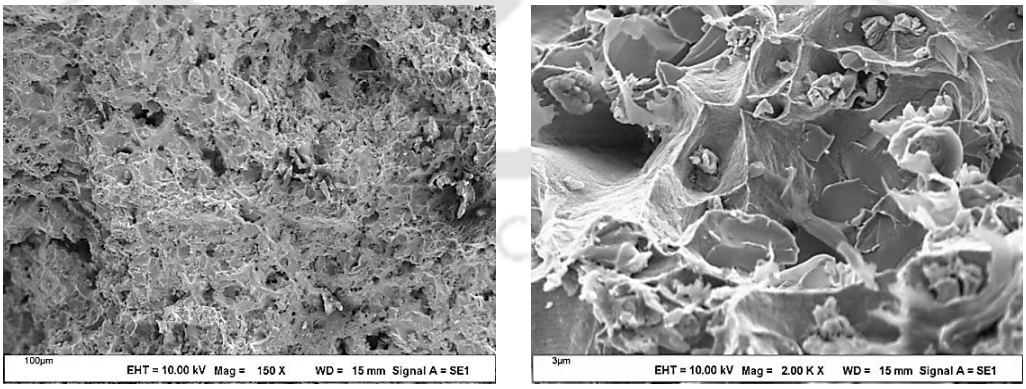

(a) (b)

Figure 4.37. (a) Low magnification and (b) high magnification fractographs of creep tested samples at 650 °C/120 MPa.

TH-1394_09610307

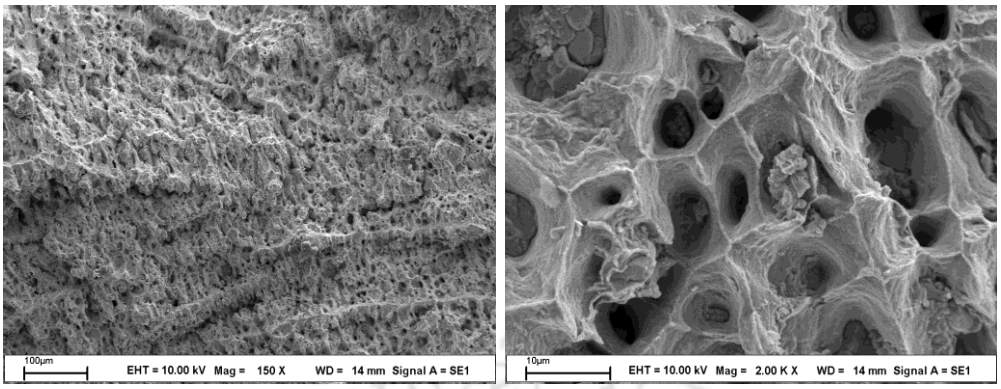

(a) (b)

Figure 4.38. (a) Low magnification and (b) high magnification fractographs of creep tested samples at 900 °C/120 MPa.

4.3.6 Monkman-Grant Relationships

The Monkman-Grant and modified Monkman-Grant relationships (Eq. 2.6 and Eq. 2.7, respectively) are useful in determining the creep rupture time of the material. Detailed description regarding these relationships is highlighted in section 2.8. Figure 4.39(a) shows the plot of rupture time t_r vs. $\dot{\varepsilon}_s$ for all the tests carried out at different temperatures and stresses. Figure also shows a straight line fit with coefficient of determination, R^2 =0.97. From the figure, the value of Monkman-Grant exponent *m* and constant *C* in Eq. 2.7 are 0.99 and 0.096, respectively. Since it is reasonable to assume a value of *m* as unity, Eq. 2.7 can be written in the form

$$\dot{\varepsilon}_s . t_r = C_{MG} = 0.096 \tag{4.10}$$

Figure 4.39(a) indicates that rupture time t_r is inversely proportional to the minimum creep rate and the Monkman-Grant relationship can be used for predicting the rupture time of the investigated steel.

Figure 4.39(b) shows the plot of ε_f/t_r vs. $\dot{\varepsilon}_s$ for the material. The plot shows a straight line fit with a coefficient of determination R^2 = 0.98. From the figure, the values for *m'* and *C'* in the modified Monkman-Grant relationship (Eq. 2.8) are found to be 1.06 and 0.254, respectively. Approximating the value of *m'* equal to unity, the modified Monkman-Grant expression can be obtained as

$$\dot{\varepsilon}_s . \frac{t_r}{\varepsilon_f} = 0.254 \tag{4.11}$$

This indicates that the ε_f/t_r is directly proportional to the minimum creep rate. *i.e.* the modified Monkman-Grant relationship expressed in the above form can be used for

TH-1394_09610307

predicting the rupture time from the minimum creep rate and fracture strain of the of the investigated steel with reasonable accuracy. From the values of coefficient of determination for the Eq. 4.10 and Eq. 4.11, one can conclude that both Monkman-Grant and modified Monkman-Grant relationships can be successfully used to correlate the rupture time and steady state creep rate for the investigated steel.

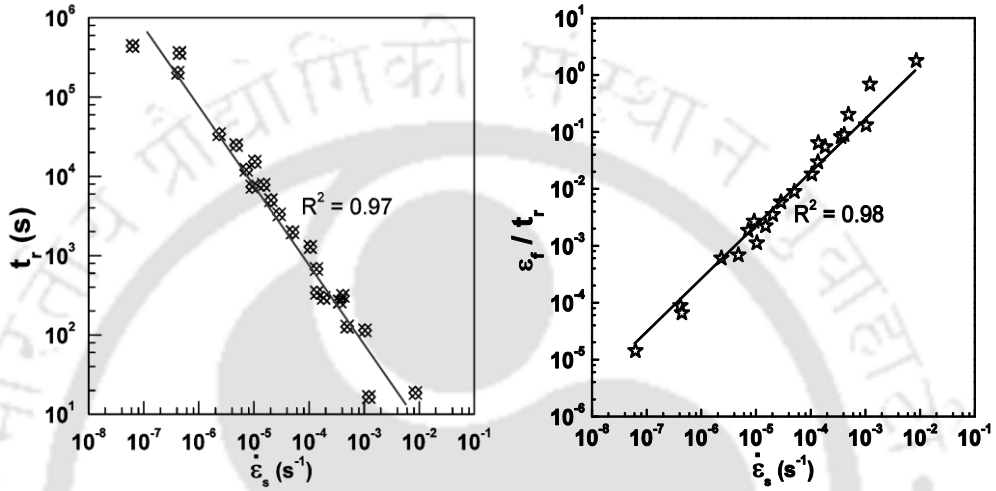

(a) (b)

Figure 4.39. Variation of (a) rupture time with $\dot{\varepsilon}_s$ and (b) ε_f/t_r with $\dot{\varepsilon}_s$.

In line with the MMGR, Choudhary et al. (2010) [162] proposed relationships correlating $\dot{\varepsilon}_s$, with time for onset of secondary creep, t_{os} and time for onset of tertiary creep t_t. Time t_{os} can be obtained using the relationship

$$\dot{\varepsilon}_s{}^a . \frac{t_{os}}{\varepsilon_1} = K_1 \tag{4.12}$$

where a and K_1 are constants. A logarithmic plot of t_{os}/ε_1 vs. $\dot{\varepsilon}_s$ obtained using the creep data is shown in Figure 4.40(a). From the straight line fit the values for a and K_1 are determined as 0.998 and 0.65 respectively, with R^2 = 0.992. In the present case, assuming a =1, Eq. 4.12 can be expressed as

$$\dot{\varepsilon}_s \frac{t_{os}}{\varepsilon_1} = 0.65 \tag{4.13}$$

Following similar procedure [Choudhary et al. (2010) [162]], the time for onset of tertiary creep, t_{ot} can be obtained by the relationship

$$\dot{\varepsilon}_s{}^b . \frac{t_{ot}}{\varepsilon_3} = K_1{}' \tag{4.14}$$

TH-1394_09610307

where b and K_1' are constants. From a logarithmic plot of t_t/ε_3 vs. $\dot{\varepsilon}_s$ shown in Figure 4.40(b), b and K_1' were determined to be 0.997 and 0.82, respectively. Assuming b = 1, Eq. 4.14 can be written in the form

$$\dot{\varepsilon}_s . \frac{t_{ot}}{\varepsilon_3} = K_T' = 0.82 \tag{4.15}$$

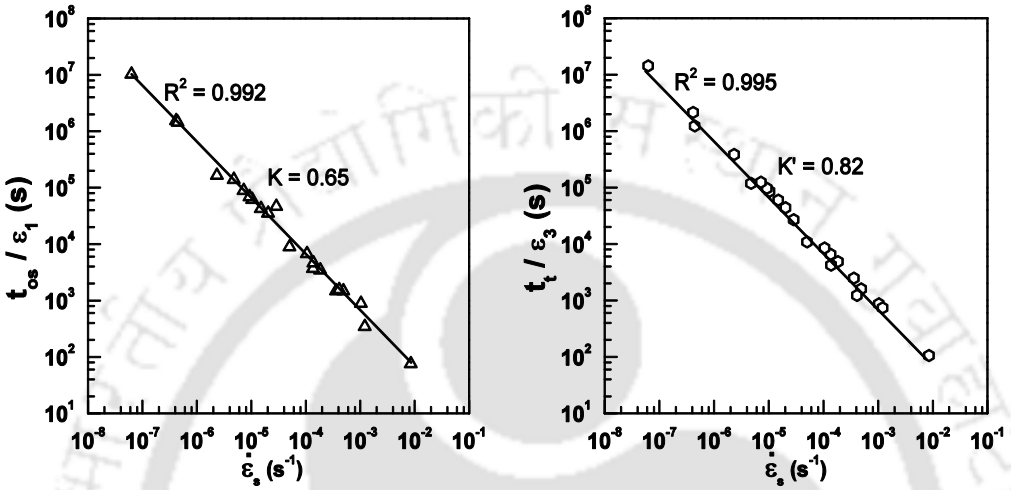

(a) (b)

Figure 4.40. Variation of (a) t_{os}/ε_1 with $\dot{\varepsilon}_s$ and (b) t_t/ε_3 with $\dot{\varepsilon}_s$.

It appears that the time spent in the tertiary region is some fraction of the total time of rupture. A plot of t_{ot} vs. t_r for all stress levels is shown in Figure 4.41. From the straight line fit an expression correlating the t_{ot} and t_r is obtained as

$$t_{ot} = 0.668 . t_r \tag{4.16}$$

This indicates that only 33.2 % of the total rupture time is spent for the tertiary creep strain.

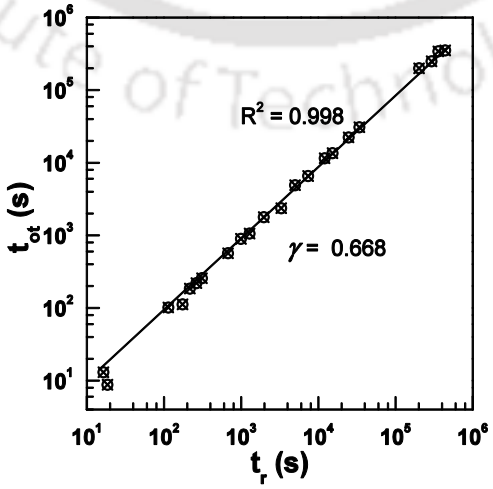

Figure 4.41. Plot of time to onset of tertiary creep vs. rupture time.

TH-1394_09610307

To investigate whether the time spent in tertiary creep is dependent on the stress level, analysis was carried out for two stress ranges: lower stress in the range 47 MPa to 68 MPa and higher stress in the range 80 MPa to 120 MPa.

For stresses in the range 47-68 MPa, the expression obtained as

$$t_{ot} = 0.814\, t_r \tag{4.17}$$

and for stresses in the range 80-120 MPa, the expression obtained as

$$t_{ot} = 0.53\, t_r \tag{4.18}$$

Eq. 4.17 reveals that, the time spent in tertiary creep is around 18.6 % of the total rupture time for low stress levels, whereas, from Eq. 4.18, it is found that higher time (around 47 %) is spent for the tertiary creep region at higher stresses.

4.3.7 Creep Damage Tolerance Factor

Components used at elevated temperature are designed for a particular allowable stress based on the stress necessary to achieve a certain strain in a given time. In this approach the creep ductility is not considered while arriving at the allowable stress. The Monkman-Grant relationship is based on the fact that creep deformation and damage are interrelated. In materials where the creep damage is by growth of the cavities and the creep fracture is strain controlled, the creep damage grows along with the creep curve. The cavity attains a critical size at t_{MGD}, as shown in Figure 3.12. As per the continuum damage mechanics (CMD), the critical damage criterion is defined and can be arrived by Eq. 2.11.

A double logarithmic plot of average creep rate vs. minimum creep rate [(ε_f/t_r) vs. $\dot{\varepsilon}_s$] from the entire the creep test data is shown in Figure 4.42. From the plot, the value for λ in Eq. 2.11 is found to be 1.53. It may also be noted that the value of λ in the stress range 47-68 MPa and 80-120 MPa are 1.29 and 2.54 respectively. This is in agreement with the trend reported for different steels [162-170]. In few cases, the high reported values for λ are due to the lower test temperatures compared to the present work. A strong dependency of damage tolerance factor λ, with stress has been reported, based on experiments using foil specimen [165]. However in bulk samples, λ is in the range 1.5 to 10 [170] where higher values are for lower stress conditions. Nucleation of micro cracks and cavities during creep generally occur towards the end of the secondary

TH-1394_09610307

creep region. Presence of these defects at the grain boundary region plays an important role in the deformation during the tertiary creep.

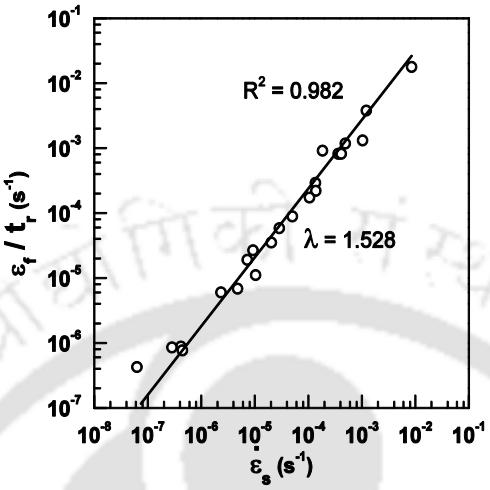

Figure 4.42. Variation of average creep rate with minimum strain rate.

Low values of λ between 1.5 to 2.5 are attributed to creep damage due to growth of cavities by diffusion in the power law creep region [165, 238]. Singh and Kamaraj (2009, 2010) analyzed creep ductility λ for rotor steel and observed λ was governed by the type of voids which nucleate and grow along grain boundaries till failure of the material [239, 240]. However, the acceleration of creep damage due to degradation of microstructure by coarsening of particles and substructure results in higher values of λ. Micrograph of creep rupture specimen and the value of $\lambda < 1.53$ suggests that the tertiary creep is caused by nucleation and growth of inter-granular cavities.

Figure 4.43 illustrates the t_{MGD} vs. t_r plot for the investigated steel. For the entire set of experiments the value of f_{CDM} of Eq. 2.12 is determined as 0.804. However, the values of f_{CDM} for stresses in the range 47-68 MPa and 80-120 MPa are found to be 0.927 and 0.684, respectively. It is also to be noted that the value of f_{CDM} evaluated using Eq. 2.12 for $\lambda = 1.53$ for the present steel is 0.8025, which almost equal to value obtained from Figure 4.43. This indicates that the f_{CDM} obtained by Monkman-Grant ductility relationship is in good agreement with that obtained by CDM technique.

TH-1394_09610307

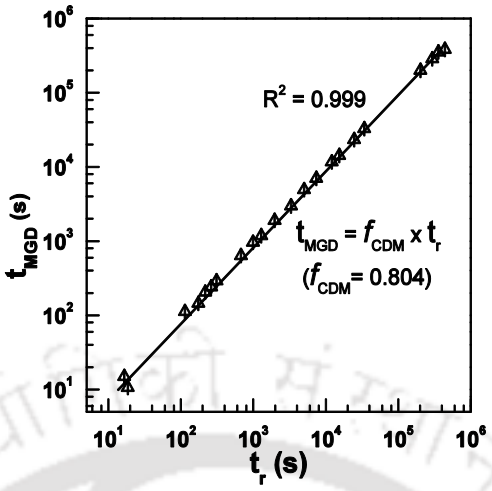

Figure 4.43. Variation of time to reach MGD with rupture time.

In conclusion, the creep curve can be divided into two regions. The first region is a safe region which is up to the point of t_{MGD}. In this region, creep damage is a slow process and almost at a uniform rate. The second region, lying in the range t_{MGD} to t_r is considered to be unsafe due to localized creep damage resulting in acceleration of the creep process. A transition exists between these two regions [241] during which the cavity size reaches a critical value resulting in accelerated creep rate. f_{CDM} quantifies the degradation of the material during service and can be used as a creep design criterion [242, 243] for engineering components. From the present investigation, the value of f_{CDM} equal to 0.804 can be used as a factor of safety in creep design for the steel.

4.4 Artificial Neural Network Modeling of Creep Curve

Modeling of creep curve was carried out by predicting the time dependent creep strain ε by artificial neural network (ANN) technique. The modeling was based on the concept

$$\varepsilon = f(\sigma, T, t) \tag{4.19}$$

where, σ is the applied stress, T the temperature and t the time.

Creep curve at any temperature and stress was predicted by ANN using the limited experimental data. The methodology followed for the ANN modeling is presented in section 3.4.3. The ANN architecture in the present study consists of an input layer, one hidden layer and an output layer. The input layer consists of three neurons, each representing σ, T and t. The output layer consists of one neuron

TH-1394_09610307

representing ε. The intermediate hidden layer consists of N neurons. With this architecture, the network is trained by providing data in the form of several input and output pairs. During the training process, the network adjusts its weights to minimize the error between the predicted and actual outputs. To ensure proper weights and bias during the training process, the model was simultaneously tested with a set of testing data. The network is said to over-fit the data when the testing error is much higher than the training error. When the training and testing errors are almost equal the network is considered to be properly fitted. The values of σ, T and t were transformed to lie within the range of 0.1 and 0.9 before feeding the data in to the network. Training was carried out using the *trainlm* training function of MATLAB® software. For the network training, a number of numerical experiments were carried out with single hidden layer neural network using *tansig, logsig, hardlim* and *purelin* transfer functions with varying number of neurons in the hidden layer. During the numerical trail experiments, the best neural network architecture was frozen based on (i) functional RMS error during training and testing which should be minimum (ii) 98 % of the data which could be predicted within a deviation error of ± 20 % and (iii) atleast 95 % of the data which could be predicted within a deviation error of ± 15 %. From the numerical experiments, the best network architecture and processing function was arrived at.

After a number of numerical experiments, the final architecture was arrived with single hidden layer with j = 15 neurons as shown in Figure 3.13. The transfer function at the input to hidden layer was *tansig* and at the output layer was *purelin* function. During the training with the 732 input-output data sets, the RMS error was 0.0064 with a maximum deviation error of 33.6 %. The corresponding errors during the testing with 376 data sets were 0.006 and 31.9 %, respectively.

Figure 4.44(a) & (b) show the plots of neural network predicted vs. experimental value of creep strain during training and testing, respectively. A diagonal line inclined at 45^{o} from horizontal is shown in both the figures. The plot (Figure 4.4(a)) shows most of the data points during training lie very close to the inclined line indicating good prediction. 92.8 % and 97.3 % data points lies within a deviation error of ± 10 % and ± 15 %, respectively during the training. The correlation coefficient R_{cc} and average absolute relative error (AARE) for the training data set are 0.994 and 0.18 %, respectively. As shown in Figure 4.44(b), during the testing, 90.2 % and 96.8 % of the

TH-1394_09610307

data points could be predicted within a deviation error of ± 10 % and ± 15 %, respectively. The R_{cc} value and AARE for the testing data set were determined as 0.995 and 0.09 %, respectively.

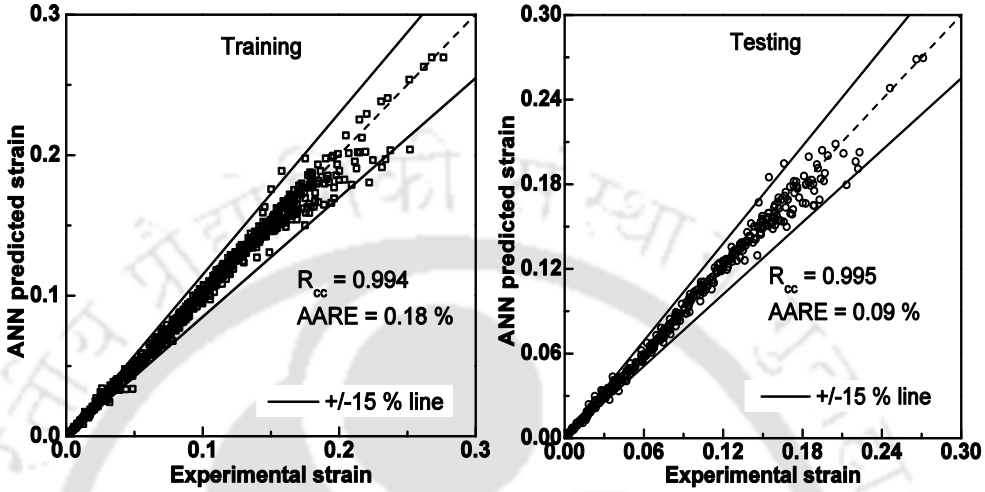

(a) (b)

Figure 4.44. Correlation between experimental and predicted creep strain data after (a) training and (b) testing of artificial neural network.

The frequency counts vs. relative error histogram plots are shown in Figure 4.45(a) & (b) for training and testing, respectively. The relative error of the ANN model shows a typical Gaussian distribution. It is observed that the relative error obtained from the ANN model vary from -30.7 % to 33.6 % and -22 % to 31.9 % for training and testing, respectively. Figure 4.45(a) & (b) show that 71.7 % training data sets and 66.8 % testing data sets of the relative error of ANN model are within ± 5 %.

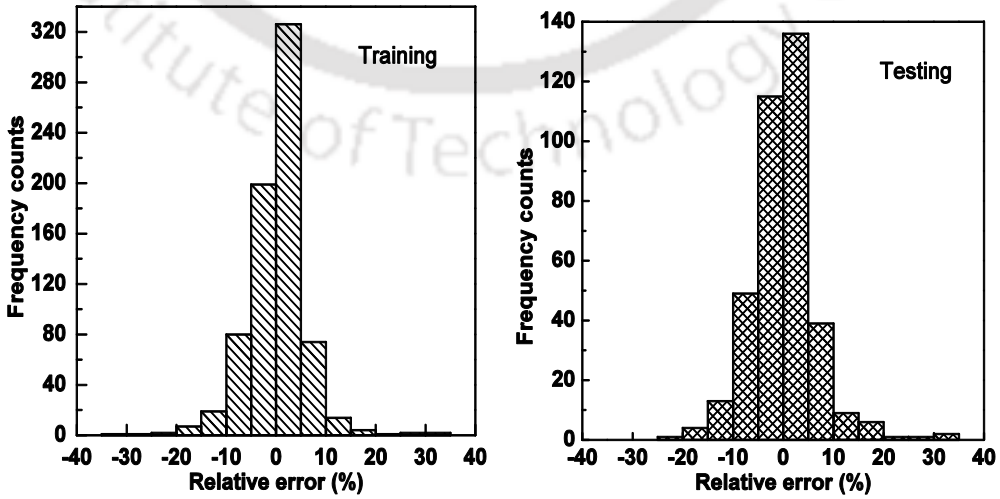

(a) (b)

Figure 4.45. Relative error between experimental and predicted creep strain data after (a) training and (b) testing of artificial neural network.

TH-1394_09610307

Figure 4.46(a) & (b) show the distribution of the residual values about zero mean for training and testing, respectively. The randomized distribution of residual values about zero mean signifies that no systematic error exists in the development of the of the ANN model. The propagation of the residuals on both sides of zero indicates that the developed model is unbiased and the predictive capability of the ANN model is good. The main source of prediction error may be due to noise in the experimental data which cannot be wholly attributed to the predictability of the neural network model.

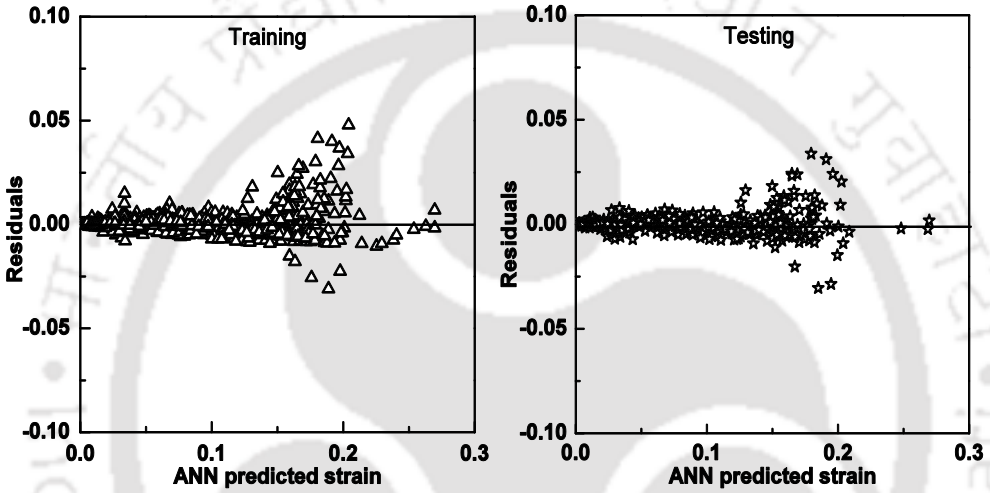

(a) (b)

Figure 4.46. Plot between residuals and predicted values after (a) training and (b) testing of artificial neural network.

.

The relative importance of the each input variable on output was quantified using Eq. 3.13. The importance of the input variables given by weights method proposed by Garson [232] is shown in Figure 4.47. The contribution of the input variable is in the range from 22 % to 52 %. The figure shows that among the three input variables, applied stress has higher dependency on creep strain, followed by temperature.

The fitted neural network model was validated independently for 154 data sets which were not used earlier for the purpose of training or testing. Figure 4.48(a) shows the plot of neural network predicted and experimental value of strains.151 out of 154 data (i.e. 98%) could be predicted within a deviation error of ± 10 % during validation. The RMS error, correlation coefficient R_{cc} and AARE for the validation data set are 0.0062, 0.992 and -0.91 %, respectively. Figure 4.48(b) shows the plot of frequency counts vs. relative error histogram for validation. It is observed that the maximum

TH-1394_09610307

relative error during validation is 18.9 %. Figure 4.48(b) indicates that 79.2 % and 98 % of the predicted strains are within ± 5 % and ± 10 %, respectively.

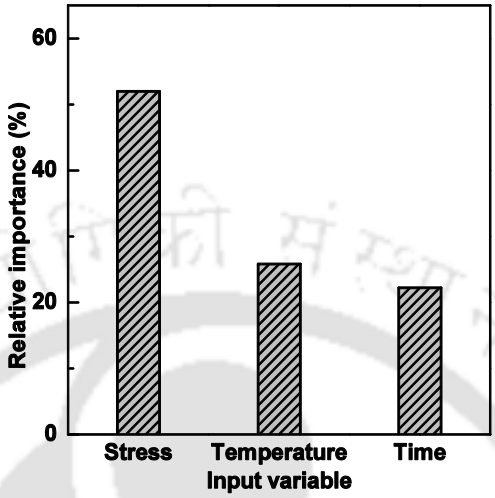

Figure 4.47. Relative importance of each input variable to simulate artificial neural network of creep curve based on Garson's algorithm.

Figure 4.48(c) shows the uniform distribution of the residual values about zero mean for validation. The prediction using the 154 independent data sets establishes the confidence in the predictive capabilities of the neural network model.

Having gained confidence in the neural network architecture, creep curves were obtained by ANN simulation under the 22 experimental conditions of stress and temperature. The simulations were carried out up to the rupture time obtained from the experiments. Figure 4.49 shows the comparison of the ANN simulated and experimental creep curves for six conditions of stress and temperature. In the figure, the continuous lines represent the simulated curves. Plots for the remaining 16 experimental conditions are shown in Appendix-VIII. The predictions are found to be very good.

TH-1394_09610307

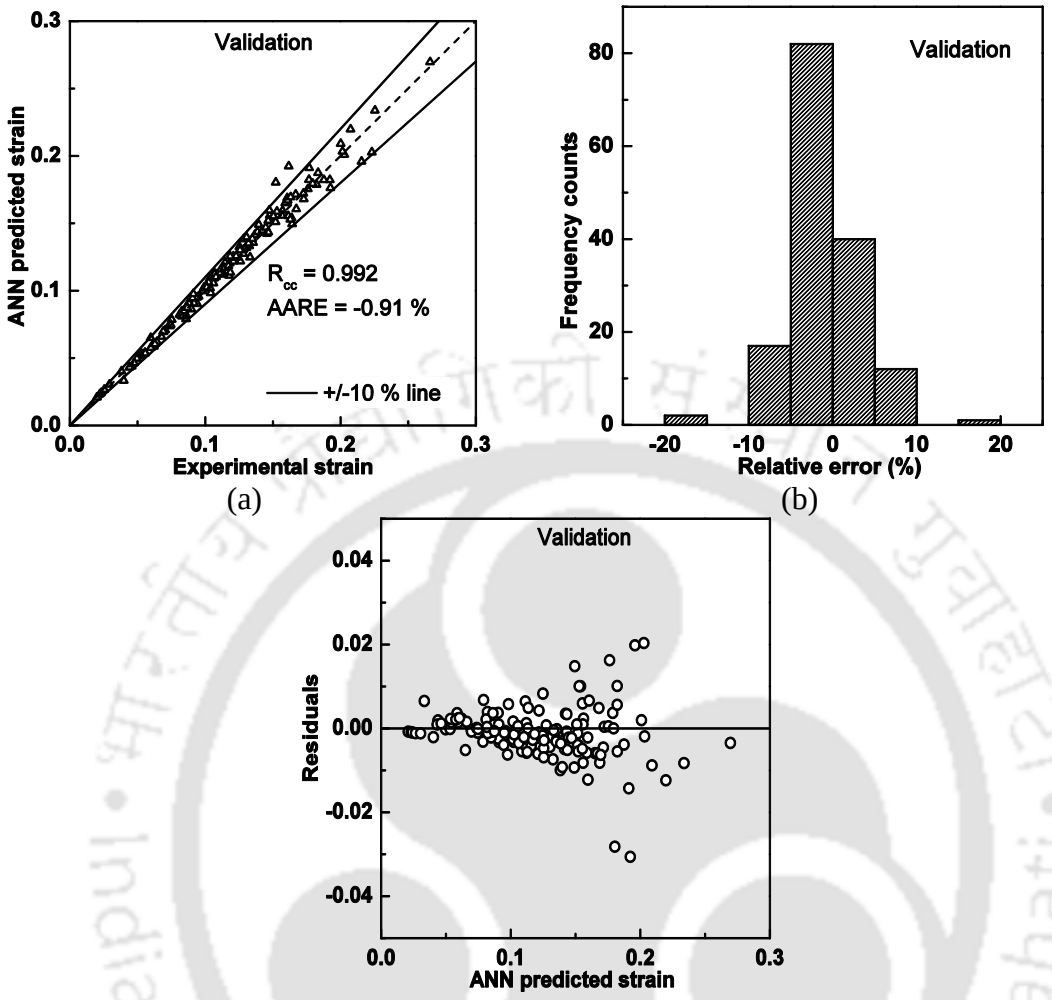

Figure 4.48. (a) Correlation, (b) relative error between experimental and predicted strain data and (c) plot between residuals and predicted values after validation.

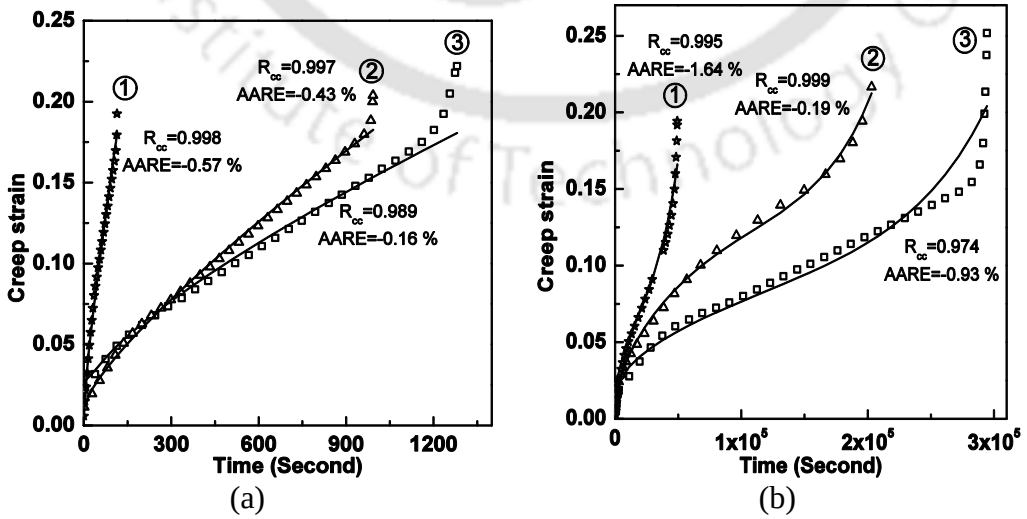

Figure 4.49. Comparison between experimental and predicted creep curves. Creep curves at (a) (1) 800 °C/120 MPa, (2) 900 °C/68 MPa, (3) 950 °C/47 MPa and (b) (1) 650 °C/120 MPa, (2) 750 °C/80 MPa, (3) 750 °C/68 MPa.

Simulation of creep curves were also carried out under various combinations of stresses and temperatures other than the experimental conditions. Figure 4.50(a) & (b) show the plot of the simulated creep curves up to a strain of 0.3.

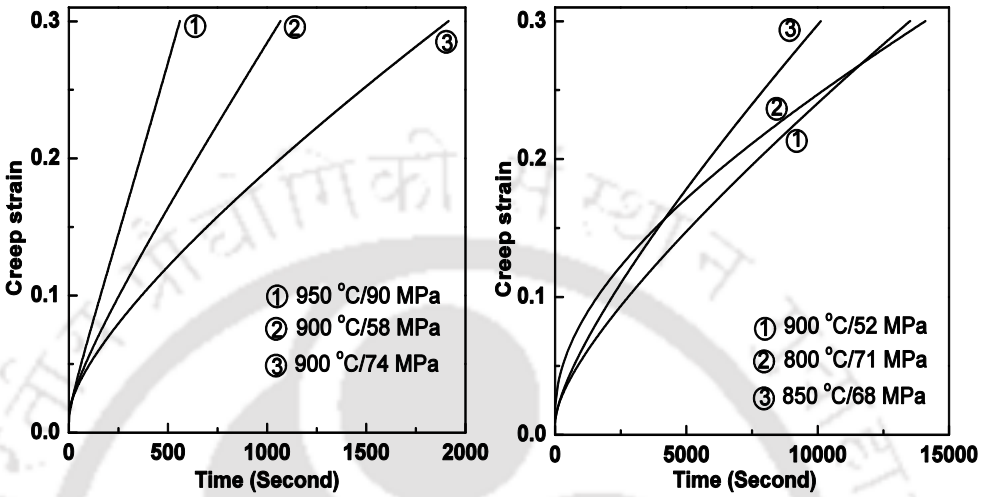

(a) (b)

Figure 4.50. Predicted creep curves at various stresses and temperatures.

For validating the authenticity of the simulated creep curves, one creep test was carried out at 68 MPa / 850 ˚C up to 20000 seconds. During the experiment the time to rupture was found to be 7337 seconds. Figure 4.51 shows the plots of the ANN simulated creep curve and the experimentally obtained creep curve for time up to 7337 seconds. The experimental result shows that the creep curve enters the tertiary stage just before rupture, whereas this was not reflected in the simulated creep curve. It is also evident that the deviation between ANN predicted and experimental strain in the tertiary creep region is high. The creep deformation in the tertiary region is not of much importance from the point of view of industrial safety since the maximum design creep life is at the onset of tertiary creep. Literature indicates that the strain to failure in metallic materials undergoing creep deformation is generally in the range 0.15-0.20. [244, 245], though few cases are reported with strains of around 0.3 [164, 246]. From the curves shown in Figure 4.51, the correlation coefficient R_{cc} and AARE between experimental and predicted strain values are found to be 0.994 and 23 %, respectively, indicating good prediction of the creep curve up to a strain of 0.2. It can be concluded that ANN modeling can be used as a powerful tool for prediction of creep curves using data obtained from limited experiments.

TH-1394_09610307

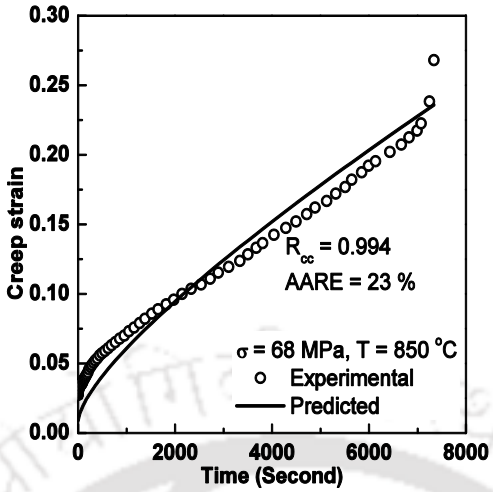

Figure 4.51. Comparison between experimental and predicted creep curve at 850 ˚C/68 MPa.

4.4.1 Comparison of Minimum Creep Rate

The minimum creep rate $\dot{\varepsilon}_s$ during creep deformation for various combinations of stress and temperatures are determined from (i) the creep experiments, (ii) power law constitutive equation (Eq. 4.8) and (iii) ANN predicted creep curves. The $\dot{\varepsilon}_s$ vs. $1/T$ plot obtained by the above three methods are shown in Figure 4.52(a). Plot of $\dot{\varepsilon}_s$ vs. σ obtained by these methods are shown in Figure 4.52(b). The plots indicate that the strain rate predicted by the constitutive model (Eq. 4.8) deviates by one to two orders of magnitude compared to the experimental value whereas the ANN predicted $\dot{\varepsilon}_s$ values are comparable to that of the experimental values. Table 4.14 compares the values of $\dot{\varepsilon}_s$ obtained by the three methods. The data indicates that the ANN predicted $\dot{\varepsilon}_s$ are close to the experimental values with reasonable accuracy.

Table 4.7 summarizes the predictability of minimum strain rate values obtained from power law equation (Eq. 4.8) and ANN predicted creep curve. Minimum strain rate values determined from ANN predicted creep curve show closer values than the $\dot{\varepsilon}_s$ values calculated using power law constitutive equation.

From the above analysis it can be concluded that ANN model is a powerful tool for prediction of $\dot{\varepsilon}_s$ within the domain of experimental conditions of temperature and stresses compared to the constitutive model.

TH-1394_09610307

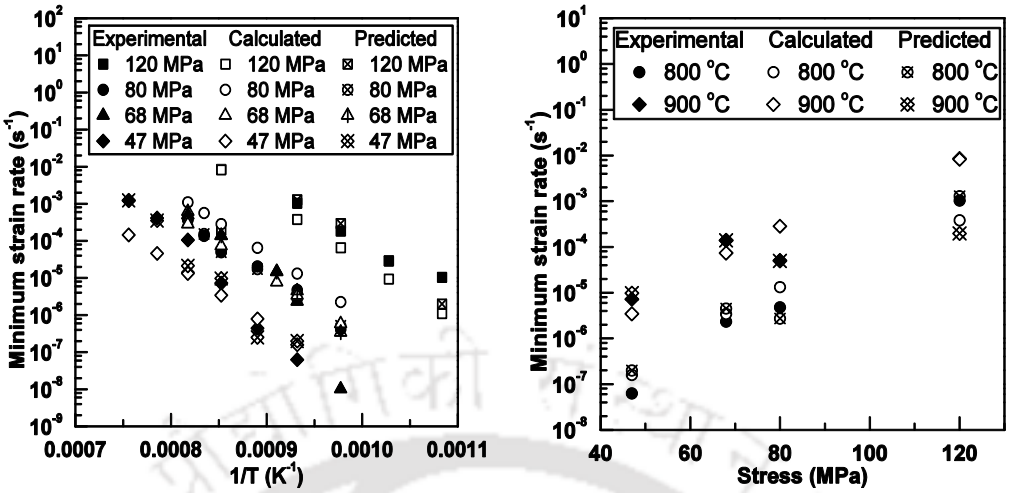

(a) (b)

Figure 4.52. Comparison of experimental, calculated using power law and ANN predicted $\dot{\varepsilon}_s$ with (a) $1/T$ for constant stresses and (b) σ for constant T.

Table 4.7. Comparison of the minimum strain rate obtained from the experimental, calculated using Eq. 4.8 and predicted by ANN technique.

Stress (MPa)	Temperature (°C)	Minimum strain rate (s^{-1})		
		Experimental	By constitutive model (Eq. 4.8)	ANN
120	800	1.03×10^{-3}	3.81×10^{-4}	1.28×10^{-3}
120	750	1.84×10^{-4}	6.54×10^{-5}	2.95×10^{-4}
120	700	2.88×10^{-5}	9.37×10^{-6}	2.89×10^{-5}
80	950	3.61×10^{-4}	1.09×10^{-3}	3.77×10^{-4}
80	925	1.37×10^{-4}	5.66×10^{-4}	1.53×10^{-4}
80	900	5.05×10^{-5}	2.84×10^{-4}	4.96×10^{-5}
68	950	4.92×10^{-4}	2.84×10^{-4}	6.14×10^{-4}
68	900	1.38×10^{-4}	7.37×10^{-5}	1.40×10^{-4}
68	825	1.50×10^{-5}	7.75×10^{-6}	1.45×10^{-5}
47	1050	1.21×10^{-3}	1.44×10^{-4}	1.24×10^{-3}
47	1000	4.11×10^{-4}	4.58×10^{-5}	3.52×10^{-4}
47	900	7.21×10^{-6}	3.43×10^{-6}	9.73×10^{-6}
68[@]	850	2.29×10^{-5}	1.70×10^{-5}	2.88×10^{-5}

[@] from the experiment carried out for the validation of the ANN technique and this data is not included for the development of constitutive parameters.

TH-1394_09610307

4.4.2 Creep Life Prediction by Parametric Techniques

In the parametric techniques, creep failure time of the material at particular service conditions of temperature and pressure is determined. The advantage of these techniques is that the long time life of the material can be predicted using data obtained from short time accelerated creep tests. In the present work, the data obtained from the accelerated creep test experiments is used to compare the creep life based on Manson-Haferd, Orr-Sherby-Dorn and Larson-Miller parametric techniques. For design purpose, only the creep life of the material up to the end of the secondary creep region is of importance, though designers considers the total rupture time. Creep curve data available from the literature indicates that most of the creep rupture occurs for strains less than 0.2. However, from the application point of view, a component can be considered as failed even if the creep strain is 0.15. In the present analysis, the creep life (rupture time) is taken as the time necessary to reach a creep strain of 0.15. The rupture time for a creep strain of 0.15 for various combinations of stress and temperatures were obtained by ANN simulated creep curve. The subsequent sub-sections discuss the creep life predicted by three parametric techniques.

4.4.2.1 Manson-Haferd Technique

For prediction of the creep life by Manson-Haferd parameter $P_{M\text{-}H}$, $\log_{10}(t_r)$ vs. T is plotted for different constant stresses. The Manson-Haferd constants, T_a and $\log_{10}(t_a)$ are determined from the intersection point of the extrapolated iso-stress lines. Using these constants, the σ vs. $P_{M\text{-}H}$ master plot is developed. The creep life of the material for a particular stress and temperature is obtained by extrapolation of the master curve.

Figure 4.53(a) shows the $\log_{10}(t_r)$ vs. T plot for the investigated steel at constant applied stresses. The value of Manson-Haferd constants, T_a and $\log_{10}(t_a)$ were determined to be 1520 K and -7.8, respectively. Figure 4.53(b) shows the Manson-Haferd master curve. The plot indicates a linear fit with the coefficient of determination R^2 equal to 0.978.

TH-1394_09610307

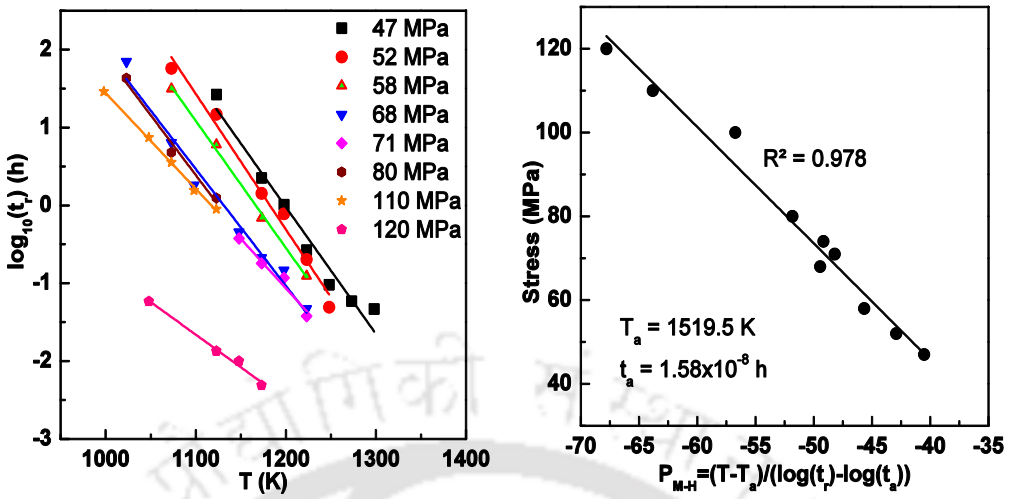

(a) (b)

Figure 4.53. Plot of (a) $\log_{10}(t_r)$ vs. T to determine T_a and $\log_{10}(t_a)$ and (b) Manson-Haferd master curve.

The $P_{M\text{-}H}$ values for stresses in the range from 5 to 45 MPa obtained by linear extrapolating the curve shown in Figure 4.53(b) are given in Table 4.8.

Table 4.8. $P_{M\text{-}H}$ values for various stress values.

Stress (MPa)	$P_{M\text{-}H}$
5	-25.34
10	-27.14
15	-28.94
20	-30.74
25	-32.54
30	-34.34
35	-36.14
40	-37.94
45	-39.74

The creep life t_r is determined using the equation

$$t_r = 10^{\left[\left(\frac{(T-1519.5)}{P_{M-H}}\right)-7.8\right]} \quad (4.20)$$

Figure 4.54(a) & (b) show the creep life of the investigated material plotted for different stresses and temperature, respectively. The plot indicates that the creep life at constant stress (or temperature) increases with decrease in temperature (or stress), which is the expected trend.

TH-1394_09610307

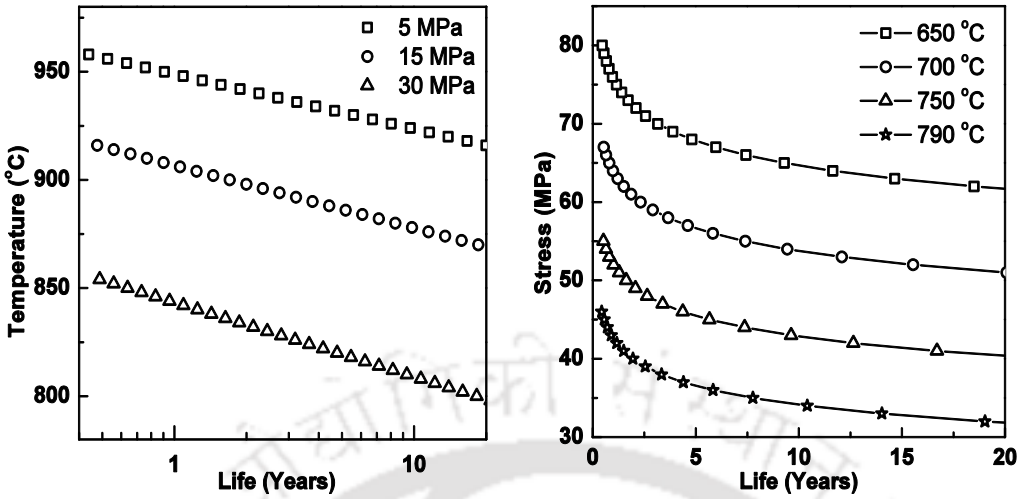

(a) (b)

Figure 4.54. Plot of (a) temperature-predicted creep life and (b) stress-predicted creep life for Manson-Haferd parameter.

4.4.2.2 Orr-Sherby-Dorn Technique

In this, the Orr-Sherby-Dorn parameter $P_{O\text{-}S\text{-}D}$ was determined using Eq. 2.15. The master curve for the Orr-Sherby-Dorn parametric technique is obtained by the σ vs. $P_{O\text{-}S\text{-}D}$ plot. The liner relationship between the stress and $P_{O\text{-}S\text{-}D}$ can be expressed as:

$$\sigma = a_0 + a_1 P_{O-S-D} \tag{4.21}$$

The $P_{O\text{-}S\text{-}D}$ values were found to be different when different values of Q_c are used in Eq. 2.16. Plot of best stress σ vs. $P_{O\text{-}S\text{-}D}$ master curve is obtained when the optimum value of Q_c was chosen. The optimum value of Q_c is corresponding to the case where R^2 for the linear fit of the stress σ vs. $P_{O\text{-}S\text{-}D}$ master curve is maximum. Figure 4.55(a) shows the variations of coefficient of determination with the constant Q_c by trial and error. From this plot, the best fit is obtained for a Q_c value of 556 kJ/mol for which R^2 = 0.968. The corresponding values of constants a_0 and a_1 in Eq. 4.21 are respectively -18.56 and -404.16.

The $P_{O\text{-}S\text{-}D}$ value for stresses outside the domain of investigation is obtained by linear extrapolation of the master curve. The creep life for any combination of temperature and stress is determined using the expression

$$t_r = 10^{\left[\left(P_{O-S-D} + \frac{Q_c}{2.3RT}\right)\right]} \tag{4.22}$$

TH-1394_09610307

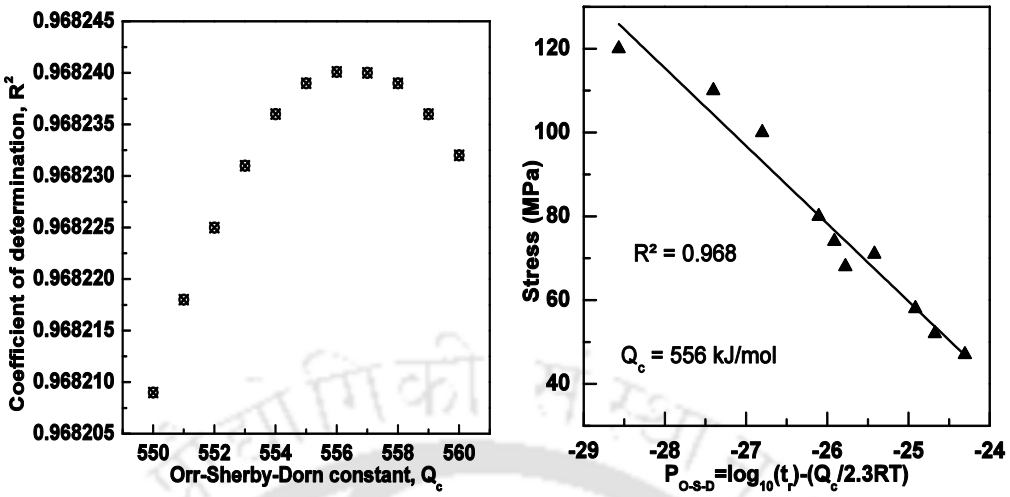

(a) (b)

Figure 4.55. Plot of (a) Variation of coefficient of determination for linear fit with Q_c and (b) Orr-Sherby-Dorn master curve.

Figure 4.55(b) shows the σ vs. $P_{O\text{-}S\text{-}D}$ master plot obtained for the steel. Values of $P_{O\text{-}S\text{-}D}$ determined from the master curve for various stresses are given in table 4.9.

Table 4.9. $P_{O\text{-}S\text{-}D}$ values at different stresses.

Stress (MPa)	$P_{O\text{-}S\text{-}D}$
5	-22.05
10	-22.32
15	-22.59
20	-22.86
25	-23.13
30	-23.40
35	-23.67
40	-23.94
45	-24.21

The creep life at any temperatures and stress was determined using the expression

$$t_r = 10^{\left[\left(P_{O-S-D}+\frac{556\times1000}{2.3RT}\right)\right]} \quad (4.23)$$

Figure 4.56(a) & (b) shows the creep life of the HP40Nb steel at constant stresses and temperatures. The creep life of the steel determined by Orr-Sherby-Dorn parameter, using Eq. 4.23, increases with the decrease in temperature at a constant stress. Figure 4.56(b) also reveals that at a constant temperature, the creep life decreases with increase in stress.

TH-1394_09610307

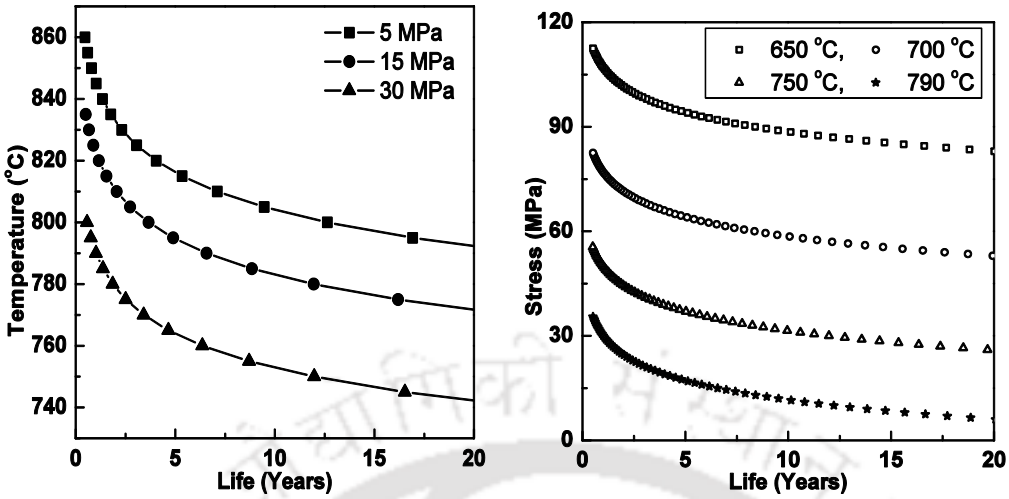

(a) (b)

Figure 4.56. Plot of (a) temperature-predicted creep life and (b) stress-predicted creep life for Orr-Sherby-Dorn parameter.

4.4.2.3 Larson-Miller Technique

Larson-Miller parameter is widely accepted by industries to predict creep life of materials. As described in section 2.9.1, the Larson-Miller parameter $P_{L\text{-}M}$ is expressed in the form

$$P_{L-M} = T(C_{L-M} + \log_{10} t_r) \times 10^{-3} \tag{4.24}$$

where T is the test temperature, t_r is the total rupture time and $C_{L\text{-}M}$ is a constant obtained graphically as discussed section 2.9.1. Figure 2.12 shows the typical plot of $\log_{10}(t_r)$ vs. $1/T$ for constant stresses. The Larson-Miller parametric technique is under the assumption that these iso-stress lines, when extended, intersects the vertical axis at $1/T = 0$ at a particular point, the value of which is taken as the value of $C_{L\text{-}M}$. Using the σ vs. $P_{L\text{-}M}$ master curve, the creep life at any temperature and stress is estimated by the expression:

$$t_r = 10^{\left[\left(1000 \times \frac{P_{L-M}}{T}\right) - C_{L-M}\right]} \tag{4.25}$$

A close observation would reveal that the $\log_{10}(t_r)$ vs. $1/T$ plots for different applied stresses indicates that the iso-stress curves when extended intersect the vertical axes at different points, each point correspond to different value of $C_{L\text{-}M}$. A plot of $C_{L\text{-}M}$ vs. σ indicates a straight line fit which can be expressed as:

$$C_{L-M} = a_2 + a_3\sigma \tag{4.26}$$

TH-1394_09610307

where a_2 and a_3 are constants and can be determined from by a least square fit. By substituting Eq. 4.26 for the $C_{L\text{-}M}$ in Eq. 4.24, the $P_{L\text{-}M}$ relationship can be modified as:

$$P_{L-M}(\sigma) = T(\log_{10} t_r + (a_2 + a_3 \times \sigma)) \times 10^{-3} \quad (4.27)$$

Figure 4.57(a) & (b) show the plots of $\log_{10}(t_r)$ vs. $1/T$ for different constant stresses. From the figure (Figure 4.57(b)) it is evident that the iso-stress lines, when extended, are intersecting the $\log_{10}(t_r)$ axis at different points indicating different $C_{L\text{-}M}$ values. The value of $C_{L\text{-}M}$ is found to lay between 11 - 20 for the stress in the range 47 MPa - 120 MPa. The plot of $C_{L\text{-}M}$ vs. σ shown in Figure 4.57(c) indicates a linear relationship between $C_{L\text{-}M}$ and σ. The constants a_2 and a_3 in Eq. 4.26 are determined as -0.122 and 25.438, respectively.

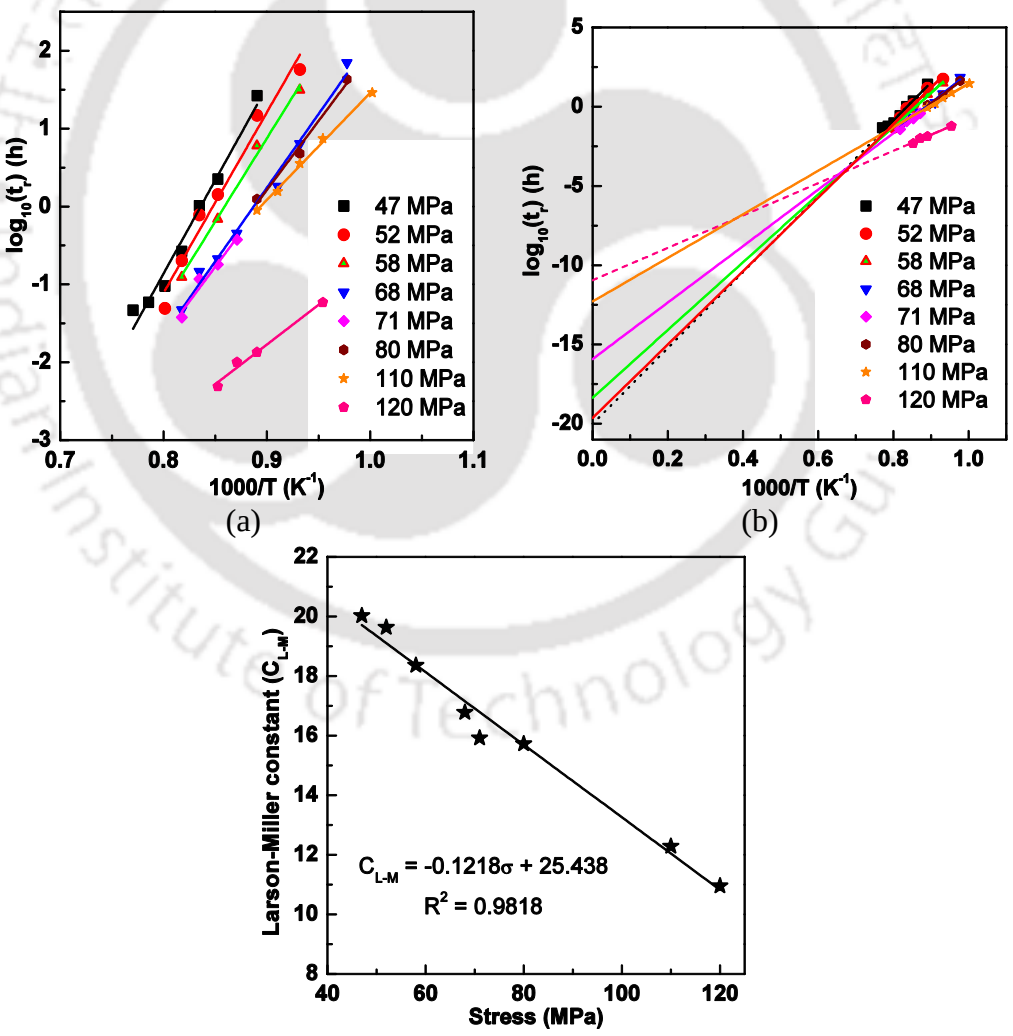

Figure 4.57. Plot of (a) $\log_{10}(t_r)$ vs. $1000/T$, (b) $\log_{10}(t_r)$ vs. $1000/T$ with extrapolated curves up to 1000/T = 0 and (c) $C_{L\text{-}M}$ vs. σ.

For austenitic steels, the $C_{L\text{-}M}$ value proposed by Larson and Miller for obtaining the σ vs. $P_{L\text{-}M}$ master plot is 20 [10]. The σ vs. $P_{L\text{-}M}$ plots for the reformer tube is shown in Figure 4.58(a) indicating linear relationships. In the figure, continuous line corresponds to the case where $C_{L\text{-}M}$ =20 and the other dotted line corresponds to the case where $C_{L\text{-}M}$ is a function of σ (i.e $C_{L\text{-}M}(\sigma)$). The figure indicates large scatter in the data points when $C_{L\text{-}M}$ is considered as constant compared to the case where $C_{L\text{-}M}(\sigma)$. The R^2 value for the former case is 0.84, whereas for the latter case it is 0.92. Hence, the master plot considering $C_{L\text{-}M}(\sigma)$ appears to be more realistic for the prediction of long-term creep rupture life of the investigated material. Figure 4.58(b) shows the plot of σ vs. average $P_{L\text{-}M}$ plots for each stress with $C_{L\text{-}M}$ =20 and $C_{L\text{-}M}(\sigma)$. The coefficient of determination R^2 for curve with $C_{L\text{-}M}$ =20 and $C_{L\text{-}M}(\sigma)$ are found to be 0.948 and 0.992, respectively.

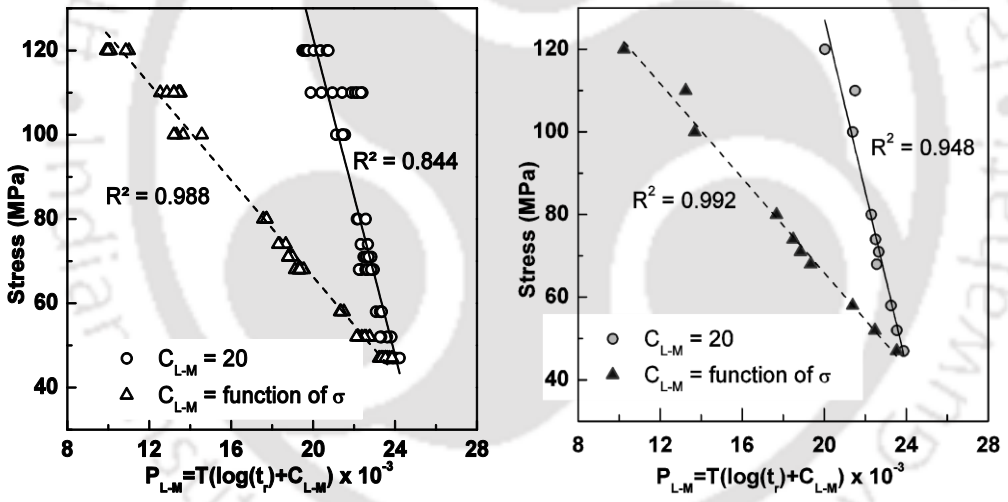

(a) (b)

Figure 4.58. Plot of (a) σ vs. $P_{L\text{-}M}$ and (b) σ vs. average $P_{L\text{-}M}$.

For the creep life prediction of the material at low stress levels, the $P_{L\text{-}M}$ value is obtained by extrapolating the master curve to low stress values. The extrapolated values of $P_{L\text{-}M}$ determined for stresses in the range 5 MPa - 45MPa for the service exposed reformer tube are given in Table 4.10 for both cases.

The creep life of the reformer tube for both the cases, i.e., $C_{L\text{-}M}$ =20 and $C_{L\text{-}M}(\sigma)$ is determined by Eq. 4.28 and Eq. 4.29, respectively.

$$t_r = 10^{\left[\left(1000\times\frac{P_{L-M}}{T}\right)-20\right]} \tag{4.28}$$

TH-1394_09610307

$$t_r = 10^{\left[\left(1000\times\frac{P_{L-M}}{T}\right)-(-0.122\times\sigma+25.438)\right]} \quad (4.29)$$

Table 4.10. $P_{L\text{-}M}$ and $C_{L\text{-}M}$ values at different stresses.

Stress (MPa)	$P_{L\text{-}M}$ for $C_{L\text{-}M}$ = 20 ($\times10^{-3}$)	$C_{L\text{-}M}$ (σ)	$P_{L\text{-}M}$ for $C_{L\text{-}M}$ (σ) ($\times10^{-3}$)
5	25.83	24.83	30.66
10	25.60	24.22	29.79
15	25.36	23.61	28.91
20	25.12	23.00	28.04
25	24.88	22.39	27.16
30	24.65	21.78	26.29
35	24.41	21.18	25.41
40	24.17	20.57	24.54
45	23.93	19.96	23.66

It is evident from Figure 4.59(a) & (b) that the creep life decrease with increase in temperature. Table 4.11 compares the creep life (i.e. time to attain a creep strain of 0.15) of the material predicted for different combinations of stresses and temperatures, by considering $C_{L\text{-}M}$ = 20 and $C_{L\text{-}M}(\sigma)$. It is clear from Figure 4.59 and Table 4.11 that the creep life of the materail predicted by considering $C_{L\text{-}M}$ = 20 is higher compared to that predicted by considering $C_{L\text{-}M}(\sigma)$. Figure 4.60(a) & (b) shows the plot of σ vs. creep life of the investigated steel. Both the figures show that the creep life decreases with increase in stress. At 790 °C and 1 MPa, the estimated creep life of the steel is 3.5 years and 1.8 years for the case $C_{L\text{-}M}$ = 20 and $C_{L\text{-}M}(\sigma)$, respectively.

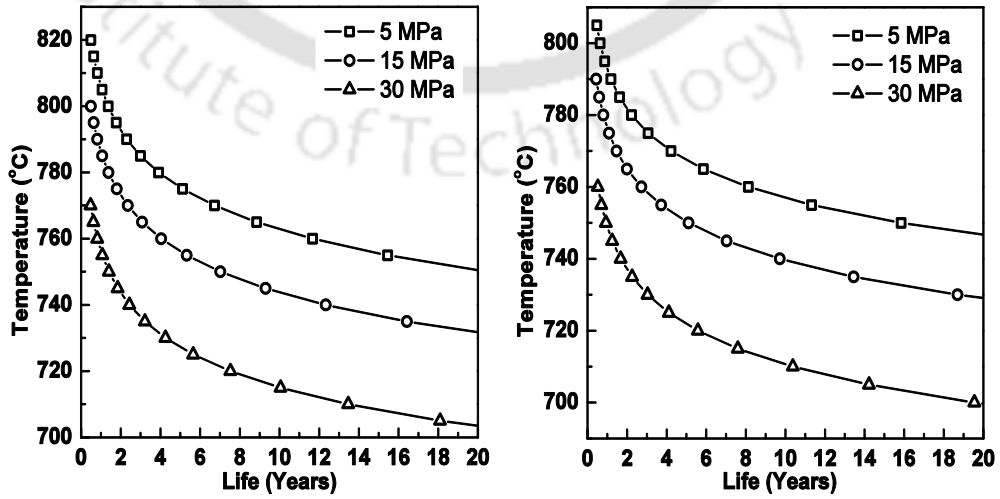

(a) (b)

Figure 4.59. Temperature-predicted creep life for (a) constant $C_{L\text{-}M}$ and (b) $C_{L\text{-}M}(\sigma)$ up to creep strain 0.15.

TH-1394_09610307

Table 4.11. Creep life at a creep strain of 0.15 of the reformer tube for different stress and temperature combinations.

Stress (MPa)	Temperature (˚C)	Creep life (years)	
		$C_{L\text{-}M}$ = 20	$C_{L\text{-}M}(\sigma)$
5	800	1.36	0.64
10	780	2.32	1.33
15	760	4.04	2.72
20	740	7.18	5.41
25	720	13.07	10.44
30	700	24.38	19.55

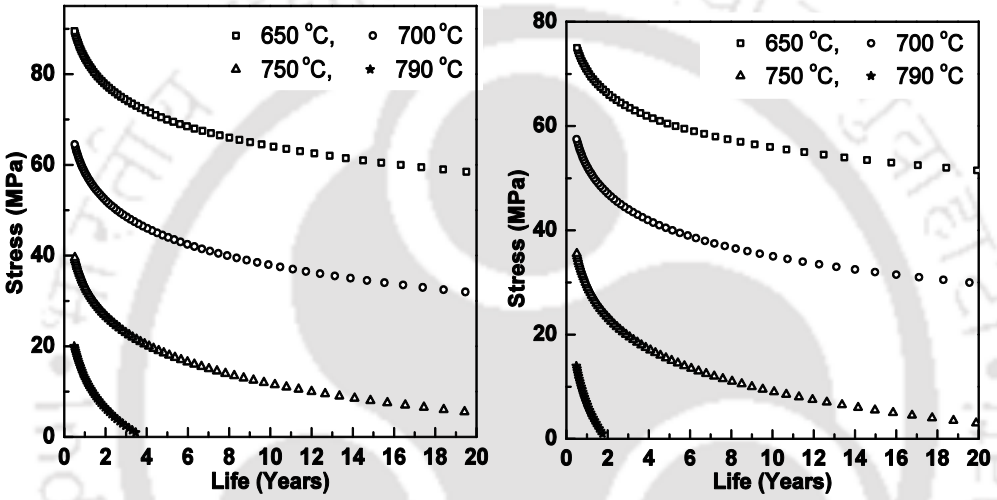

(a) (b)

Figure 4.60. Stress-predicted creep life for (a) constant $C_{L\text{-}M}$ and (b) $C_{L\text{-}M}$ as a function of stress up to creep strain 0.15.

For the three parametric techniques discussed in this work, the strain to failure criteria is considered as 0.15 (i.e an engineering strain of 16.2%). A comparison of the creep failure time predicted by these three parametric techniques are presented in Table 4.12. It is evident from the table that the creep life determined by Mansion-Hafred method and Orr-Sherby-Dorn method gives highly overestimated values. The creep life determined by L-M technique considering $C_{L\text{-}M}$ = 20 is higher than that predicted considering $C_{L\text{-}M}(\sigma)$.

Figure 4.61(a) shows the plot of T vs. creep life of the HP40Nb steel at 5 MPa and 30 MPa obtained by the Larson-Miller method considering $C_{L\text{-}M}$ =20 and $C_{L\text{-}M}(\sigma)$. At 800 °C and 5 MPa, the estimated creep life of the steel is 1.34 years and 0.64 years for the case $C_{L\text{-}M}$ = 20 and $C_{L\text{-}M}(\sigma)$, respectively. At 710 °C / 30 MPa the respective creep lives are found to be 13.4 years and 10.4 years. Variation of predicted creep life at 650 °C and 750 °C considering $C_{L\text{-}M}$ as a constant and as a function of stress is shown in

TH-1394_09610307

Figure 4.61(b). At 650 °C and 70 MPa, the estimated creep life of the steel is 5 years and 1.1 years for the case $C_{L\text{-}M}$ = 20 and $C_{L\text{-}M}(\sigma)$, respectively. At 750 °C / 6 MPa the respective creep lives are found to be 18.4 years and 14.2 years.

Table 4.12. Comparison of creep life at a creep strain of 0.15 between different parametric techniques.

Applied stress (MPa)	Creep life (Years)	Temperature (°C)			
		Larson Miller method with $C_{L\text{-}M}$ = 20	Larson Miller method with $C_{L\text{-}M}(\sigma)$	Manson-Haferd method	Orr-Sherby-Dorn method
5	1	806	793	949	845
5	2	793	782	941	833
5	5	776	768	931	816
5	10	763	757	924	804
10	1	796	785	928	834
10	2	783	773	920	821
10	5	766	759	909	805
10	10	753	749	901	793
15	1	786	776	907	822
15	2	773	765	898	810
15	5	756	750	886	795
15	10	743	740	878	783
20	1	776	767	886	812
20	2	763	756	876	800
20	5	747	741	864	784
20	10	734	730	855	773

The creep life prediction by Larson-miller parameter is sensitive to the $C_{L\text{-}M}$ value. It may be noted that under constant stress test condition, the iso-stress lines in the $\log_{10}(t_r)$ vs. $1/T$ plot are not meeting at a single point leads to inaccurate results. Since, the $C_{L\text{-}M}$ value depends on the applied stress, this modification is required to be incorporated in the L-M method. The result obtained from the analysis indicates lower creep life by considering $C_{L\text{-}M}(\sigma)$ compared to a constant $C_{L\text{-}M}$ value. The creep life determined by considering $C_{L\text{-}M}(\sigma)$ is more conservative from the design point of view.

TH-1394_09610307

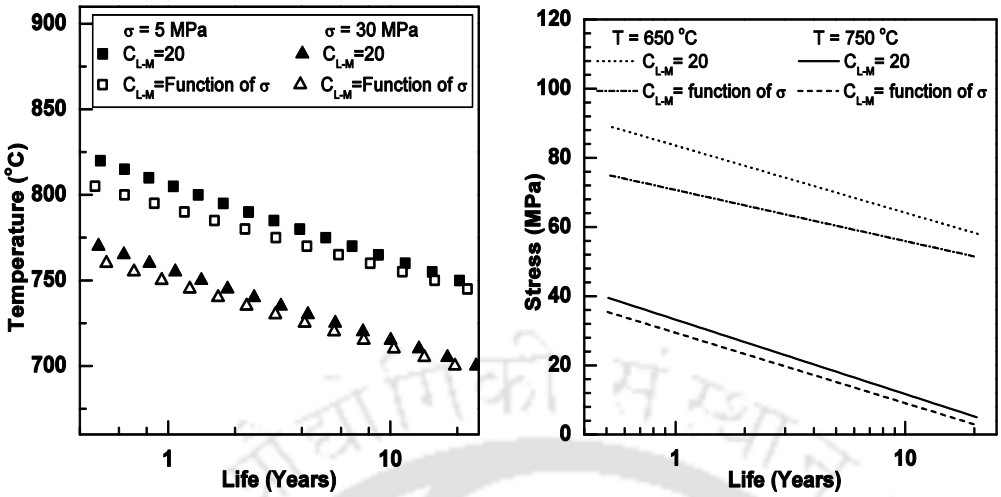

(a) (b)

Figure 4.61. Comparison of (a) temperature and (b) stress vs. predicted creep life for $C_{L\text{-}M}$ as a constant and $C_{L\text{-}M}(\sigma)$.

Summary

The experimental results from microstructural analysis, elevated temperature tensile tests and creep tests on service exposed HP40Nb micro-alloyed stainless steel are presented in this chapter. The relationship for determining the minimum creep rate was developed by constitutive modeling. Relationship between minimum creep rate and creep rupture time were verified by Monkman-Grant relationships. Creep curves for the material within the test domain were generated successfully by ANN modeling and simulation where 98 % of the data could be predicted within a deviation error of ± 10 %. Comparison of the minimum creep rate estimated by the constitutive modeling and ANN modeling revealed that the value obtained by ANN technique was closely matching with the experimental results. Creep life of the material was estimated by Larson-Miller technique, Manson-Haferd technique and Orr-Sherby-Dorn technique and the results compared. The creep life determined by Manson-Haferd method and Orr-Sherby-Dorn method were found to be highly over-estimated. The creep life estimated by Larson-Miller method is sensitive to the $C_{L\text{-}M}$ value. It is proposed that the $C_{L\text{-}M}$ in the $P_{L\text{-}M}$ expression be modified by stress dependent function.

TH-1394_09610307

CHAPTER 5

CONCLUSIONS & SCOPE FOR FUTURE WORK

5.1 Conclusions

The experimental methodology, the modeling studies performed on micro-alloyed HP40Nb austenitic stainless steel, their results and discussions were presented in the earlier chapters. The experiments were mainly investigating the microstructure, elevated temperature tensile tests and creep testing of the investigated steel. The modeling studies revealed the importance of analysis of creep deformation and failure by various existing techniques. Artificial Neural Network (ANN) was used successfully for modeling creep deformation of the steel. The creep life prediction of the steel was carried out by various existing techniques and compared. These investigations revealed many new findings, which are highlighted below:

- Microstructure of the HP40Nb steel consists of equiaxed austenitic grains with continuous network of carbides at grain boundary regions. The grain boundary carbides are Cr_7C_3, $Cr_{23}C_6$, NbC, (Nb,Ti)C. The Cr_7C_3 carbides dissolve in the matrix with concomitant increase in $Cr_{23}C_6$ when the steel is exposed to temperatures above 1000 ˚C.
- The Young's modulus, yield strength and ultimate tensile strength of the steel decreased and percentage elongation increased with increase in temperature. Dissolution of Cr_7C_3 particles resulted in sharp decrease in strength of the steel. The strain hardening exponent of the steel increased with the increase in temperature up to 600 ˚C and decreased with further increase in temperature.
- Up to 600 ˚C, the failure in the material was by brittle fracture. Between 600 ˚C to 1000 ˚C the failure was dominated by ductile failure mechanism. *i.e.* by micro-void nucleation, growth and coalescence. At 1200 ˚C, the material failure was by inter-granular fracture.
- Strain to failure and secondary strain decreased with increase in minimum creep strain. Both these strains decreased with increase in applied stress above 900 ˚C. For constant stresses, secondary strain increased and strain to failure decreased with the increase in temperature.

TH-1394_09610307

- Minimum creep rate at a constant temperature increases with the increase in stress. Rupture time at a constant stress decreases exponentially with the increase in temperature.
- Stress exponent and apparent activation energy for creep decreases non-linearly with the increase in temperature and stress respectively. Power-law creep expression shows better result among different constitutive equations.
- Nucleation of voids in the vicinity of Cr-rich carbide, its subsequent growth and coalescences is the main creep failure mechanism of the steel.
- At lower temperature, fracture is quasi-brittle failure where as at elevated temperature, the material failure is by ductile fracture.
- The threshold stress during the creep test is negligible.
- Both Monkman-Grant and modified Monkman-Grant relationships were found to be valid for the steel.
- Low value of the creep damage tolerance factor λ, indicates large creep strain accumulation during secondary creep region.
- Time to reach Monkman-Grant ductility t_{MGD} was found to be 80 % of the rupture time of the steel confirming secondary strain as the major contributor to the total strain.
- Time dependent creep strain for various combinations of stresses and temperatures was simulated successfully for the first time. The comparison of the creep curves simulated by ANN technique with the experimentally determined curves show good prediction capability by ANN modeling.
- The minimum creep rate obtained by ANN simulation was found to be more accurate than that obtained by the constitutive modeling technique.
- Creep life prediction by various parametric techniques reveals prediction by Larson-Miller parameter as the most suitable prediction technique compared to Manson-Hafred and Orr-Sherby-Dorn technique.

TH-1394_09610307

- It is proposed that $C_{L\text{-}M}$ in the $P_{L\text{-}M}$ equation should be modified as a function of stress rather than considering it as a constant. While considering $C_{L\text{-}M}(\sigma)$ the scatter in the master plot is reduced. The creep life prediction considering $C_{L\text{-}M}(\sigma)$ gives conservative result compared to when considering $C_{L\text{-}M}$ as constant.

.

5.2 Main Contribution of This Work

The two major contribution of this thesis are:

a. The work demonstrates that creep curves can be predicted by ANN modeling using limited experimental data, within acceptable accuracy. Though the creep failure norm used in this work considering the practical condition of creep failure strain as 0.15, the technique can be extended to higher failure strains depending upon the material and test conditions.

b. A modification in the Larson-Miller parametric technique for the prediction of failure time is proposed by considering Larson-Miller constant $C_{L\text{-}M}$ as a function of stress. The creep life prediction by the proposed modification leads to conservative results useful from the design point of view.

5.3 Scope for Future Work

The present investigations were focused on investigating the high temperature tensile and creep failure of the HP40Nb steel. The work also demonstrated the capability of artificial neural network technique in simulating creep curves from the data obtained from limited experiments. These investigations have not only yielded many interesting results but have also pointed towards several possible directions of further research. Some of these are enumerated below:

- The present work was concentrated in austenitic stainless steel where the material undergoes no phase transformation. The present methodology may be extended to a variety of materials with different crystal structures.
- The present work was limited to the creep data of HP40Nb steel. Further investigations may be carried out to study the cavitation and its effect on the creep deformation of this material.

TH-1394_09610307

- Further investigation of this steel under high resolution TEM would throw more light on the nature of the various phases present under various heat treatment conditions.
- The high temperature fracture toughness, corrosion resistance and thermal fatigue resistance of this material would help in assessing the potential of this steel for a wide range of application.
- Application of ANN technique may be extended to predict the creep life of material exhibiting phase transformations during different conditions of creep tests.
- The proposed modified Larson-Miller parameter technique for predicting the creep failure time may be validated for other materials.

TH-1394_09610307

REFERNCES

1 G. Quickel, C. Jaske, B. Rollins and J. Beavers, "Failure analysis and remaining life assessment of methanol reformer tubes", *Journal of Failure Analysis and Prevention*, 2009, vol. 9, pp. 511-516.

2 M. Garbiak, W. Jasiński and B. Piekarski, "Materials for reformer furnace tubes", *History of evolution, Archieves of Foundry Engineering*, 2011, vol. 11, pp. 47-52.

3 America Metal Academy, Capability and choice: Steel material for stainless steel, tool and special purpose, Metal Manual, 9th edition.

4 D.J. Cox and D.E. Jordan, "Materials Technology in Steam Reforming Processes", Pergamon Press, London, 1964.

5 R.H. Kane, "Effects of silicon content and oxidation potential on the carburization of centrifugally cast HK-40", *Corrosion*, 1981, vol.37, pp. 187-199.

6 S.J. Zhu, P.E. Li, J. Zhao and Z.B. Cao, "The effect of prior aging on the creep crack growth behaviour of austenitic HK40 steel", *Materials Science and Engineering A*, 1989, vol. 114, pp. 7-12.

7 C. Stallybrass and G. Sauthoff, "Ferritic Fe-Al-Ni-Cr alloys with coherent precipitates for high-temperature applications", *Materials Science and Engineering A*, 2004, vol. 387-389, pp. 985-990.

8 C.S. Li and Y.S. Yang, "A glass based coating for enhancing anti-coking and anti-carburizing abilities of heat-resistant steel HP", *Surface & Coatings Technology*, 2004, vol. 185, pp. 68-73.

9 F. Lechermama, M. Fahnlea and J.M. Sanchez, "First-principles investigation of the Ni-Fe-Al system", *Intermetallics*, 2005, vol. 13, pp. 1096-1109.

10 F.R. Larson and J. Miller, Time-Temperature Relationship for Rupture and Creep Stresses, *Transaction ASME*, 1952, vol. 74, pp. 765-775.

11 R.L. Orr, O.D. Sherby and J.E. Dorn, "Correlations of rupture data for metals at elevated temperature", *Transactions ASM*, 1954, vol. 46, pp. 113-128.

12 S.S. Manson and A.M. Haferd, A linear time-temperature relation for extrapolation of creep and stress rupture data, NACA TN2890, 1952, pp. 1-49.

13 R.W. Evan and B. Wilshire, Creep of metals and alloys, The Institute of Materials, London, 1985, p.197.

14 M. Prager, "The Omega method: an engineering approach to life assessment", *Journal of Pressure Vessel Technology*, 2000, vol. 122, pp. 273-280.

15 K. Maruyama, C. Tanaka and H. Oikawa, "Long-term creep curve prediction based on the modified θ projection concept", *Transactions ASME, Journal of Pressure Vessel Technology*, 1990, vol. 112, pp. 92-97.

TH-1394_09610307

16 Z. Wang, C. K. Chiang, and T.J. Chuang, "Optimum design of a ceramic tensile creep specimen using a finite element method", *Journal of Research of the National Institute of Standards and Technology*, 1997, vol. 102, pp. 15-28.

17 H.J. Renner, F. Marschner, Catalytic reforming of natural gas and other hydrocarbon, B. Elvers, S. Hawkins, M. Ravenscroft, J.F. Rousaville and G. Schulz (eds.), Ullmann's encyclopedia of industrial chemistry, vol. A2, 5th ed., VCH Verlagsgesellschaft, Weinheim, Germany, 1985, pp.143-242.

18 American Petroleum Institute, Calculation of heater-tube thickness in petroleum refineries, API recommended practice 530, 3rd ed., Washington (DC), 1988.

19 C.J. Liu and Y. Chen, "Variation of the microstructure and mechanical properties of HP40Nb hydrogen reformer tube with time at elevated temperature", *Materials and Design*, 2011, vol. 32, pp. 2507-2512.

20 M.B. Zaghoul, T. Shinoda and R. Tanaka, "Relation between structure and creep rupture strength of centrifugally cast HK40 steel", *Transactions ISIJ*, 1977, vol. 17, pp. 28-36.

21 D. J. Cox and D.E. Jordan, Materials Technology in Steam Reforming Processes, Pergamon Press, London, 1964.

22 R.H. Kane, "Effects of silicon content and oxidation potential on the carburization of centrifugally cast HK-40", *Corrosion*, 1981, vol.37, pp. 187-199.

23 S.J. Zhu, P. E. Li, J. Zhao, Z.B. Cao, "The effect of prior aging on the creep crack growth behaviour of austenitic HK40 steel", *Materials Science and Engineering A*, 1989, vol. 114, pp. 7-12.

24 C. Stallybrass and G. Sauthoff, "Ferritic Fe-Al-Ni-Cr alloys with coherent precipitates for high-temperature applications", *Materials Science and Engineering A*, 2004, vol. 387-389, pp. 985-990.

25 C. S. Li and Y. S. Yang, "A glass based coating for enhancing anti-coking and anti-carburizing abilities of heat-resistant steel HP", *Surface & Coatings Technology*, 2004, vol. 185, pp. 68-73.

26 F. Lechermama, M. Fahnlea and J.M. Sanchez, "First-principles investigation of the Ni-Fe-Al system", *Intermetallics*, 2005, vol. 13, pp. 1096-1109.

27 A. Alvino, D. Lega, F. Giacobbe, V. Mazzocchi and A. Rinaldi, "Damage characterization in two reformer heater tubes after nearly 10 years of service at different operative and maintenance conditions", *Engineering Failure Analysis*, 2010, vol. 17, pp. 1526-1541.

28 L.H. DeAlmeida, A.F. Ribeiro and I.L. May, "Microstructural characterization of modified 25Cr-35Ni centrifugally cast steel furnace tubes", *Materials Characterization*, 2003, vol. 49, pp. 219-229.

29 J. Swaminathan, K. Guguloth, M. Gunjan, P. Roy and R. Ghosh, "Failure analysis and remaining life assessment of service exposed primary reformer heater tubes", *Engineering Failure Analysis*, 2008, vol. 15, pp. 311-331.

TH-1394_09610307

30 W.Z. Wang, F.Z. Xuan, Z.D. Wang, B. Wang and C.J. Liu, "Effect of overheating temperature on the microstructure and creep behavior of HP40Nb alloy", *Materials & Design*, 2011, vol. 32, pp. 4010-4016.

31 S.J. Zhu, D.J. Li, Y. Wang, W.Q. Tian, S.G. Xu and F.G. Wang, "Effect of niobium on creep and creep crack growth of cast Ni-Cr austenitic steel", *Materials Science and Technology*, 1990, vol. 6, pp. 1193-1198.

32 J. Yan, Y. Gao, F. Yang, C. Yao, Z. Ye, D. Yi and S. Ma, "Effect of tungsten on the microstructure evolution and mechanical properties of yttrium modified HP40Nb alloy", *Materials Science and Engineering A*, 2011, vol. 529, pp. 361-369.

33 G.D.A. Soares, L.H. deAlmedia, T.L. daSilveira and I.L. May, "Niobium additions in HP heat-resistant cast stainless steels", *Materials Characterization*, 1992, vol. 29, pp. 387-396.

34 R. Voicu, J. Lacaze, E. Andrieu, D. Poquillon and J. Furtado, "Creep and tensile behaviour of austenitic Fe-Cr-Ni stainless steels", *Materials Science and Engineering A*, 2009, vol. 510-511, pp. 185-189.

35 K. Guan, H. Xu and Z. Wang, "Quantitative study of creep cavity area of HP40 furnace tubes", *Nuclear Engineering and Design*, 2005, vol. 235, pp. 1447-1456.

36 R. Kirchheiner and P. Woelpert, "Niobium in centrifugally cast tubes for petrochemical applications", Proceedings of the International Symposium Niobium, Orlando, USA, 2001.

37 T. Sourmail, "Precipitation in creep resistant austenitic stainless steels", *Materials Science and Technology*, 2001, vol. 17, pp. 1-14.

38 R. Voicu, E. Andrieu, D. Poquillon, J. Furtado and J. Lacaze, "Microstructure evolution of HP40-Nb alloys during aging under air at 1000 °C", *Materials Characterization*, 2009, vol. 60, pp. 1020-1027.

39 A.K. Ray, S. Kumar, G. Krishna, M. Gunjan, B. Goswami and S.C. Bose, "Microstructural studies and remnant life assessment of eleven years service exposed reformer tube", *Materials Science and Engineering A*, 2011, vol. 529, pp. 102-112.

40 H.C. Furtado and I. Le May, "High temperature degradation in power plants and refineries", *Materials Research*, 2004, vol. 7, pp. 103-110.

41 M.F. Ashby and D.R.H. Jones, "Engineering Materials 1: An introduction to their properties and applications", Butterworth-Heinemann, Wobum, USA, 2nd ed., 2002, pp. 172.

42 G. E. Dieter, Mechanical Metallurgy, McGraw-Hill Book Co. Ltd., UK, SI Metric ed., 1988.

43 A. Graham and K.F.A. Walles, "Relations between long and short time properties of commercial alloys", *Journal of the Iron and Steel Institute*, 1955, vol. 193, pp. 105.

TH-1394_09610307

44 F. Phillips, "The slow stretch in India rubber, glass and metal wire when subjected to a constant pull", *Philosophical Magazine*, 1905, vol.9, pp. 513.

45 P.G. McVetty, "Factors affecting the choice of working stresses for high temperature service", *Transactions ASME*, 1933, vol. 55, pp. 99.

46 J.B. Conway and M.J. Mullikin, "An evaluation of various first stage creep equations", Proceedings of AIME conference, Detroit, Michegan, 1962.

47 F.N. Norton, The creep of steel at high temperature, McGraw Hill, New York, 1929.

48 L. Prandtl, "Ein gedankenmodell zur kinetischen theorie der festen körper", *ZAMM- Journal of Applied Mathematics and Mechanics*, 1928, vol. 8, pp. 85-106.

49 A. Nadai, "The influence of time upon creep, The hyperbolic sine law", S. Timoshenko Anniversary Volume, The Macmillian Co., New York, 1938, pp. 155.

50 D. McHenry, "A new aspect of creep in concrete and its application to design", *Proceedings of ASTM*, 1943, vol.43, pp. 1069.

51 Y.N. Rabotnov, "Creep problems in structural members", Amsterdam, North-Holland, 1969.

52 L.M. Kachanov, "Time of the fracture process under creep conditions", *Izv A Kad Nauk SSSR, Otd Techn Nauk*, 1958, vol. 8, pp. 26-31.

53 R. Sandström and A. Kondyr, "A model for tertiary creep in Mo- and CrMo-steels", Proceedings of third International Conference on Mechanical Behaviour of Materials, Cambridge, 1979.

54 D.A. Woodford, "Creep and rupture of an advanced fiber strengthened eutectic composite superalloy", *Metallurgical Transactions A*, 1977, vol. 8 pp. 639-650.

55 Z. L. Gong and T. R. Hsu, "Deformation of aluminum alloy under cyclic creep loadings", *Journal of Testing and Evaluation*, 1991, vol. 19, pp. 14-23.

56 X.P. Zhang, C.B. Yu, Y.P. Zhang, S. Shrestha and L. Dorn, "Processing treatment of a lead-free Sn-Ag-Cu-Bi solder by rapid laser-beam reflowing and the creep property of its soldered connection", *Journal of Materials Processing Technology*, 2007, vol. 192-193, pp. 539-542.

57 S.R. Holdsworth, M. Askins, A. Baker, E. Gariboldi, S. Holmström, A. Klenk, M. Ringel, G. Merckling, R. Sandstrom, M. Schwienheer and S. Spigarelli, "Factors influencing creep model equation selection", *International Journal of Pressure Vessels and Piping*, 2008, vol. 85, pp. 80-88.

58 E. Kandare, S. Feih, A. Kootsookos, Z. Mathys, B.Y. Lattimer and A.P. Mouritz, "Creep-based life prediction modeling of aluminum in fire", *Materials Science and Engineering A*, 2010, vol. 527, pp.1185-1193.

59 A.K. Mukherjee, J.E. Bird and J.E. Dorn, "Experimental correlation for high temperature creep", *Transactions ASM*, 1969, vol. 62, pp. 155-179.

TH-1394_09610307

60 J. Weertman, "Theory of steady state creep based on dislocation climb", *Journal of Applied Physics*, 1955, vol. 26, pp. 1213-1217.

61 R. Mahmudi, A.R. Geranmayeh and A. Rezaee-Bazzaz, "Impression creep behavior of lead-free Sn-5Sb solder alloy", *Materials Science and Engineering A*, 2007, vol. 448, pp. 287-293.

62 F. Gao and T. Takemoto, "Mechanical properties evolution of Sn-3.5Ag based lead-free solders by nanoindentation", *Materials Letters*, 2006, vol. 60, pp. 2315-2318.

63 I. Shohji, T. Yoshida, T. Takahashi and S. Hioki, "Tensile properties of Sn-Ag based lead-free solders and strain rate sensitivity", *Materials Science and Engineering A*, 2004, vol. 366, pp. 50-55.

64 S. Wiese, F. Feustel and E. Meusel, "Characterisation of constitutive behaviour of SnAg, SnAgCu and SnPb solder in flip chip joints", *Sensors and Actuators A: Physical*, 2002, vol. 99, pp. 188-193.

65 S. Wiese and E. Meusel, "Characterization of lead-free solders in flip chip joints", *Journal of Electronic Packaging*, 2003, vol. 125, pp. 531-538.

66 S. Wiese and S. Rzepka, "Time-independent elastic-plastic behaviour of solder materials", *Microelectronics Reliability*, 2004, vol. 44, pp. 1893-1900.

67 A. Schubert, Proceedings of IEEE 53rd Electronic Components and Technology Conference, New Orleans, Louisiana, USA, 2003, pp. 603-610.

68 Q. Zhang, Proceedings of IEEE 53rd Electronic Components and Technology Conference, New Orleans, Louisiana, USA, 2003, pp. 1862-1868.

69 P. Feltham, "The plastic flow of iron and plain carbon steels above the A3-Point", Proceeding Physics Society B, 1953, vol.66, pp. 865-884.

70 A.H. Cottrell and V. Aytekin, "The flow of zinc under constant stress", *Journal Institute of Metals*, 1950, vol. 77, pp. 389-422.

71 A.S. Novick and E.S. Machlin, "Dislocation theory as applied by N.A.C.A. to the creep of metals", *Journal of Applied Physics*, 1947, vol. 18, pp. 79-87.

72 P. Feltham, and J.D. Meakin, "Creep in face-centered cubic metals with special reference to copper", *Acta Metallurgica*, 1959, vol. 7, pp. 614-627.

73 P. Feltham, "On the creep of metals at very low temperatures", *Philosophical Magazine*, 1961, vol. 6, pp. 1301-1303.

74 O.D. Sherby and P.M. Burke, "Mechanical behavior of crystalline solids at elevated temperature", *Progress in Materials Science*, 1968, vol. 13, pp. 323-390.

75 A.E. Johnson and N.E. Frost, "Rheology of metals at elevated temperatures", *Journal of the Mechanics and Physics of Solids*, 1952, vol. 1, pp. 37-52.

76 A. Fawzy, N. Habib, M. Sobhy, E. Nassr and G. Saad, "Effect of Zn addition on steady state creep characteristics of Sn-3.3Ag solder alloy", *Materials Science and Technology*, 2008, vol. 24, pp. 488-494.

TH-1394_09610307

77 G. Saad, A. Fawzy and E. Shawky, "Effect of Ag addition on the creep characteristics of Sn-8.8 wt% Zn solder alloy", *Journal of Alloys and Compounds*, 2009, vol. 479, pp. 844-850.

78 A.M. Abd El-Khalek, "Effect of pre-deformation and phase transformation on the creep behaviour of Ag-1 wt% Cu alloy", *Materials Science and Engineering A*, 2010, vol. 527, pp. 4818-4822.

79 A. Schubert, H. Walter, R. Dudek, B. Michel, G. Lefranc, J. Otto and G. Mitic, "Thermo-mechanical properties and creep deformation of lead-containing and lead-free solders", Proceedings of International Symposium and Exhibition on Advanced Packaging Materials, Braselton, Georgia, USA, 2001, pp. 129-134.

80 B.A. Latella, T. Liu, K.U. Snowden, E.G. Mehrtens, G.R. Lumpkin and B.K. Gan, "Short-term flexural creep deformation in synroc-C", *Journal of Materials Science*, 2003, vol.38, pp. 3223-3231.

81 R.W. Evans and B. Wilshire, "Creep of metals and alloys", The Institute of Metals, London, 1985, pp. 113.

82 A. Seeger, "The generation of lattice defects by moving dislocations, and its application to the temperature dependence of the flow-stress of F.C.C. crystals", *Philosophical Magazine*, 1955, vol. 46, pp. 1194-1217.

83 N.F. Mott, Conference on Creep and Fracture of Metals at High Temperatures, H.M. Stationery Office, London, 1956, pp. 21.

84 P. Hirsch and D. Warrington, "The flow stress of aluminium and copper at high temperatures", *Philosophical Magazine*, 1961, vol. 6, pp. 735-768.

85 C.R. Barrett and W.D. Nix, "A model for steady state creep based on the motion of jogged screw dislocations", *Acta Metallurgica*, 1966, vol.13, pp. 1247-1258.

86 B. Derby and M.F. Ashby, "Power-laws, and the A-n correlation in creep", *Scripta Metallurgica*, 1984, vol.18, pp. 1079-1084.

87 O.A. Ruano and O.D. Sherby, "On constitutive equations for various diffusion controlled creep mechanisms", *Revue De Physique Appliquée*, 1988, vol. 23, pp. 625-637.

88 J.E. Dorn, "Some fundamental experiments on high temperature creep", *Journal of the Mechanics and Physics of Solids*, 1954, vol. 3, pp. 85-116.

89 D.R. Hayhurst, F. Vakili-Tahami and J.Q. Zhou, "Constitutive equations for time independent plasticity and creep of 316 stainless steel at 550 ˚C", *International Journal of Pressure Vessels and Piping*, 2003, vol. 80, pp. 97-109.

90 O.D. Sherby, J.L. Lytton and J.E. Dorn, "Activation energies for creep of high-purity aluminium", *Acta Metallurgica*, 1957, vol. 5, pp. 219-227.

91 P.R. Landon, J.L. Lytton, L.A. Shepard and J.E. Dorn, "The activation energies for creep of polycrystalline copper and nickel", *Transactions ASM*, 1959, vol.51, pp. 900.

92 W.J. McG. Tegart, "Activation energies for high temperature creep of polycrystalline magnesium", *Acta Metallurgica*, 1961, vol. 9, pp. 614-617.

TH-1394_09610307

93 H. Conrad, *Journal of Metals,* 1964, pp. 582.

94 J.J. Holmes, "The activation energies for creep of zircaloy-2", *Journal of Nuclear Materials*, 1964, vol. 13, pp. 137-141.

95 M.J. Klein and M.E. Gulden, "The activation energy for creep of columbium (niobium)", *Metallurgical Transactions*, 1973, vol. 4, pp. 2175-2180.

96 R.W. Lund and W.D. Nix, "On high creep activation energies for dispersion strengthened metals", *Metallurgical and Materials Transactions A,* 1975, vol. 6, pp. 1329-1333.

97 S. Purushothaman and J. Tien, "Role of back stress in the creep behavior of particle strengthened alloys", *Acta Metallurgica,* 1978, vol. 26, pp. 519-528.

98 S. Ig Hong, "Influence of dynamic strain aging on the apparent activation energy for creep", *Materials Science and Engineering*, 1984, vol. 64, pp. L19-L21.

99 S. Ig Hong, "On the creep activation energies of alloys", *Materials Science and Engineering*, 1987, vol. 86, pp. 211-218.

100 V. Buršíková, J. Buršík, V. Navrátil and K. Milička, "Creep behaviour of leaded brass", *Materials Science and Engineering A,* 2002, vol. 324, pp. 235-238.

101 S.N. Zhurkov and T.P. Sanfirova, *Soviet Physics-Technical Physics*, 1959, vol. 3, pp. 1586.

102 S.V. Raj, "Tensile creep of polycrystalline near-stoichiometric NiAl", *Materials Science and Engineering A,* 2003, vol. 356, pp. 283-297.

103 C.R. Barrett, A.J. Ardell and O.D. Sherby, "Influence of modulus on the temperature dependence of the activation energy for creep at high temperature", *Transaction Metallurgical Society of AIME*, 1964, vol. 230, pp. 200-204.

104 T.A. Trozera, O.D. Sherby and J.E. Dorn, "Effect of strain rate and temperature on the plastic deformation of high purity aluminum", *Transactions ASM*, 1957, vol. 49, pp. 173-188.

105 Y. Jingli, S. Yangshan, X. Feng, X. Shan, X. Yingying and T. Weijian, "Creep behavior of Mg-2wt.%Nd binary alloy", *Materials Science and Engineering A,* 2009, vol. 524, pp. 102-107.

106 A.R. Kaufman, P. Gordon and D.W. Lillie, *Transactions ASM,* 1950, vol. 42, pp. 785.

107 O.D. Sherby and J.E. Dorn, "The creep properties of cold rolled aluminium alloy sheet metals", *Transactions ASM*, 1951, vol. 43, pp. 611.

108 O.D. Sherby and J.E. Dorn, "Creep correlations in alpha solutions of aluminium", *Transactions AIME,* 1952, vol. 194, pp. 959-964.

109 R.L. Orr, O.D. Sherby and J.E. Dorn, "Correlations of rupture data for metals at elevated temperature", *Transactions ASM*, 1954, vol. 46, pp. 113-128.

110 I.A. Servi and N.J. Grant, "Creep and stress-rupture behavior of aluminum as a function of purity", *Journal of Metals, AIME*, 1951, vol. 3, pp. 909-916.

TH-1394_09610307

111 F.B. Cuff and N.J. Grant, Iron Age, 1952, pp. 134.

112 T.H. Hazlett, E.R. Parker and M.W. Nathans, "Determination of Activation & Energies for Secondary Creep", Institute of Engineering Research Report, University of California, Berkeley, Series No. 28, Issue No. 8, 1950.

113 A. Nadai and M.J. Manjoine, "High Speed Tension Tests at Elevated Temperatures", *Transactions ASME*, 1941, vol. 63, pp. A-77.

114 R.C. Grassi, D.W. Bainbridge and J.W. Harman, US Atomic Energy Commission Publication No. AECU 2 201, 1952.

115 D. Park, S. Hong, K. Lee, M. Huh, J. Suh, S. Lee and W. Jung, "High temperature creep behaviour and microstructural evolution of an 18Cr9Ni3CuNbVN austenitic stainless steel", *Materials Characterization*, 2014, vol. 93, pp. 52-61.

116 F.V. Tahamia, A.H. Daei-Sorkhabia and F.R. Biglari, "Creep constitutive equations for cold-drawn 304L stainless steel", *Materials Science and Engineering A*, 2010, vol. 527, pp. 4993-4999.

117 A.K. Raj, "On high-temperature materials: a case on creep and oxidation of a fully austenitic heat-resistant superalloy stainless steel sheet", *Journal of Materials*, 2013, vol. 2013 pp. 1-6.

118 T. Yamane, N. Genma and Y. Takahashi, "Creep behaviour of a 25wt % Cr-20wt % Ni austenitic stainless steel doped with antimony", *Journal of Materials Science*, 1984, vol. 19, pp. 263-269.

119 O.A. Ruano, J. Wadsworth and O.D. Sherby, "Deformation mechanisms in an austenitic stainless steel (25Cr-20Ni) at elevated temperature", *Journal of Materials Science*, 1985, vol. 20, pp. 3735-3744.

120 S. Holmström, "Engineering tools for robust creep modeling", Ph.D. thesis, The Aalto University School of Science and Technology, Aalto University, Finland, 2010.

121 D. Alessio, G. Gonzalez, V.F. Pirrone, L. Iurman and L. Moro, "Variation of creep properties in HP steel by influence of temperature", *Procedia Materials Science*, 2012, vol. 1, pp. 104-109.

122 J. Harper and J.E.Dorn, "Viscous creep of aluminum near its melting temperature. Theory of steady-state creep based on dislocation climb", *Acta Metallurgica*, 1957, vol. 5, pp. 654-665.

123 R.L. Coble, "A model for boundary diffusion controlled creep in polycrystalline materials", *Journal of Applied Physics*, 1963, vol. 34, pp. 1679-1682.

124 F.A. Mohamed and T.G. Langdon, "The transition from dislocation climb to viscous glide in creep of solid solution alloys", *Acta Metallurgica*, 1974, vol. 22, pp. 779-788.

125 F.A. Mohamed and T.G. Langdon, "Deformation mechanism maps based on grain size", *Metallurgical Transactions*, 1974, vol. 5, pp. 2339-2345.

TH-1394_09610307

126 T.G. Langdon, Deformation of polycrystals: mechanisms and microstructures, N. Hansen, A. Horsewell, T. Leffers and H. Lilholt (eds.), Rise National Laboratory, Roskilde, Denmark, l981, pp. 45.

127 P. Yavari and T.G. Langdon, "An examination of the breakdown in creep by viscous glide in solid solution alloys at high stress levels", *Acta Metallurgica*, 1982, vol. 30 pp. 2181-2196.

128 R.L. Stocker and M.F. Ashby, "On the empirical constants in the Dorn equation", *Scripta Metallurgica*, 1973, vol. 7, pp. 115-120.

129 S.S. Bhattacharya, G.V. Satishnarayana and K.A. Padmanabhan, "A generic analysis for high-temperature power-law deformation: the case of linear ln(strain rate)-ln(stress) relationship", *Journal of Materials Science*, 1995, vol. 30, pp. 5850-5866.

130 A. Iost, "The correlation between the power-law coefficients in creep: the temperature dependence", *Journal of Materials Science*, 1998, vol. 33, pp. 3201-3206.

131 M.F. Ashby, "A first report on deformation-mechanism maps", *Acta Metallurgica*, 1972, vol. 20, pp. 887-897.

132 F.A. Mohamed and T.G. Langdon, "Deformation mechanism maps based on grain size", *Metallurgical Transactions*, 1974, vol. 5, pp. 2339-2345.

133 F.A. Mohamed and T.G. Langdon, "The transition from dislocation climb to viscous glide in creep of solid solution alloys", *Acta Metallurgica*, 1974, vol. 22, pp. 779-788.

134 R.N. Singh, "Application of deformation-mechanism maps to the study of in-reactor behavior of carbide fuels", *Journal of Nuclear Materials*, 1977, vol. 64, pp. 167-173.

135 P.M. Sargent and M.F. Ashby, "Deformation-mechanism maps for silicon carbides", *Scripta Metallurgica*, 1983, vol.17, pp. 951-957.

136 P.M. Sargent, G. Malakondaiah and M.F. Ashby, "A deformation map for cobalt", *Scripta Metallurgica*, 1983, vol.17, pp. 625-629.

137 P.M. Sargent and M.F. Ashby, "Deformation mechanism maps for alkali metals", *Scripta Metallurgica*, 1984, vol.18, pp. 145-150.

138 P.M. Sargent and M.F. Ashby, "A deformation mechanism map for a III-V compound, indium antimonide", *Scripta Metallurgica*, 1984, vol.18, pp. 219-224.

139 J. A. Carey, P.M. Sargent, D.R.H. Jones, "A deformation mechanism map for IN738LC superalloy", *Journal of Materials Science Letters*, 1990, vol. 9, pp. 572-575.

140 H.J. Frost and M.F. Ashby, Deformation mechanism maps, Pergamon Press, Oxford, U.K., 1982.

TH-1394_09610307

141 N. Bonora and L. Esposito, "Mechanism based creep model incorporating damage", *Journal of Engineering Materials and Technology*, 2010, vol. 132, pp. 1-7.

142 M.E. Kassner and T.A. Hayes, "Creep cavitation in metals", *International Journal of Plasticity*, 2003, vol. 19, pp. 1715-1748.

143 M.F. Ashby, C. Gandhi and D.M.R. Taplin, "Fracture-mechanism maps and their construction for f.c.c. metals and alloys", *Acta Metallurgica*, 1979, vol. 27, pp. 666-729.

144 F.C. Monkman and N.J. Grant, "An empirical relationship between rupture life and minimum creep rate in creep rupture tests", *Proceeding ASTM*, 1956, vol. 56, pp. 593-620.

145 V. Gaffard, J. Besson and A.F. Gourgues-Lorenzon, "Creep failure model of a tempered martensitic stainless steel integrating multiple deformation and damage mechanisms", *International Journal of Fracture*, 2005, vol. 133, pp. 139-166.

146 W.G. Kim, S.H. Kim and W.S. Ryu, "Evaluation of Monkman-Grant parameters for type 316LN and modified 9Cr-Mo stainless steels", *KSME International Journal*, 2002, vol. 16, pp. 1420-1427.

147 E.I. Samuel, B.K. Choudhary, D.P. Rao Palaparti and M.D. Mathew, "Creep deformation and rupture behaviour of P92 steel at 923 K", *Procedia Engineering*, 2013, vol. 55, pp. 64-69.

148 B. Michel, "Formulation of a new intergranular creep damage model for austenitic stainless steels", *Nuclear Engineering and Design*, 2004, vol. 227, pp. 161-174.

149 W.G. Kim, D.W. Kim, W.S. Ryu, "Applicability of Monkman-Grant relationships to type 316L(N) stainless steel", *Transactions of the Korean Society of Mechanical Engineers A*, 2000, vol. 24, pp. 2326-2333.

150 J. Cadek, Creep in metallic materials, Elsevier, Amsterdam, 1988.

151 E.H. Toscano and M. Bocek, "Relationship between strain rate, strain to failure and life time", *Journal of Nuclear Materials*, 1981, vol. 96, pp. 29-36.

152 F. Dobes and K. Milicka, "The relation between minimum creep rate and time to fracture", *Metal Science*, 1976, vol. 10, pp. 382-384.

153 A. Baldan, "Effects of carbides and cavitation on the Monkman-Grant ductility of a nickel-base superalloy", *Journal of Materials Science Letters*, 1992, vol. 11, pp. 1315-1318.

154 F. Povolo, "Comments on the Monkman-Grant and the modified Monkman-Grant relationships", *Journal of Materials Science*, 1985, vol. 20, pp. 2005-2010.

155 D.C. Dunand, B.Q. Han and A.M. Jannsen, "Monkman-Grant analysis of creep fracture in dispersion-strengthened and particulate-reinforced aluminum", *Metallurgical and Materials Transactions A*, 1999, vol. 30, pp. 829-838.

TH-1394_09610307

156 H.J. Ryu, Y.S. Kim and A.M. Yacout, "Thermal creep modeling of HT9 steel for fast reactor applications", *Journal of Nuclear Materials*, 2011, vol. 409, pp. 207-213.

157 C. Phaniraj, B.K. Choudhary, K.B.S. Rao and B. Raj, "Relationship between time to reach Monkman–Grant ductility and rupture life", *Scripta Materialia*, 2003, vol. 48, pp. 1313-1318.

158 V.M. Radhakrishnan, "The relationship between minimum creep rate and rupture time in Cr-Mo steels", *Journal of Materials Engineering and Performance*, 1992, vol. 1, pp. 123-128.

159 B.K. Choudhary, C. Phaniraj, K.B.S. Rao and S.L. Mannan, "Creep deformation behavior and kinetic aspects of 9Cr-1Mo ferritic steel", *ISIJ International*, 2001, vol. 41, pp. S73-S80.

160 F. Dobeš and K. Milička, "On the Monkman-Grant relation for small punch test data", *Materials Science and Engineering A*, 2002, vol. 336, pp. 245-248.

161 A.K. Ray, K. Diwakar, B.N. Prasad, Y.N. Tiwari, R.N. Ghosh and J.D. Whittenberger, "Long term creep-rupture behaviour of 813 K exposed 2.25-1Mo steel between 773 and 873 K", *Materials Science and Engineering A*, 2007, vol. 454-455, pp. 124-131.

162 B.K. Choudhary, C. Phaniraj and B. Raj, "Interesting relationships for creep deformation and damage and their applicability for 9Cr-1Mo ferritic steel", *Transactions of the Indian Institute of Metals*, 2010, vol. 63, pp. 675-680.

163 B.K. Choudhary and E.I. Samuel, "Creep behaviour of modified 9Cr-1Mo ferritic steel", *Journal of Nuclear Materials*, 2011, vol. 412, pp. 82-89.

164 B.K. Choudhary, "Tertiary creep behaviour of 9Cr-1Mo ferritic steel", *Materials Science and Engineering A*, 2013, vol. 585, pp. 1-9.

165 H.O. Ali and M.N. Tamin, "Modified Monkman-Grant relationship for austenitic stainless steel foils", *Journal of Nuclear Materials*, 2013, vol. 433, pp. 74-79.

166 G. Sundararajan, "The Monkman-Grant relationship", *Materials Science and Engineering A*, 1989, vol. 112, pp. 205-214.

167 C. Phaniraj, M. Nandagopal, S.L. Mannan and P. Rodriguez, "The relationship between transient and steady state creep in AISI 304 stainless steel", *Acta Materialia*, 1991, vol. 39, pp. 1651-1656.

168 C. Phaniraj, M. Nandagopal, S.L. Mannan, P. Rodriguez, B.P. Kashyap, "Analysis of first order kinetics for tertiary creep in AISI 304 stainless steel", *Acta Materialia*, 1996, vol. 44, pp. 4059-4069.

169 B.K. Choudhary, C. Phaniraj, K.B.S. Rao and S.L. Mannan, "Transient creep behaviour of forged thick section 9Cr-1Mo ferritic steel", *Key Engineering Materials*, 1999, vol. 171-174, pp. 437-444.

TH-1394_09610307

170 C. Phaniraj, B.K. Choudhary, B. Raj and K.B.S. Rao, "A critical damage criterion for creeping solids", *Journal of Materials Science*, 2005, vol. 40, pp. 2561-2564.

171 M.F. Ashby and B.F. Dyson, Valluri et al., editors. Advances in Fracture Research, Pergamon Press, Oxford, 1984, pp. 3-30.

172 B.F. Dyson and T.B. Gibbons, "Tertiary creep in nickel-base superalloys: analysis of experimental data and theoretical synthesis", *Acta Metallurgica*, 1987, vol. 35, pp. 2355-2369.

173 F.A. Leckie and D.R. Hayhurst, "Creep rupture of structures", *Proceedings of the Royal Society London A*, 1974, vol. 340, pp. 323-347.

174 F.A. Leckie and D.R. Hayhurst, "Constitutive equations for creep rupture", *Acta Metallurgica*, 1977, vol. 25, pp. 1059-1070.

175 F.A. Leckie and D.R. Hayhurst, "The damage concept in creep mechanics", *Mechanics Research Communications*, 1975, vol. 2, pp. 23-26.

176 B.J. Cane, "Remaining creep life estimation by strain assessment on plant", *International Journal of Pressure Vessels and Piping*, 1982, vol. 10, pp. 11-30.

177 I.W. Goodall, R.D.H. Cockroft and E.J. Chubb, "An approximate description of the creep rupture of structures", *International Journal of Mechanical Sciences*, 1975, vol. 17, pp. 351-360.

178 J.H. Hollomon and L.D. Jaffe, "Time-temperature relation in tempering steel", *Transactions AIMME*, 1945, vol. 162, pp. 223-249.

179 B. Wilshire and P.J. Scharning, "Creep and creep fracture of commercial aluminium alloys", *Journal of Materials Science*, 2008, vol. 43, pp. 3992-4000.

180 J.F.R. Sobrinho and L. de O. Bueno, "Correlation between creep and hot tensile behaviour for 2.25Cr-1Mo steel from 500ºC to 700ºC. Part 2: An assessment according to different parameterization methodologies", *Revista Matéria*, 2005, vol. 10, pp. 463-471.

181 A.R. Nicoll, "The Larson-Miller C constant as applied to a cobalt-based directionally solidified eutectic alloy", *Journal of Materials Science*, 1979, vol. 14, pp.1759-1761.

182 A.K. Koul, "Larson-Miller parameter and its modified version", *Scripta Matallurgica*, 1982, vol. 16, pp. 947-950.

183 A.K. Koul, and W. Wallace, "A note on the microstructural dependence of creep strength in incone1 700", *Metallurgical Transactions A*, 1982, vol. 13, pp. 673-675.

184 Y. Kadoya, T. Goto, S. Date, T. Yamauchi, T. Saida and T. Sada, "Assessment of remaining life of fossil power plant parts by means of a miniature creep rupture test", *ISIJ International*, 1990, vol. 30, pp. 854-861.

185 Y. Sugita, Y. Kato, T. Yokoyama, T. Sada, F. Sasuyama and N. Nishimura, "Evaluation of creep damage progress by metallurgical examination in aged power boiler pressure parts", *ISIJ International*, 1990, vol. 30, pp. 895-904.

TH-1394_09610307

186 M. Nakashiro, S. Kihara, F. Kishimoto and T. Fujimor, "Evaluation of long term creep strength of 2.25Cr-1Mo heat transfer tube in actual service stress level range", *ISIJ International*, 1990, vol. 30, pp. 823-828.

187 T. Fujita, "Current progress in advanced high Cr ferritic steels for high-temperature applications", *ISIJ International*, 1992, vol. 32, pp. 175-181.

188 M. Vasudevan, S. Venkadesan, P.V. Sivaprasad and S.L. Mannan, "Use of the Larson-Miller parameter to study the influence of ageing on the hardness of cold-worked austenitic stainless steel", *Journal of Nuclear Materials*, 1994, vol. 211, pp. 251-255.

189 S. Deng and R. Warren, "Creep properties of single crystal oxides evaluated by a Larson-Miller procedure", *Journal of the European Ceramic Society*, 1995, vol. 15, pp. 513-520.

190 Y. Harada, Y. Maruyama, A. Maeda, E. Chino, H. Shibazaki, T. Kudo, A. Hidaka, K. Hashimoto and J. Sugimoto, "Evaluation of high temperature tensile and creep properties of light water reactor coolant piping materials for severe accident analyses", *Journal of Nuclear Science and Technology*, 2000, vol. 37, pp. 518-529.

191 A.K. Ray and J.D. Whittenberger, "Stress rupture behavior of a thermal barrier coated AE 437A Ni-based superalloy used for aero turbine blades", *Materials Science and Engineering A*, 2009, vol. 509, pp. 111-114.

192 F.T. Furillo, S. Purushothaman and J.K. Tien, "Further discussion on "Understanding the Larson-Miller parameter", *Scripta Matallurgica*, 1978, vol. 12, pp. 331-332.

193 E.R. Buchanan and L.A. Tarshis, "Strengths and failure mechanisms of a Co-15Cr-13TaC directionally solidified eutectic alloy", *Metallurgical Transactions*, 1974, vol. 5, pp. 1413-1422.

194 H.J. Kim, "Assessment of creep life fraction for in-service high-temperature components", *Engineering Failure Analysis*, 2005, vol. 12, pp. 578-585.

195 B.M. Shlyakman, O.N. Yampolskii and D.V. Ratushev, "A method for determining constant C in the Hollomon parameter", *Metal Science and Heat Treatment*, 2010, vol. 52, pp. 451-453.

196 J.H. Hollomon and Jaffe, L. D., "Time – temperature relation in tempering steel", *Transactions of the American Institute of Mining and Metallurgical Engineers*, vol.162 (1945) pp.223 – 249.

197 R.C. Yang, K. Chen, H.X. Feng and H. Wang, "Determination and application of Larson-Miller parameter for heat resistant steel 12Cr1MoV and 15CrMo", *Acta Metallurgica Sinica*, 2004, vol. 17, pp. 471-476.

198 R.C. Yang, Z. Li and K. Chen, "Research on physical significance of the Larson-Miller parameter and its electron theory for heat-resistant steels", *Key Engineering Materials*, 2007, vol. 353-358, pp. 477-480.

TH-1394_09610307

199 J. Zhao, S. Han, H. Gao and L. Wang, "Remaining life assessment of a CrMoV steel using the Z-parameter method", *International Journal of Pressure Vessels and Piping*, 2004, vol. 81, pp. 757-760.

200 J. Zhao, D. Li, J. Zhang, W. Feng and Y. Fang, "Introduction of SCRI model for creep rupture life assessment", *International Journal of Pressure Vessels and Piping*, 2009, vol. 86, pp. 599-603.

201 L. Xing, J. Zhao, F. Sheng and W. Feng, "Z-parameter method for damage evaluation in HK40 steel", *Journal of Materials Science & Technology*, 2007, vol. 23, pp. 329-332.

202 W.G. Kim, J.Y. Park, S.J. Kim and J. Jang, "Reliability assessment of creep rupture life for Gr. 91 steel", *Materials & Design*, 2013, vol. 51, pp. 1045-1051.

203 W.G. Kim, J.Y. Park, B.K. Choudhary, S.J. Kim, M.H. Kim and J. Jang, "Influence of data size on the reliability assessment of creep life of grade 91 steel", *Journal of Mechanical Science and Technology*, 2014, vol. 28, pp. 4493-4501.

204 A.K. Ray, S.K. Sinha, Y.N. Tiwari, J. Swaminathan, G. Das, S. Chaudhuri and R. Singh, "Analysis of failed reformer tubes", *Engineering Failure Analysis*, 2003, vol. 10, pp. 351-362.

205 B. Shannon and C. Jaske, "A comprehensive approach to reformer tube inspection and assessment", 2nd Middle East Non-destructive Testing Proceedings, Saudi Arabia, vol. 9, 2003.

206 S.A.J. Jahromi and M. Naghi Khani, "Creep life assessment of primary reformer HP40-Nb modified steel tube of an ammonia plant", *IJE Transactions B: Applications*, 2004, vol. 17, pp. 183-190.

207 M.T. Hagan and M.B. Menhaj, "Training feed forward networks with the Marquardt algorithm", *IEEE Transactions on Neural Networks*, 1994, vol. 5, pp. 989-993.

208 J. Jones and D.J.C. MacKay, "Neural network modeling of the mechanical properties of Ni based superalloys", 8th International Symposium on Superalloys, Seven Springs, Pennsylvania, USA, 1996, pp. 417-424.

209 H.K.D.H. Bhadeshia, "Neural networks in materials science", *ISIJ International*, 1999, vol. 39, pp. 966-979.

210 C. Dumortier and P. Lehert, "Statistical modelling of mechanical tensile properties of steels by using neural networks and multivariate data analysis", Neural Networks in Materials Science, *ISIJ International*, 1999, vol. 39, pp. 980-985.

211 S. Datta, J. Sil and M.K. Banerjee, "Petri neural network model for the effect of controlled thermomechanical process parameters on the mechanical properties of HSLA steels", Neural Networks in Materials Science, *ISIJ International*, 1999, vol. 39, pp. 986-990.

TH-1394_09610307

212 J. Warde and D.M. Knowles, "Application of neural networks to mechanical property determination of Ni based superalloys", *ISIJ International*, 1999, vol. 39, pp. 1006-1014.

213 J. Warde and D.M. Knowles, "Use of neural networks for alloy design", *ISIJ International*, 1999, vol. 39, pp. 1015-1019.

214 Y. Huang and P.L. Blackwell, "Prediction of mechanical properties of superplastic Inconel 718 using artificial neural networks", *Materials Science and Technology*, 2002, vol. 18, pp. 1104-1108.

215 M.E. Haque and K.V. Sudhakar, "ANN back-propagation prediction model for fracture toughness in microalloy steel", *International Journal of Fatigue*, 2002, vol. 24, pp. 1003-1010.

216 M.B. Esfahani, M.R. Toroghinejad and S. Abbasi, "Artificial neural network modeling the tensile strength of hot strip mill products", *ISIJ International*, 2009, vol. 49, pp. 1583-1587.

217 M.A. Yescas, "Prediction of the Vickers hardness austempered ductile irons using neural network", *International Journal of Cast Metals Research*, 2003, vol. 15, pp. 513-521.

218 A.M. Hassan, A. Alrashdan, M.T. Hayajneh and A.T. Mayyas, "Prediction of density, porosity and hardness in aluminum-copper-based composite materials using artificial neural network", *Journal of Materials Processing Technology*, 2009, vol. 209, pp. 894-899.

219 M. Evans, "Method for improving parametric creep rupture life of 2.25Cr-1Mo steel using artificial neural networks", *Materials Science and Technology*, 1999, vol. 15, pp. 647-658.

220 Y.S. Yoo, C.Y. Jo and C.N. Jones, "Compositional prediction of creep rupture life of single crystal Ni base superalloy by Bayesian neural network", *Materials Science and Engineering A*, 2002, vol. 336, pp. 22-29.

221 Y.S. Yoo, I.S. Kim, D.H. Kim, C.Y. Jo, H.M. Kim and C.N. Jones, "The application of neural network to the development of single crystal superalloys", *Superalloys 2004*, 2004, pp. 942-950.

222 N. Wang, S.T. Tu and F.Z. Xuan, "A novel prediction method of creep rupture life of 9-12% chromium ferritic steel based on abductive network", *Engineering Failure Analysis*, 2013, vol. 31, pp. 302-310.

223 O. Frolova, E. Roos, K. Maile and W. Müller, "Representation of the heat specific creep rupture behaviour of 9% Cr steels using neural networks", *Transactions on Machine Learning and Data Mining*, 2011, vol. 4, pp. 1-16.

224 R.E. Johnston, "Neural networks for critical high temperature component life prediction", *Materials Science and Technology*, 2011, vol. 27, pp. 108-114.

225 M.F.A. Ghafir, Y.G. Li and L. Wang, "Creep life prediction for aero gas turbine hot section component using artificial neural networks", *Journal of Engineering for Gas Turbines and Power*, 2014, vol. 136, pp. 031504-1-031504-9.

TH-1394_09610307

226 S. Chatzidakis, M. Alamaniotis and L.H. Tsoukalas, “Creep rupture forecasting for high performance energy systems”, 5th International Conference on Information, Intelligence, Systems and Applications, IISA 2014, California, USA, 2014, pp. 95-99.

227 V.K. Gupta, N. Kwatra and S. Ray, “Artificial neural network modeling of creep behavior in a rotating composite disc”, *Engineering Computations*, 2007, vol. 24, pp. 151-164.

228 A. Sarkar, S.K. Sinha, J.K. Chakravartty and R.K. Sinha, “Artificial neural network modelling of in-reactor diametral creep of Zr2.5%Nb pressure tubes of Indian PHWRs”, *Annals of Nuclear Energy*, 2014, vol. 69, pp. 246-251.

229 S. Surendarnath, K. Sankaranarayanasamy and B. Ravisankar, “Workability study on 99.04% pure aluminium processed by ECAP,” *Materials and Manufacturing Processes*, 2014, vol. 29, pp. 691-696.

230 J. Luo and M.Q. Li, “Strain rate sensitivity and strain hardening exponent during the isothermal compression of Ti60 alloy”, *Materials Science and Engineering A*, 2012, vol. 538, pp. 156-163.

231 P.S. Robi and U.S. Dixit, “Application of neural networks in generating processing map for hot working,” *Journal of Materials Processing Technology*, 2003, vol. 142, pp. 289-294.

232 G.D. Garson, “Interpreting neural-network connection weights”, *Artificial Intelligence Expert*, 1991, vol. 6, pp. 47-51.

233 E.S. Elmolla and M. Chaudhuri, The Use of Artificial Neural Network (ANN) for Modelling, Simulation and Prediction of Advanced Oxidation Process Performance in Recalcitrant Wastewater Treatment, Chapter 6, "Artificial Neural Networks-Application", edited by C.L.P. Hui, ,InTech Europe, Croatia, 2011.

234 J.H. Lee, W.J. Yang, W.D. Yoo and K.S. Cho, “Microstructural and mechanical property changes in HK40 reformer tubes after long term use”, *Engineering Failure Analysis*, 2009, vol. 16, pp.1883-1888.

235 NRIM creep data sheet No. 38A, Data sheets on the elevated temperature properties of centrifugally cast tubes and cast block of 25Cr·35Ni·0.4C steel for reformer furnaces (SCH 24).

236 H39WM 25/35 Cr/Ni Nb 0.4% C microalloy cast heat resisting alloy, Physical properties, Doncasters Paralloy Ltd, UK, 2013.

237 S. Latha, M.D. Mathew, P. Parameswaran, K.B.S. Rao and S.L. Mannan, “Thermal creep properties of alloy D9 stainless steel and 316 stainless steel fuel clad tubes”, *International Journal of Pressure Vessels and Piping*, 2008, vol. 85, pp. 866-870.

238 D.D. Yin, Q.D. Wang, C.J. Boehlert and V. Janik, “Creep and fracture behavior of peak-aged Mg-11Y-5Gd-2Zn-0.5Zr (wtpct)”, *Metallurgical and Materials Transactions A*, 2012, vol. 43, pp. 3338-3350.

TH-1394_09610307

239 K. Singh and M. Kamaraj, "Creep ductility of 1Cr1Mo1/4V low alloy forging and casting steels", *Materials Science and Engineering A*, 2009, vol. 510-511, pp. 51-57.

240 K. Singh and M. Kamaraj, "Creep ductility evaluation of low alloy steels used for steam turbine components", *Transactions of The Indian Institute of Metals*, 2010, vol. 63, pp. 391-395.

241 P.W. Davies and K.R. Williams, "Recovery measurements during tertiary creep of α-iron", *Acta Metallurgica*, 1969, vol. 17, pp. 897-903.

242 ASME Boiler and Pressure Vessel Code, Section VIII, Division 1 and Section III, Division 1, Subsection NH, Class I Components in Elevated Temperatures Service, 2001.

243 D.A. Woodford, ASM Handbook Materials selection and design, 20, ASM International, Metals Park, Ohio, USA, 1997, pp. 573.

244 X. Zhou, Y. Liu, C. Liu and B. Ning, "Evolution of creep damage in a modified ferritic heat resistant steel with excellent short-term creep performance and its oxide layer characteristic", *Materials Science and Engineering A*, 2014, vol. 608, pp.46-52.

245 V. Sklenička, K. Kuchařová, M. Svoboda, L. Kloc, J. Buršík and A. Kroupa, "Long-term creep behavior of 9-12%Cr power plant steels", *Materials Characterization*, 2003, vol. 51, pp.35-48.

246 V.T. Ha and W.S. Jung, "Effects of heat treatment processes on microstructure and creep properties of a high nitrogen 15Cr-15Ni austenitic heat resistant stainless steel", *Materials Science and Engineering A*, 2011, vol. 528, pp.7115-7123.

TH-1394_09610307

Appendix-I

Larson-Miller parameter

In 1952, F.R. Larson and J. Miller proposed that creep rate adequately governed by the Arrhenius type equation i.e.

$$\dot{\varepsilon} = A_0 \, exp\left(-\frac{Q_c}{RT}\right) \tag{I.1}$$

where $\dot{\varepsilon}$ is the minimum creep rate or the rate at a constant strain, A_0 is a constant, R is the universal gas constant, T is the absolute temperature, Q_c is the activation energy for the creep process.

Since, the rupture time depends on the creep rate by $t_r \left(\frac{d\varepsilon}{dt}\right)_{\min}$ = constant, the Eq. I.1 may be written

$$\frac{1}{t_r} = A_0 \, exp\left(-\frac{Q_c}{RT}\right) \tag{I.2}$$

where t_r is the time to rupture.

Taking the natural logarithm of both sides of Eq. I.2

$$-\ln(t_r) = \ln(A_0) - \frac{Q_c}{RT} \tag{I.3}$$

With some rearrangement

$$\frac{Q_c}{R} = T(\ln(A_0) + \ln(t_r)) \tag{I.4}$$

The final relation becomes

$$T(\mathrm{C}_{L-M} + \log_{10}(t_r)) = \frac{Q_c}{2.3R} = P_{L\text{-}M} = \text{Constant (for constant stress)} \tag{I.5}$$

where $C_{L\text{-}M} = \log_{10}(A_0)$ = constant and $P_{L\text{-}M}$ is Larson-Miller parameter.

TH-1394_09610307

Appendix-II

Manson – Haferd parameter

In 1953, S.S. Manson and A.M. Haferd proposed a parametric technique based on the assumption that the temperature T depends on time to rupture t_r which follows an exponential relation in the form

$$t_r = A_1 \exp(Q_c T) \tag{II.1}$$

where A_1 is a constant and Q_c is a stress dependent function. Taking the common logarithm of both sides of Eq. II.1

$$\log_{10}(t_r) = \log_{10}(A_1) + \left(\frac{Q_c T}{2.3}\right) \tag{II.2}$$

Since, iso-stress plots of $\log_{10}(t_r)$ vs. T intersect at a fixed point given by T_a and $\log_{10}(t_a)$,

$$\log_{10}(t_a) = \log_{10}(A_1) + \left(\frac{Q_c T_a}{2.3}\right) \tag{II.3}$$

On subtracting Eq. (II.3) from Eq. (II.2) and with some simplifications one obtain

$$\log_{10}(t_r) - \log_{10}(t_a) = \frac{Q_c}{2.3}(T - T_a) \tag{II.4}$$

The final relation becomes

$$\frac{(T-T_a)}{\log_{10}(t_r)-\log_{10}(t_a)} = \frac{Q_c}{2.3} = P_{M\text{-}H} = \text{Constant} \tag{II.4}$$

where $P_{M\text{-}H}$ is Manson-Haferd parameter.

TH-1394_09610307

Appendix-III

Orr-Sherby-Dorn parameter

In 1954, R.L. Orr, O.D. Sherby and J.E. Dorn proposed a parametric technique based on Arrhenius type equation i.e.

$$\dot{\varepsilon}_s = A_2 \, exp\left(-\frac{Q_c}{RT}\right) \tag{III.1}$$

where $\dot{\varepsilon}_s$ is the minimum creep rate, A_2 is a constant, R is the universal gas constant, T is the absolute temperature, Q_c is the activation energy for the creep process.

Since, the rupture time inversely proportional with minimum creep rate by $\left(t_r \propto \frac{1}{\dot{\varepsilon}_s}\right)$, the Eq. III.1 may be written

$$t_r = A_3 \, exp\left(\frac{Q_c}{RT}\right) \tag{III.2}$$

where t_r is the time to rupture and A_3=1/A_2.

Taking the common logarithm of both sides of Eq. III.2

$$\log_{10}(t_r) = \log_{10}(A_3) + \left(\frac{Q_c}{2.3RT}\right) \tag{III.3}$$

With some rearrangement

$$\log_{10}(A_3) = \log_{10}(t_r) - \frac{Q_c}{2.3RT} \tag{III.4}$$

The final relation becomes

$$\log_{10}(t_r) - \frac{Q_c}{2.3RT} = P_{O\text{-}S\text{-}D} \tag{III.5}$$

where $P_{O\text{-}S\text{-}D}$ is Orr-Sherby-Dorn parameter.

TH-1394_09610307

Appendix-IV

Calculations of the spring constants

Spring unit for constant stresses 47 MPa, 68MPa and 80 MPa was calibrated. At the starting of each calibration test, the top plate was kept at a position by rotating power screw nut where maximum load acting on a specimen for zero displacement of gauge length. Displacement of the top plate was measured from a reference point. By reverse rotation of the nut, load was released by spring as well as on specimen and top plate came down. For each millimeter displacement load was noted from the load indicator. Maximum percentage deviation and RMS error for 47 MPa, 68MPa and 80 MPa are given in Table IV.1.

Table IV.1. Spring stiffness, percentage deviation and RMS error for different stresses.

True Stress (MPa)	Spring stiffness (N/mm)	Maximum deviation (%)	RMS error (N)
47	22.4	+2.34 -3.13	1.64
68	33.7	+1.66 -2.70	14.39
80	42	+4.40 -6.28	46.26

The creep apparatus was commissioned by creep test at for stresses of 68 MPa and 80 MPa at 650 °C and 860 °C respectively. The creep tests were performed on mild steel and 316 stainless steel sample respectively. Creep tests were performed following the procedure described above. Load vs. displacement of gauge length for both the tests are shown in Figure IV.1a. Maximum percentage deviation and RMS error of the creep test were determined and given in Table IV.2. The values of percentage deviation and RMS error indicate that the apparatus shows an acceptable result for creep testing. Figure IV.1b shows the creep curve obtained from these two creep test.

TH-1394_09610307

Table IV.2. Percentage deviation and RSM error for the low stress apparatus.

True stress (MPa)	Temperature (°C)	Maximum deviation (%)	RMS error (N)
68	650	+ 0.9 - 0.8	3.9
80	860	+ 0.3 - 0.6	3.9

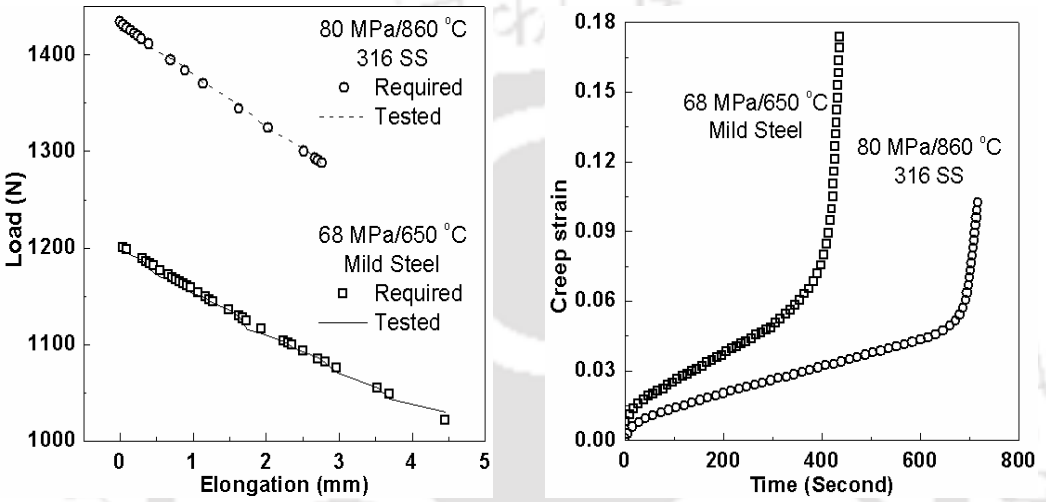

(a) (b)

Figure IV.1. (a) Load vs. displacement plot and (b) creep curve tested at 68 MPa/650 ˚C of mild steel and 80 MPa/860 °C of 316 SS sample.

TH-1394_09610307

Appendix-V

Design of modified creep set-up

The non-linear behavior of the load vs. elongation plot is taken care of by using a set of inclined tension springs. The schematic diagram of the inclined spring arrangement is shown in Figure V.1(a). In this case, the spring force $F_v(x)$ is a nonlinear function of the displacement variable x as shown in the free body diagram (Figure V.1(b)). One end of the springs is attached to the top circular plate through pin joints. The other ends of the springs are attached to a bottom plate.

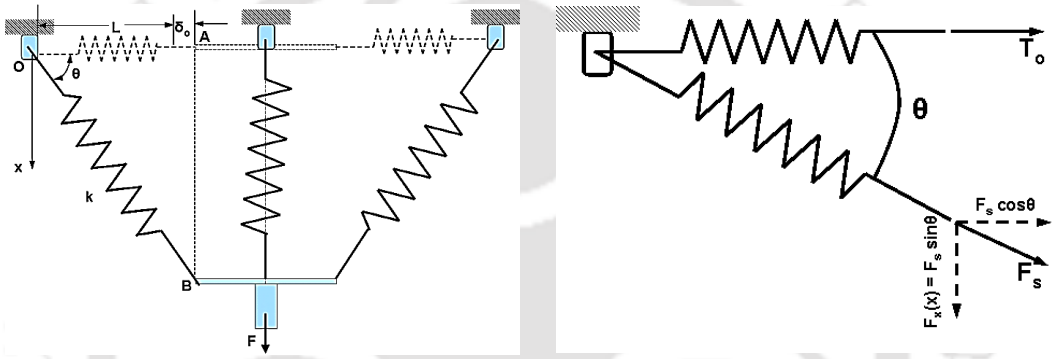

(a) (b)

Figure V.1. Schematic diagram showing the (a) force and displacement of the bottom disc and (b) free body diagram of a single inclined spring.

The total vertical load acting by n_s number of springs is given by,

$$F_v = n_s \times F_s = n_s \times \left[k_s \delta_o \frac{x}{\sqrt{{L_n}^2 - x^2}} + k_s x \left(\frac{\sqrt{{L_n}^2 - x^2} - L_n}{\sqrt{{L_n}^2 - x^2}} \right) \right] \quad \text{(V.1)}$$

Based on the above formulation, load versus elongation of creep specimen for true strains up to 0.45 has been calculated. The gauge length (L_{gauge}) of the specimen is 25 mm and the initial cross–sectional area is 19.5 mm^2.

Different tension springs were purchased from the local market with varying spring dimensions. Stiffness of these springs was measured by carrying out tension test on UTM. The load F_v on the specimen for each millimeter displacements was computed using Eq. V.1 by varying the number of springs (3, 4, and 6 springs) in the setup and with different spring stiffness.

TH-1394_09610307

The deviation of the computed and the required load values were determined for each combination. The percentage deviation error and the root mean square (RMS) error were determined by:

$$\text{Percentage deviation error} = \frac{y_i - x_i}{x_i} \times 100 \tag{V.2}$$

$$Root\ mean\ square\ (RMS) error = \sqrt{\frac{1}{N}\sum_{i=1}^{N}(x_i - y_i)^2} \tag{V.3}$$

where x_i is the required values, y_i is the computed values and N is the number of data. Based on the error norms (minimum percentage error and minimum RMS error), the combination of number of springs and spring stiffness were decided. The stiffness of spring, number of springs, maximum percentage deviation and RMS error for 120 MPa stress were determined for creep testing apparatus and are shown in Table V.1.

Table V.1. Details of spring used for the high stress creep testing apparatus.

True stress (MPa)	Spring stiffness (N/mm)	Number of springs	Maximum % deviation	RMS error (N)
120	59.39	4	+ 1.06 - 2.71	39

The creep apparatus was tested by a creep test at a temperature of 650 °C and stress 120 MPa of mild steel sample. Creep test was performed following normal procedure described early. Variation of load acting on the sample for the creep test with displacement of gauge length is shown in Figure V.2(a). Maximum percentage deviation and RMS error of the creep test was determined as 0.9 % and 13.47 N which are less than the theoretically calculated values given in Table V.1. The plot also indicates that the apparatus shows an acceptable result for creep testing. Figure V.2(b) shows the creep curve obtained from the creep test of mild steel sample at 650 °C and 120 MPa.

TH-1394_09610307

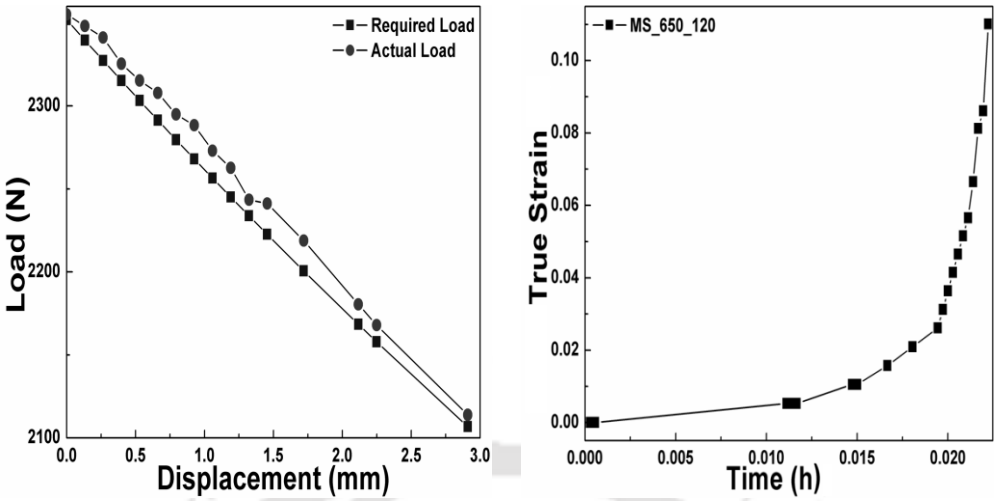

(a) (b)

Figure V.2. (a) Load vs. displacement plot and (b) creep curve of mild steel tested at 650 ˚C/120 MPa.

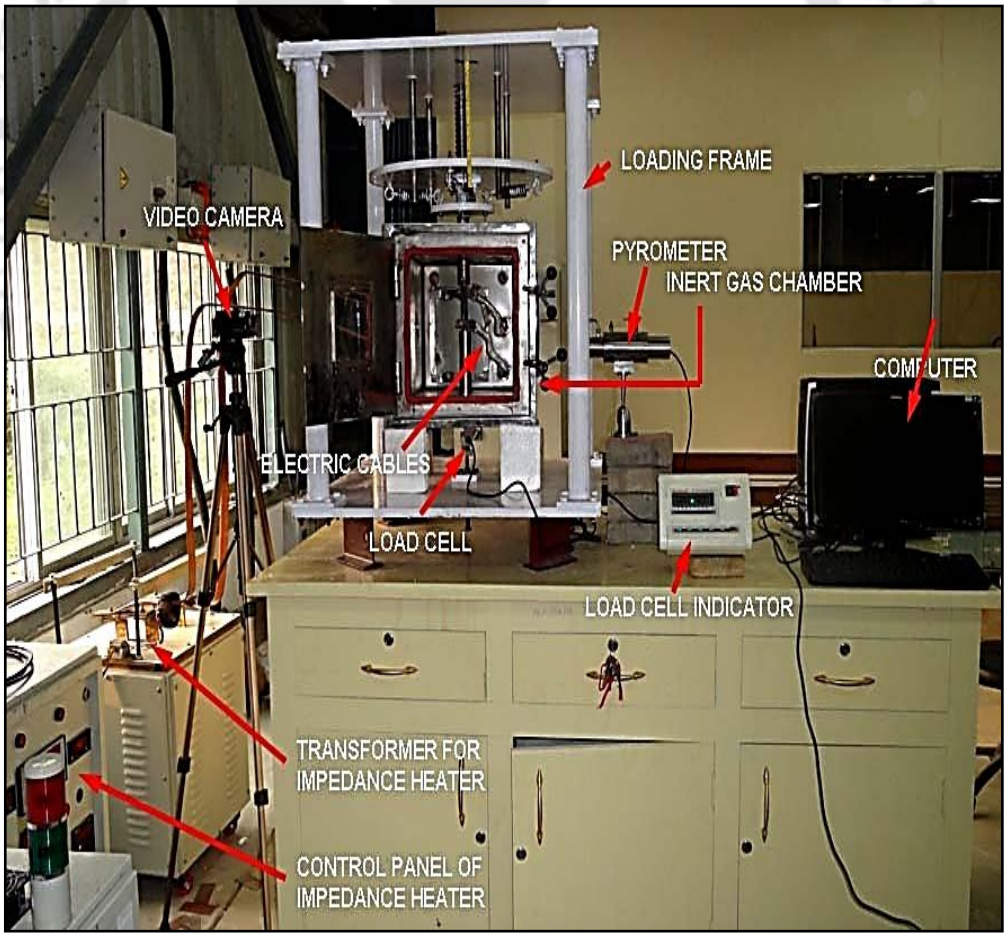

Figure V.3. Arrangement of 120 MPa constant stress creep testing apparatus with impedance heater, pyrometer, load indicator, video camera and inert gas chamber.

TH-1394_09610307

Appendix-VI

Detailed technical specification

(a) Load Cell:

Items	Load Cell
Capacity	500 kg
Model	S – type (34810)
Excitation Voltage	10 VDC - Maximum 15 VDC
Nominal Output / Sensitivity	3.0 mv/v
Non Linearity	<±0.025% FSO
Hysteresis	<±0.02% FSO
Non Repeatability	<±0.01% FSO
Creep(30 Minutes)	<±0.03% FSO
Zero Balance	±1.0% FSO
Input Resistance	392±15 Ohms
Output Resistance	350±3 Ohms
Insulation Resistance	> 1000 Mega Ohms at 50VDC
Safe Overload	150%
Ultimate Overload	250%
Allowable Side Load	50%
Temperature Compensated Range	0°C to +60ºC
Temperature Effect on Output	<0.0015% FSO /ºC
Temperature Effect on Zero	<0.0020% FSO /ºC
Deflection	<0.4mm at FSO
Finish & Construction	Electronic Nickel Plated tool Steel Alloy
Hole Size / Pitch	12 mm & 1.75 mm.
Environment Protection Class	IP67

(b) Digital Indicator:

i) Model: T4

ii) Wall mounting with 6 digit 7 segment LED display

iii) RS 232 compatible output

iv) With Tare / Zero facility

v) Battery Back up

TH-1394_09610307

Appendix-VII

Experimental creep curves

The appendix contains creep curves obtained from the creep tests at elevated temperatures and stresses.

(i) Constant stress of 47 MPa:

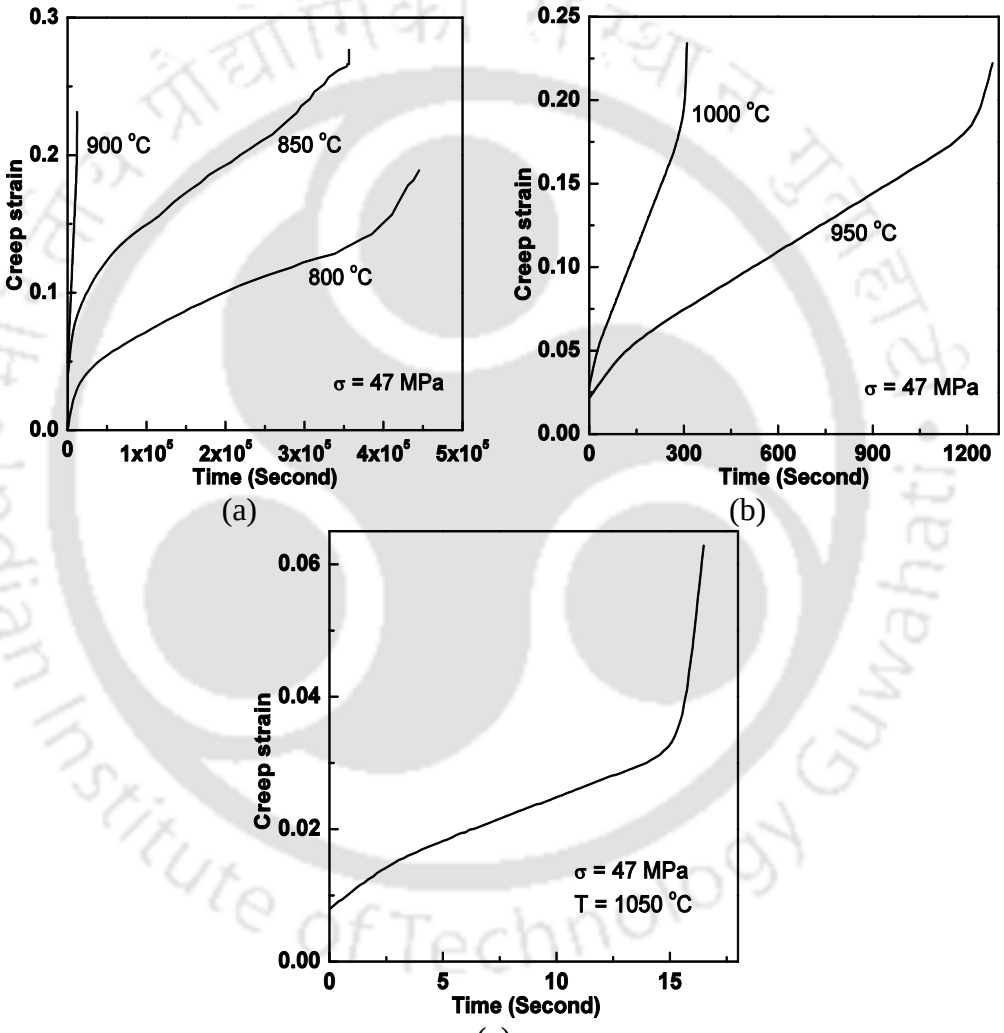

Fig. VII.1. Creep curves for HP40Nb micro-alloyed steel tested at 47 MPa, (a) 800 °C, 850 °C, 900 °C, (b) 950 °C, 1000 °C and (c) 1050 °C.

TH-1394_09610307

(ii) Constant stress of 68 MPa:

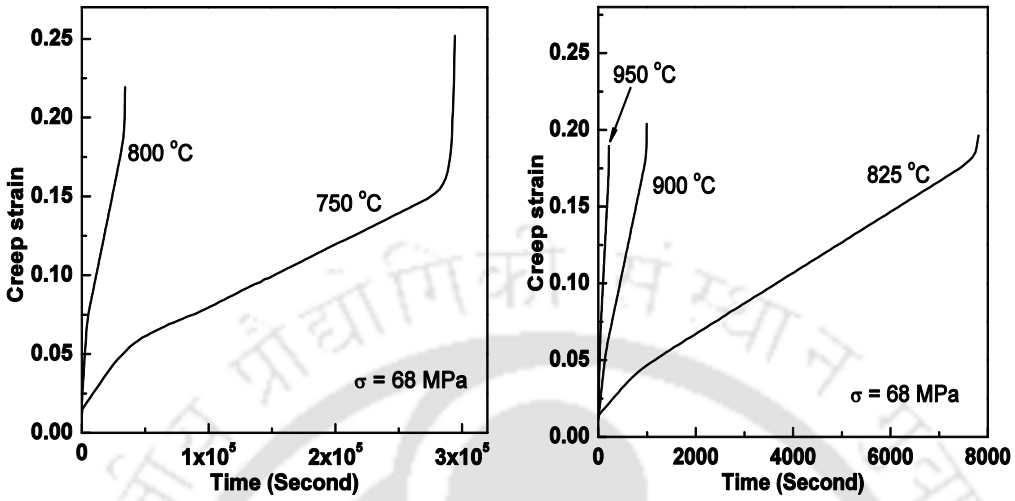

(a) (b)

Fig. VII.2. Creep curves for HP40Nb micro-alloyed steel tested at 68 MPa, (a) 750 °C, 800 °C and (b) 825 °C, 900 °C, 950 °C.

(iii) Constant stress of 80 MPa:

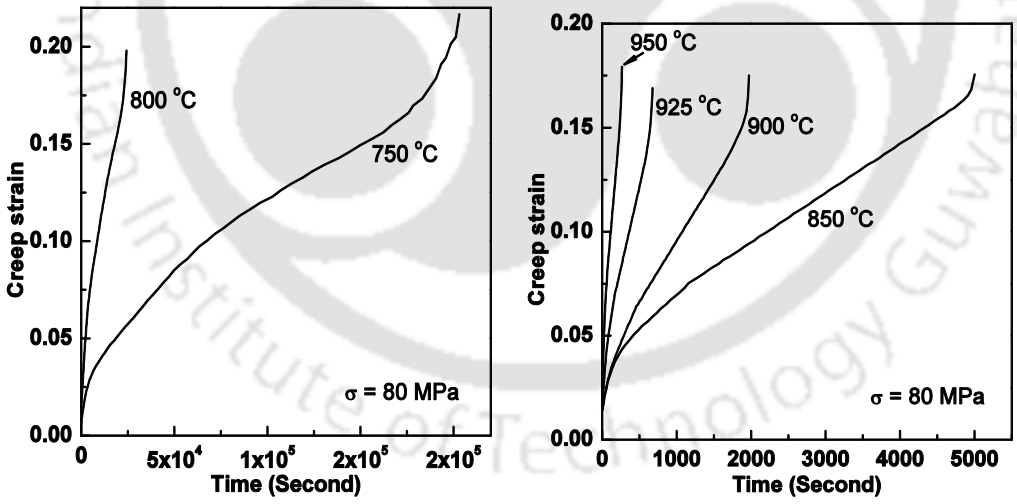

(a) (b)

Fig. VII.3. Creep curves for HP40Nb micro-alloyed steel tested at 80 MPa, (a) 750 °C, 800 °C and (b) 850 °C, 900 °C, 925 °C, 950 °C, .

TH-1394_09610307

(iv) Constant stress of 120 MPa:

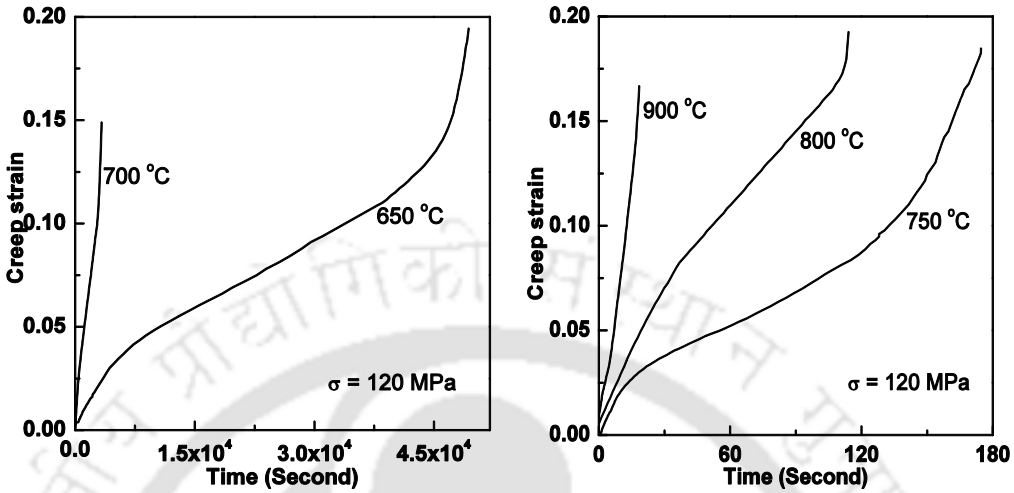

(a) (b)

Fig. VII.4. Creep curves for HP40Nb micro-alloyed steel tested at 120 MPa, (a) 650 °C, 700 °C and (b) 750 °C, 800 °C, 900 °C .

TH-1394_09610307

Appendix-VIII

Comparison of ANN simulated and experimental creep curves

The appendix contains comparison of ANN simulated and experimental creep curves for the remaining 16 experimental conditions.

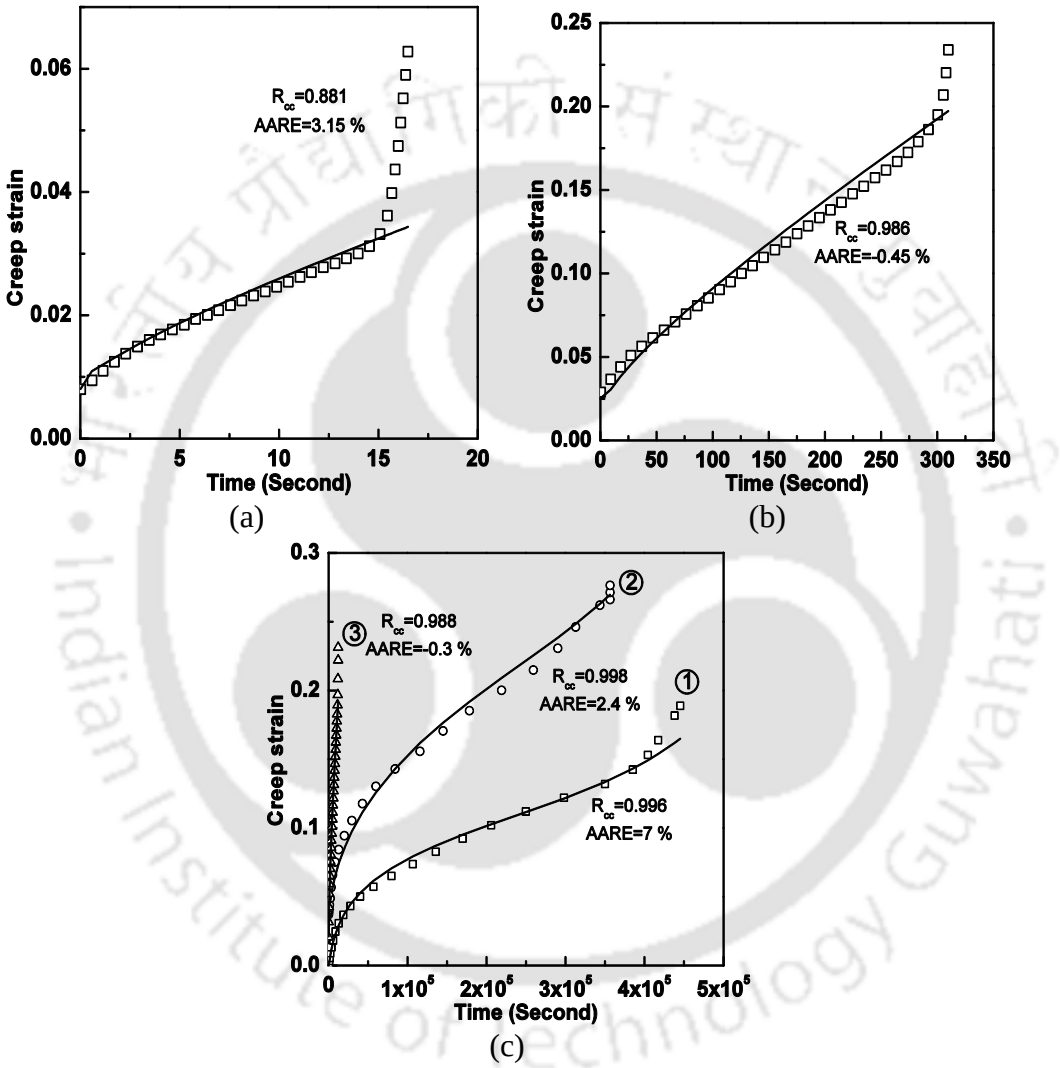

Figure VIII.1. Comparison between experimental and predicted creep curves at 47 MPa. Creep curves at (a) 1050 °C, (b) 1000 °C and (c) (1) 800 °C, (2) 850 °C, (3) 900 °C.

TH-1394_09610307

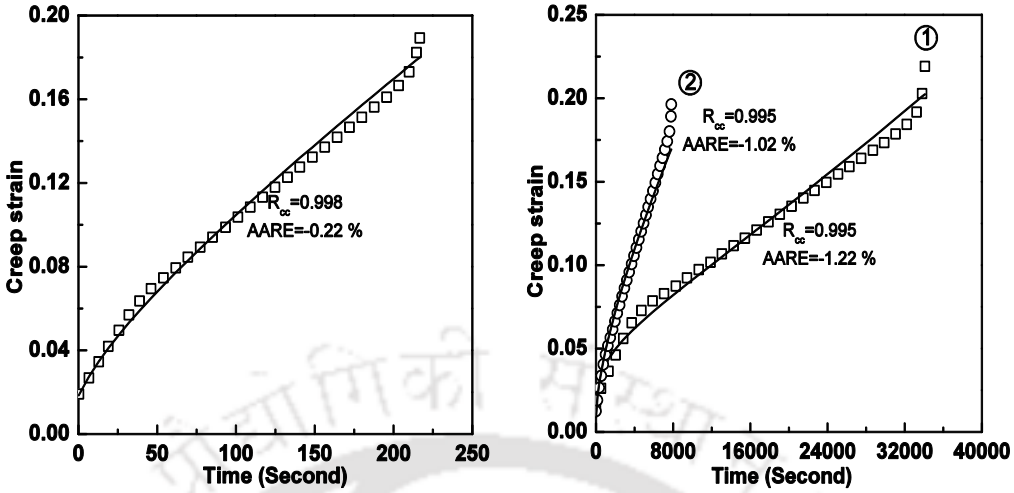

(a) (b)

Figure VIII.2. Comparison between experimental and predicted creep curves at 68 MPa. Creep curves at (a) 950 °C and (b) (1) 800 °C, (2) 825 °C.

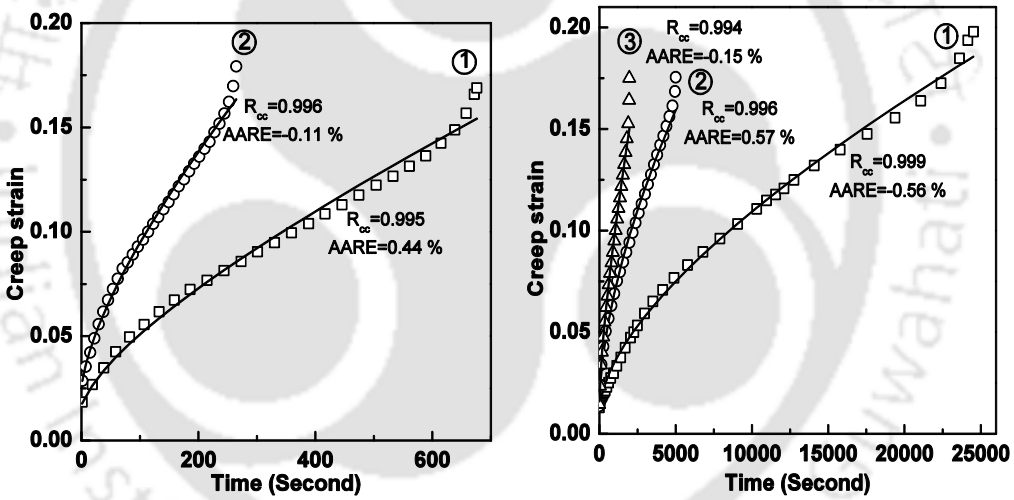

(a) (b)

Figure VIII.3. Comparison between experimental and predicted creep curves at 80 MPa. Creep curves at (a) (1) 925 °C, (2) 950 °C and (b) (1) 800 °C, (2) 850 °C, (3) 900 °C.

TH-1394_09610307

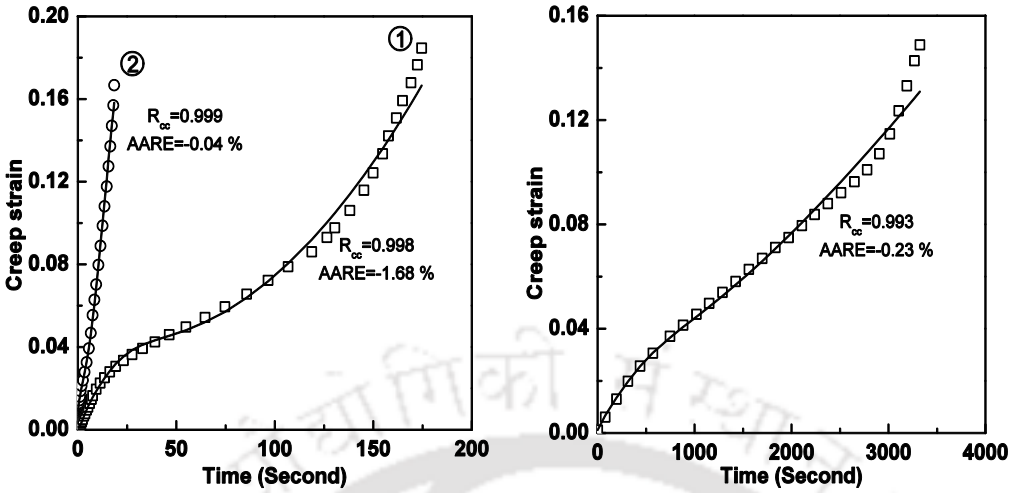

(a) (b)

Figure VIII.4. Comparison between experimental and predicted creep curves at 120 MPa. Creep curves at (a) (1) 750 °C, (2) 900 °C and (b) 700 °C.

TH-1394_09610307

LIST OF PUBLICATIONS

1. **A. Ghatak**, B. Das and P.S. Robi, Application of flexural resonance method for the determination of damping properties and Young's modulus of metallic materials at elevated temperatures, Twenty First International Conference on Processing and Fabrication of Advanced Materials (PFAM XXI), IIT Guwahati, Assam, December 2012, pp. 755-763.
2. **A. Ghatak** and P.S. Robi, Effect of Temperature on the Tensile Properties of HP40Nb Microalloyed Reformer Steel**,** Twenty Second International Conference on Processing and Fabrication of Advanced Materials (PFAM XXII), Institution of Engineers Singapore (IES), Singapore, December 2013, pp. 534-543.
3. **A. Ghatak** and P.S. Robi, Investigation of micro-structure and creep life analysis of centrifugally cast Fe-Cr-Ni alloy reformer tubes, Advances in Materials & Processing Technology Conference (AMPT 2014), Dubai, United Arab Emirates, November 2014.
4. **A. Ghatak** and P.S. Robi, Investigation of creep deformation of 25Cr35NiNb micro-alloyed reformer steel tube material, Twenty Third International Conference on Processing and Fabrication of Advanced Materials (PFAM 2014), IIT Roorkee, India, December 2014.
5. **A. Ghatak** and P.S. Robi, Effect of microstructure with hardness on heat treatment of HP40Nb micro-alloyed reformer tube, 5th International and 26th All India Manufacturing Technology, Design and Research Conference (AIMTDR 2014), IIT Guwahati, India, December 2014.
6. **A. Ghatak** and P.S. Robi, Effect of temperature on the microstructure and hardness of service exposed 25Cr35NiNb reformer tubes, Transaction of Indian Institute of Metals (Under review).
7. **A. Ghatak** and P.S. Robi, High temperature tensile properties and fracture of 25Cr35NiNb micro-alloyed steel, Journal of Alloys and Compounds (To be communicated).
8. **A. Ghatak** and P.S. Robi, Analysis of creep behavior and damage tolerance factor of 25Cr35NiNb micro-alloyed steel, Journal of Materials Science (To be communicated).
9. **A. Ghatak** and P.S. Robi, Artificial neural network modeling of creep curve of HP40Nb microalloyed steel (Under preparation).
10. **A. Ghatak** and P.S. Robi, Constitutive equations in creep of HP40Nb microalloyed steel (Under preparation).

TH-1394_09610307